学位論文

Simultaneous multi-wavelength observation of giant radio pulses from the Crab pulsar

(多波長同時観測による カニパルサー巨大電波パルスの研究)

平成 27 年 12 月博士（理学）申請

東京大学大学院理学系研究科
物理学専攻
三上　諒

Abstract

From pulsars, extremely stable pulsed emission is observed, which suggests that pulsars are rapidly rotating and magnetized neutron stars. Among more than 2500 pulsars ever discovered, the Crab pulsar is one of the most famous pulsars, which is located at the center of the Crab nebula. The Crab has been extensively studied theoretically and observationally.

Only $\sim$ 10 of 2500 pulsars, including the Crab pulsar, sporadically emit extremely strong radio pulses called Giant Radio Pulses (GRPs). The emission mechanism of GRPs has not been revealed yet. In most pulsars, normal pulses are so weak that their pulse profiles are obtained only by accumulating synchronously the data at the pulse period. This averaging (folding) procedure leads to loss of information on the behavior of individual pulses. On the other hand, GRPs can be readily detected without being hidden by background noise due to their strong signals. Therefore GRPs give us more direct information about their emission mechanism.

GRPs show a pulse-to-pulse variation of pulse structures or flux at different frequencies. It is important to observe GRPs at multiple frequency bands simultaneously. In order to study how GRPs relate at different frequencies and how GRPs affect the emissions at other wavelengths, we study the emission mechanism of GRPs from the Crab pulsar in terms of the "simultaneous multi-wavelength observation" in this thesis.

First, we present the results of the simultaneous observation of the GRPs from the Crab pulsar at 0.3, 1.6, 2.2, 6.7 and 8.4 GHz with four telescopes in Japan (Kashima, Usuda, Iitate and Takahagi observatories). The frequency coverage ($\sim$ 1.5 decades) is the most broadband among ever reported. We obtain 3194 and 272 GRPs occurring at the main pulse (MPGRPs) and the interpulse phases (IPGRPs). The number of samples are large compared to most of the past multi-frequency observations. Some past studies collect more GRP samples than our study, but their samples are not obtained simultaneously. For our GRP samples, we carry out the spectral fitting with a single power-law function to each GRP spectrum. For the frequency range from 0.3 to 2.2 GHz, about 70% of the GRP spectra are consistent with single power-laws and the spectral

indices of them are roughly distributed from -4 to -1. We find apparent correlations between the fluences and the spectral hardness, which may indicate that less energetic pulses tend to show harder spectra ("dim-hard" GRPs). We also find a significant number of GRPs which are too weak to identify at 0.3 GHz but can be identified at both 1.6 GHz and 2.2 GHz. Those GRPs imply harder spectra than stronger ones and also normal pulses. Stacking such weak GRPs, we confirm the existence of such "dim-hard" GRPs at 0.3 GHz. Those results may strengthen the fluence-hardness correlations, or they indicate that most of GRPs may have intrinsically harder spectra than that ever reported.

The second work in this thesis is a search for a correlation between GRPs and hard X-ray pulses from the Crab pulsar. Since the spectral signature at higher energy bands is quite different from a radio band, the emission mechanism at radio band is thought to be different from that at higher energy bands. For this reason, those high energy pulses were not thought to show violent flux variation similar to the variation in radio bands, i.e., GRPs. Nevertheless, recent observation showed that optical pulses coincident with the GRPs from the Crab pulsar were on average a few percent brighter than those at non-GRP periods. This suggests that there is some kind of link between GRPs and high energy emissions. Testing the correlation between the GRPs and the pulses at other frequency bands is important for understanding the generation mechanism of GRPs in the pulsar magnetosphere.

We report the results of the simultaneous radio and hard X-ray observations of the Crab pulsar in 2010, 2013 and 2014. The correlation between GRPs and pulsed emission at the hard X-ray band has not been explored before. The observations were made with the Kashima and Usuda antennae at radio band and the Suzaku HXD at hard X-ray band. From the entire observing sessions, we obtain 7414 MPGRPs and 556 IPGRPs during the X-ray exposure times of more than 12 hours. We search for flux enhancement at hard X-ray band coincident with GRPs compared to that of non-GRP periods. For the PIN (15-75 keV) data, we set the upper limit of peak flux enhancement coincident with the MPGRPs and the IPGRPs to 33% and 88%, respectively, at a confidence level of 95%. For the GSO (40 - 600 keV) data, we also set the upper limit of peak flux enhancement to 63% and 193% coincident with the MPGRPs and the IPGRPs, respectively, at a confidence level of 95%. In contrast to radio band, hard X-ray emission does not show violent flux variation, which is consistent with the past optical study. The future X-ray telescopes, such as ASTRO-H, will improve our results.

Contents

Chapter 1

Introduction

A "Pulsar", from which we can receive extremely stable pulsed emission, was firstly discovered in 1967 (Hewish et al., 1968). Pulsars have been identified with rapidly rotating, magnetized neutron stars since the proposals by (Pacini, 1967; Gold, 1968).

Since the discovery of pulsars, it is still not possible to give a clear explanation of "what makes them shine", which Taylor & Stinebring (1986) mentioned. In pulsars, huge electric potential is induced due to their strong magnetic fields and rapid rotations by the process of unipolar induction (Goldreich & Julian, 1969). The electric force due to the induced electromagnetic field around the pulsar is much stronger than the gravitational force (by a factor of $\sim 10^8$ for a proton). Therefore, charged particles are pulled away from the surface of the star, and form a co-rotating magnetosphere surrounding the star. In order to explain the observed pulsed emission, a part of the induced electric potential should be exhausted for the acceleration of plasmas and plasma multiplication in the magnetosphere. Many models assume an existence of the namely "gap" region in the magnetosphere, where the condition of a co-rotating magnetosphere is not satisfied, a force-free state cannot be maintained and the electric field parallel to a magnetic field line exist. Such gap region is modeled as, for example, the "polar cap" (e.g. Sturrock, 1971; Ruderman & Sutherland, 1975), or the "outer gap" (e.g. Cheng et al., 1986a,b). Recent observations have restricted the emission region at γ-ray bands (e.g. Abdo et al., 2009), but there is no widely accepted and self-consistent model so far.

Radio emission from pulsars has a more difficult problem. We can estimate the brightness temperatures of the observed pulses $T_b = (\lambda^2/2k_B)(S_\nu/\Omega)$ from the distance of the pulsar, the duration of the pulse and observed flux density of the pulse S_ν (where k_B is the Boltzmann constant and λ is the observing wavelength). They are typically $10^{23} - 10^{26}$K, considerably exceeding the temperatures of matters in the pulsar

magnetosphere. Therefore, pulsar radio emission cannot be explained by a simple sum of emission from accelerated particles in the pulsar magnetosphere, and may be attributed to some coherent process such as a bunching mechanism (e.g. Cheng & Ruderman, 1977) or a maser process (e.g. Luo & Melrose, 1992). Many theoretical models have been proposed, but the question how the radio emission is produced has not been solved yet. One of the reasons of it is that, as Melrose (1995) pointed out, no widely accepted, self-consistent model of the pulsar magnetosphere is constructed. In this situation, it is difficult to predict the distributions of plasmas required to determine the relevant process of coherent emission.

We focus on a peculiar form of pulsar radio emission, giant radio pulses (GRPs). GRPs are characterized by a large intensity variation reaching more than ten times, or occasionally thousands of times larger than that of average pulses. The energy distributions of GRPs follow power-law ones, while the intensity distributions of "normal" pulses in many pulsars follow log-normal ones (Burke-Spolaor et al., 2012). While more than 2500 pulsars have been discovered at present[1] (Manchester et al., 2005), GRPs have been detected in only ~ 10 pulsars so far (e.g. Cognard et al., 1996; Johnston & Romani, 2003; Singal & Vats, 2012). Some theoretical models of GRPs have been proposed so far (Petrova, 2004; Gil & Melikidze, 2005; Lyutikov, 2007), but their emission mechanism have not been revealed yet.

Most of normal pulses are weak and their pulse profiles can be obtained by adding synchronously of the data at the pulse period. By this "folding" procedure, some characteristics of individual pulses are lost. On the other hand, GRPs can be readily detected without being hidden by a background noise due to their strength. Therefore from GRPs, we can get more direct information about the particles relevant to their emission and their emission mechanism.

In this thesis, we focus on the GRPs from the Crab pulsar (Figure 1). The Crab pulsar was discovered by GRPs (Stalin & Reifenstein, 1968). The GRPs from the Crab pulsar can be relatively frequently observed compared to the other GRP-emitting pulsars (e.g. Knight et al., 2006a). Besides, we obtain more information from the emission at higher energy bands because of relatively bright emission from the Crab pulsar compared to other pulsars (e.g. Thompson et al., 1999). Therefore, the Crab pulsar is the best candidate studying GRPs.

We study the GRPs from the Crab pulsar from the viewpoint of the "multi-wavelength observations" in this thesis. First, we carry out the spectral study of the Crab GRPs

[1] http://www.atnf.csiro.au/people/pulsar/psrcat/

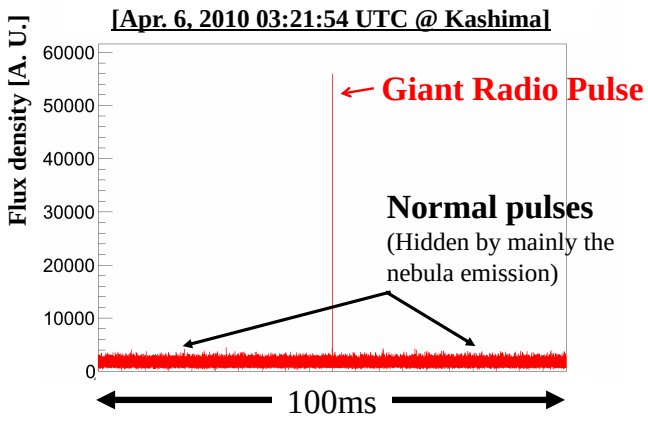

Fig. 1.1.— Example of a GRP from the Crab pulsar. This GRP was detected with the Kashima 34m antenna on Apr. 6, 2010. The 100-ms time series data (light curve) is drawn. The "normal" pulses around the GRP are hidden by the noise, which is mainly due to the emission from the Crab nebula.

based on the simultaneous multi-frequency observation at the radio frequency band. There are a lot of multi-frequency observations of the Crab GRPs (e.g. Kostyuk et al., 2003; Hankins et al., 2015), and in some studies, spectral indices or shapes have been investigated (Sallmen et al., 1999; Popov et al., 2009; Oronsaye et al., 2015). However, the numbers of samples were insufficient to discuss the statistical properties of the GRP spectra in some studies. Also, the relation between spectral indices and other quantities such as fluences has not yet been reported. Using the telescopes in Japan, we made the wide-band simultaneous observation of the Crab GRPs at 0.3, 1.6, 2.2, 6.7 and 8.4 GHz, and extracted the spectral features of the GRPs.

The second work in this thesis is a search for a correlation between GRPs and hard X-ray pulses from the Crab pulsar. As mentioned above, radio emission from pulsars requires some coherent process, while emission at higher energy bands, for example optical or X-ray emission, is modeled by the incoherent synchrotron radiation (e.g. Takata & Chang, 2007). Radio and high-energy pulses seem to be irrelevant, but Shearer et al. (2003) reported that optical pulses concurrent with the GRPs from the Crab pulsar are on average $\sim$ 3% brighter than those coincident with normal radio pulses. Similar enhancement was also obtained by Collins et al. (2012) and Strader et al. (2013). This suggests that there is some kind of link between the coherent and incoherent emissions generated in the Crab pulsar. Testing the correlation between the GRPs and the pulses at other frequency bands is important for obtaining a clue to understand the generation mechanism of GRPs in the pulsar magnetosphere. We

focus on the hard X-ray band, where no other correlation study was carried out in the previous studies (e.g. Bilous et al., 2011; Aliu et al., 2012). We did not find a significant enhancement of hard X-ray emission coincident with GRPs, but set the upper limit on its enhancement.

This thesis is organized as follows. In Chapter 2, we review the basic concepts of a pulsar and a pulsar magnetosphere at first. In this chapter, we also review GRPs in the observational and the theoretical viewpoints. In Chapter 3, we describe basic principles of our data analysis including the dedispersion procedure, the transformation of the data time and the flux calibration. In Chapter 4, we describe our results of the wide-band observation of the GRPs from the Crab Pulsar. In Chapter 5, we show the results of a search for a correlation between GRPs and hard X-ray pulses from the Crab pulsar. In Chapter 6, we summarize the results and discuss them.

Chapter 2

Pulsars and Giant Radio Pulses from Pulsars

2.1 Spin-down, and magnetic dipole radiation

Change in the observed pulse periods can be related to the loss of the rotational energy of the pulsar. The rate of increase in pulse periods of a pulsar $\dot{\mathrm{P}}$ and the rate of loss of its rotational energy $\dot{\mathrm{E}}$ are related in the following relation;

$$\dot{\mathrm{E}} \equiv \frac{\mathrm{d}E_{rot}}{\mathrm{d}t} = \frac{\mathrm{d}(\frac{1}{2}I\Omega^2)}{\mathrm{d}t} = -I\Omega\dot{\Omega} = 4\pi^2 I\dot{P}P^{-3}, \tag{2.1}$$

where $\Omega \equiv \frac{2\pi}{P}$ is the rotational angular frequency of the pulsar, and I represents the moment of inertia of the pulsar. $\dot{\mathrm{E}}$ is also referred to as "spin-down luminosity". Using $I = 10^{45}\mathrm{g}\cdot\mathrm{cm}^2$, [1]

$$\dot{\mathrm{E}} \simeq 4\times10^{31}\mathrm{erg}\cdot\mathrm{s}^{-1}\left(\frac{\dot{P}}{10^{-15}}\right)\left(\frac{P}{1\mathrm{s}}\right)^{-3}. \tag{2.4}$$

There is a strong dipole magnetic field around a neutron star. When a magnetic dipole with a magnetic moment $\mathbf{m}$ rotates, it emits an electromagnetic wave at its rotational frequency. This radiation is called "magnetic dipole radiation". The emitted power of magnetic dipole radiation is represented as

$$\dot{\mathrm{E}}_{\mathrm{dipole}} = \frac{2}{3c^3}|\mathbf{m}|^2\Omega^4\sin^2\alpha, \tag{2.5}$$

[1] A moment of inertia of a sphere of uniform density is described as

$$I = \frac{2}{5}MR^2, \tag{2.2}$$

where M and R is mass and a radius of the sphere, respectively. If we substitute $M = 1.4M_\odot$ and $R = 10\mathrm{km}$,

$$I \sim 10^{45}\mathrm{g}\cdot\mathrm{cm}^2. \tag{2.3}$$

where α is the angle between the rotational axis and the magnetic moment. When we equate the power in Equation (2.5) with spin-down luminosity described in Equation (2.1), we get

$$\dot{\Omega} = -\left(\frac{2|\mathbf{m}|^2 \sin^2 \alpha}{3Ic^3}\right)\Omega^3. \tag{2.6}$$

Using the relation $\Omega = 2\pi\nu$, we obtain

$$\dot{\nu} = -K\nu^n. \tag{2.7}$$

where n is referred to as a "braking index". If the spin-down of the pulsar is only due to magnetic dipole radiation, $n = 3$.

When we differentiate Equation (2.7) by time, we obtain

$$\ddot{\nu} = -nK\nu^{n-1}\dot{\nu}. \tag{2.8}$$

From Equations (2.7) and (2.8),

$$n = \frac{\nu\ddot{\nu}}{\dot{\nu}}. \tag{2.9}$$

Therefore, we can estimate the braking index of a pulsar with pulse period P, its rate of increase $\dot{\mathrm{P}}$ and its rate of change $\ddot{\mathrm{P}}$. The obtained braking index deviates from $n = 3$ (Livingstone et al., 2007). This suggests that there are some process(es) of energy dissipation other than magnetic dipole radiation, but the condition $n = 3$ is often assumed in order to see the basic characteristics of pulsars. We discuss them below.

From Equation (2.7),

$$\dot{P} = KP^{2-n} \tag{2.10}$$

By assuming that K is constant and integrating Equation (2.10) from $t = 0$ (the birth time of the pulsar) to $t = T$ (now), we obtain

$$\int_{t=0}^{t=T} P^{n-2}\mathrm{d}P = \int_0^T K\mathrm{d}t$$
$$KT = \frac{1}{n-1}(P^{n-1} - P_0^{n-1}), \tag{2.11}$$

where P_0 is the rotational period of the pulsar at birth.

$$T = \frac{1}{K(n-1)} \cdot P^{n-1}\left[1 - \left(\frac{P_0}{P}\right)^{n-1}\right] \tag{2.12}$$

Using the relation shown in Equation (2.10), we get

$$T = \frac{P}{\dot{P}(n-1)}\left[1 - \left(\frac{P_0}{P}\right)^{n-1}\right]. \tag{2.13}$$

Assuming that the present rotational period of the pulsar is much slower than that at birth ($P \gg P_0$) and that the spin-down of the pulsar is only due to magnetic dipole radiation ($n = 3$), we obtain

$$\mathrm{T_{age}} = \frac{P}{2\dot{P}} = 1.58 \times 10^7 \mathrm{year} \left(\frac{P}{1\mathrm{s}}\right) \left(\frac{\dot{P}}{10^{-15}\mathrm{s/s}}\right). \tag{2.14}$$

$\mathrm{T_{age}}$ is often used as the "characteristic age" of a pulsar.

When we assume the spin-down of the pulsar is only due to magnetic dipole radiation ($n = 3$). The magnetic moment $|\mathbf{m}|$ is related to strength of the magnetic field in the following relation;

$$B \approx \frac{|\mathbf{m}|}{r^3}. \tag{2.15}$$

From Equation (2.6),

$$\frac{P\dot{P}}{4\pi^2} = \frac{2|\mathbf{m}|^2 \sin^2 \alpha}{3Ic^3}. \tag{2.16}$$

By substituting $r = R$ (radius of the star) to Equation (2.16), strength of the magnetic field at the surface of the neutron star B_S can be described as

$$B_S \equiv B(r = R) = \sqrt{\frac{3c^3}{8\pi^2} \frac{I}{R^6 \sin^2 \alpha} P\dot{P}}. \tag{2.17}$$

Assuming $I = 10^{45}\mathrm{g \cdot cm^2}$, $R = 10\mathrm{km}$, $\alpha = 90^\circ$, we obtain

$$B_S = 3.2 \times 10^{19}\mathrm{Gauss}\sqrt{P\dot{P}} \simeq 10^{12}\mathrm{Gauss} \left(\frac{P}{1\mathrm{s}}\right)^{1/2} \left(\frac{\dot{P}}{10^{-15}\mathrm{s/s}}\right)^{1/2}. \tag{2.18}$$

It should be noted that this expression is a rough estimate because α is usually unknown, mass and a radius of a neutron star is currently uncertain, and the spin-down process can be due to processes other than magnetic dipole radiation. However, this expression is often used as an indicator of strength of the magnetic field at the surface of the star.

2.2 Pulsar Magnetosphere

In this subsection, we discuss the electromagnetic field formed around the pulsar. Goldreich & Julian (1969) discussed the electromagnetic fields around the pulsar in the case of the aligned rotator, where the magnetic axis and the rotational axis are aligned with each other. This model depicts basic principles of a pulsar magnetosphere. Below, we summarize their discussion.

Here, we consider the neutron star as a conducting sphere rotating with the angular frequency Ω. We also assume that the sphere is uniformly magnetized in z-direction,

and the magnetic field is therefore described as $\mathbf{B}_{\rm in} = B_0\mathbf{e}_z$. Due to the rotation of the magnetized sphere, the electric field is induced at any point $\mathbf{r}$ in the sphere. Charged particles in the interior feel the electric force from the induced field. As the star rotates, particles also feel the Lorentz force, and two types of forces are finally balanced. As a result, at any point $\mathbf{r}$ in the inside of the star, the relation

$$\mathbf{E}_{\rm in} + \frac{1}{c}(\mathbf{\Omega} \times \mathbf{r}) \times \mathbf{B}_{\rm in} = 0 \tag{2.19}$$

is satisfied. Therefore, $\mathbf{E}_{\rm in} \cdot \mathbf{B}_{\rm in} = 0$ is satisfied inside the star. Using the spherical coordinates (r, θ, ϕ), $\mathbf{E}_{\rm in}$ is described as

$$\mathbf{E}_{\rm in} = -\frac{\Omega B_0 r}{c}(\sin^2\theta \mathbf{e}_r + \sin\theta\cos\theta \mathbf{e}_\theta). \tag{2.20}$$

Since $\partial \mathbf{B}_{\rm in}/\partial t = 0$, the equation $\nabla \times \mathbf{E}_{\rm in} = 0$ is realized inside the star. Using the electric potential $\Phi_{\rm in}$, we can represent $\mathbf{E}_{\rm in}$ as $\mathbf{E}_{\rm in} = -\nabla\Phi_{\rm in}$. Therefore, we get

$$\Phi_{\rm in} = \left(\frac{\Omega B_0}{2c}\right)(r\sin\theta)^2 + \text{const.} \tag{2.21}$$

$$= -\left(\frac{\Omega B_0 r^2}{3c}\right)[P_2(\cos\theta) - 1] + \text{const.} \tag{2.22}$$

where $P_2(\cos\theta)$ is the Legendre polynomial of order 2.

Next, we consider the electromagnetic field outside the star. Since we now assume that there is a vacuum outside the star, the electric potential $\Phi_{\rm out}$ satisfies the following relation;

$$\triangle\Phi_{\rm out}(r, \theta) = 0. \tag{2.23}$$

This is namely the Laplace equation, and we take its general solution in the form

$$\Phi_{\rm out}(r, \theta) = \sum_{l=1}^{\infty} \frac{a_l}{r^{l+1}} P_l(\cos\theta). \tag{2.24}$$

The electric potentials on the inside and outside of the star should match each other at the surface of the star, $r = R_{NS}$. Therefore, we get

$$\Phi_{\rm out}(r, \theta) = \frac{B_S \Omega R_{NS}^5}{6cr^3}(3\cos^2\theta - 1). \tag{2.25}$$

The electric field outside the star is expressed as

$$\mathbf{E}_{\rm out} = -\nabla\Phi_{\rm out}(r, \theta) = -\frac{\partial\Phi_{\rm out}}{\partial r}\mathbf{e}_r - \frac{1}{r}\frac{\partial\Phi_{\rm out}}{\partial\theta}\mathbf{e}_\theta \tag{2.26}$$

$$= -\frac{B_0\Omega R_{NS}^5}{2cr^4}(3\cos^2\theta - 1)\mathbf{e}_r - \frac{B_0\Omega R_{NS}^5}{cr^4}\cos\theta\sin\theta\mathbf{e}_\theta \tag{2.27}$$

The magnetic field outside the star is a dipole field with moment $m = B_0 R_{NS}^3$, that is

$$\mathbf{B}_{\rm out} = \frac{B_0 R_{NS}^3 \cos\theta}{r^3}\mathbf{e}_r + \frac{B_0 R_{NS}^3 \sin\theta}{2r^3}\mathbf{e}_\theta. \tag{2.28}$$

Therefore, we get the following relation;

$$\frac{B_\theta}{B_r} = \frac{r d\theta}{dr} = \frac{\sin\theta}{2\cos\theta}. \tag{2.29}$$

Solving the differential equation above, we get

$$\frac{\sin^2\theta}{r} = \text{const.} \tag{2.30}$$

for a dipole field. We also obtain the charge density at the surface of the star, $\sigma_{\rm sur}$, from the discontinuity of the radial component of the electric field;

$$\sigma_{\rm sur} = \frac{1}{4\pi}(E_{\rm in,r} - E_{\rm out,r}) = \frac{\Omega B_0 R_{NS}}{12\pi}[2 - 5P_2(\cos\theta)] \tag{2.31}$$

From Equations (2.27) and (2.28), we get

$$\mathbf{E}_{\rm out}\cdot\mathbf{B}_{\rm out} = -\frac{\Omega R_{NS} B_0^2}{c}\left(\frac{R_{NS}}{r}\right)^7 \cos^3\theta. \tag{2.32}$$

Therefore, at the surface of the star, the electric field along the magnetic field line is

$$E_\parallel = \left[\frac{\mathbf{E}\cdot\mathbf{B}}{B}\right]_{r=R} = -\frac{B_S \Omega R_{NS}}{c}\cos^3\theta. \tag{2.33}$$

From Equation (2.33), we evaluate the electric force working on a charged particle. For a single proton,

$$\frac{\text{(electric force)}}{\text{(gravitational force)}} = \frac{e\Omega B_S R_{NS}/c}{G m_p M/R_{NS}^2} \sim 10^8 \left(\frac{B_S}{10^{12}\text{G}}\right)\left(\frac{M}{1.4M_\odot}\right)\left(\frac{P}{1\text{s}}\right)^{-1}. \tag{2.34}$$

Therefore, the environment around the star can not be a vacuum. Charged particles can be pulled out of the surface and they will create a "magnetosphere" around the star.

The charged particles pulled from the surface of the star move along the magnetic field lines. The momentum perpendicular to the magnetic field line is rapidly lost by radiation. The particles rearrange their own motion so that no net electromagnetic force acts on them. Therefore, for the particles in the magnetosphere, the following relation is satisfied;

$$\mathbf{E} + \frac{\mathbf{v}}{c}\times\mathbf{B} = 0, \tag{2.35}$$

where the velocity $\mathbf{v}$ satisfies $\mathbf{v} = \mathbf{\Omega} \times \mathbf{r}$. From the resulting electric field $\mathbf{E}$, the Maxwell's equations $\nabla \cdot \mathbf{E} = 4\pi\rho$ and $\nabla \times \mathbf{B} = \frac{4\pi}{c}\rho\mathbf{v}$, the charge density in the co-rotating magnetosphere is

$$\rho_{GJ} = \frac{1}{4\pi}\nabla \cdot \mathbf{E} = -\frac{\mathbf{B} \cdot \mathbf{\Omega}}{2\pi c}\frac{1}{1-(r\Omega/c)^2\sin^2\theta}. \tag{2.36}$$

This charge density is referred to as the "Goldreich-Julian density". The number density of the charges is approximately

$$n_{\rm GJ} \sim \frac{B_S\Omega}{2\pi ce} = \frac{B_S}{ceP} \sim 7\times10^{10}{\rm cm}^{-3}\left(\frac{P}{1{\rm s}}\right)^{-1/2}\left(\frac{B_S}{10^{12}{\rm G}}\right)^{1/2}. \tag{2.37}$$

The charged particles co-rotate with the star. If the charge density deviates from ρ_{GJ}, Equation (2.35) is not satisfied and $\mathbf{E} \cdot \mathbf{B} \neq 0$. Therefore, the electric fields along magnetic field lines will develop and the particles will be accelerated by them. This will be discussed later.

Since plasmas cannot move at a speed faster than the speed of light, co-rotation of plasmas can be maintained only within the cylindrical region called the "light cylinder". The radius of the light cylinder $R_{\rm LC}$ is

$$R_{\rm LC} = \frac{c}{\Omega} = \frac{cP}{2\pi} \simeq 4.8\times10^4{\rm km}\left(\frac{P}{1s}\right) \tag{2.38}$$

From Equation (2.15) and (2.17), the magnetic field at the position of the light cylinder $B_{\rm LC}$ is

$$B_{\rm LC} = B_S\left(\frac{R}{R_{\rm LC}}\right)^3 \simeq 9.2{\rm Gauss}\left(\frac{P}{1{\rm s}}\right)^{-5/2}\left(\frac{\dot{P}}{10^{-15}{\rm s/s}}\right)^{1/2}, \tag{2.39}$$

where we assume $I = 10^{45}{\rm g}\cdot{\rm cm}^2$ and $R = 10{\rm km}$. The motion of particles depends on whether the magnetic field line along which they move closes before reaching the light cylinder. According to Equation (2.30), the field lines emanating at the angular region $\theta > \theta_{\rm PC}$ close before reaching the light cylinder ("closed field lines"), and the field lines emanating at the angular region $\theta < \theta_{\rm PC}$ cross the light cylinder ("open field lines"). The angular region $\theta < \theta_{\rm PC}$ is referred to as the polar cap region. The critical field line is tangential to the light cylinder. This line satisfies the following relation;

$$\frac{\sin^2 90^\circ}{R_{\rm LC}} = \frac{2\pi}{cP} = \frac{\sin^2\theta_{\rm PC}}{R} \tag{2.40}$$

Assuming $\theta_{\rm PC} \ll 1$, the polar cap radius $R_{\rm PC}$ is

$$R_{\rm PC} \simeq R\sin\theta_{\rm PC} = \sqrt{\frac{2\pi R^3}{cP}} = 1.5\times10^4{\rm cm}\left(\frac{P}{1{\rm s}}\right)^{-1/2}\left(\frac{R}{10{\rm km}}\right)^{3/2}. \tag{2.41}$$

The potential difference $\Delta\Phi$ between the magnetic pole and the edge of the polar cap region is estimated as follows;

$$\begin{aligned}\Delta\Phi &= \Phi(R,0) - \Phi(R,\theta_{\rm p}) \\ &= \frac{B_S\Omega R^5}{3cR^3} - \frac{B_S\Omega R^5}{6cR^3}(3\cos^2\theta_{\rm p} - 1) \\ &= \frac{2\pi^2 B_S R^3}{c^2 P^2} \\ &= 2\times10^{13}{\rm Volt}\left(\frac{P}{1{\rm s}}\right)^{-3/2}\left(\frac{\dot{P}}{10^{-15}{\rm s/s}}\right)^{1/2}, \end{aligned} \tag{2.42}$$

where Equation (2.17) is used in the last equality.

The deviation of the charge density from the Goldreich-Julian charge density gives rise to the electric field along the magnetic field lines, and they will accelerate the particles. However, it is an open question where such electric field is formed. Some models of the electric field were proposed based on the formation of the charge depleted region ("gap" region) accompanied with the outflow of the particles from the magnetosphere. One of the models is the "polar cap" model (e.g. Sturrock, 1971; Ruderman & Sutherland, 1975), of which gap region is formed near the magnetic pole. Another model is the "outer gap" model (e.g. Cheng et al., 1986a,b), of which gap region is formed near the "null surface" satisfying $\rho_{GJ} = 0$ in the outer magnetosphere. From these models, different shapes of the energy spectrum at γ-ray band were predicted (e.g. Daugherty & Harding, 1996). Recent γ-ray observations with the *Fermi* satellite have suggested that the polar cap region is unlikely to be the acceleration site of the particles responsible for γ-ray emission (e.g. Abdo et al., 2009). In recent studies, Takata & Chang (2007) also reported that the emission from the Crab pulsar from optical to γ-ray bands can be modeled by the emission from the outer gap. However, a generally acceptable model at the whole energy bands has not been constructed yet.

2.3 Giant Radio Pulses

2.3.1 Observational aspects of Giant Radio Pulses

In this section, we discuss giant radio pulses from pulsars. Radio pulses from some pulsars show anomalous excess of pulse flux compared to average ones. Those extremely strong radio pulses are called "Giant Radio Pulses (GRPs)". In some previous studies, the "working" definition of a GRP is used, which is that the peak flux and the total energy of a pulse is more than ten times the mean ones (e.g. Johnston et al., 2001;

Tsai et al., 2015). However, as Hankins et al. (2015) pointed out, there is no standard criterion for defining GRPs at present.

GRPs commonly show the distribution of peak flux density or total energy of GRPs follows a power-law statistics (e.g. Argyle & Gower, 1972; Cognard et al., 1996, see also Figure 2.1), while those of "normal pulses" are well described as log-normal ones (Burke-Spolaor et al., 2012). For the Crab GRPs, it is also reported that the power-law indices are different according to the observing frequencies and the observation dates (Mickaliger et al., 2012, and references therein).

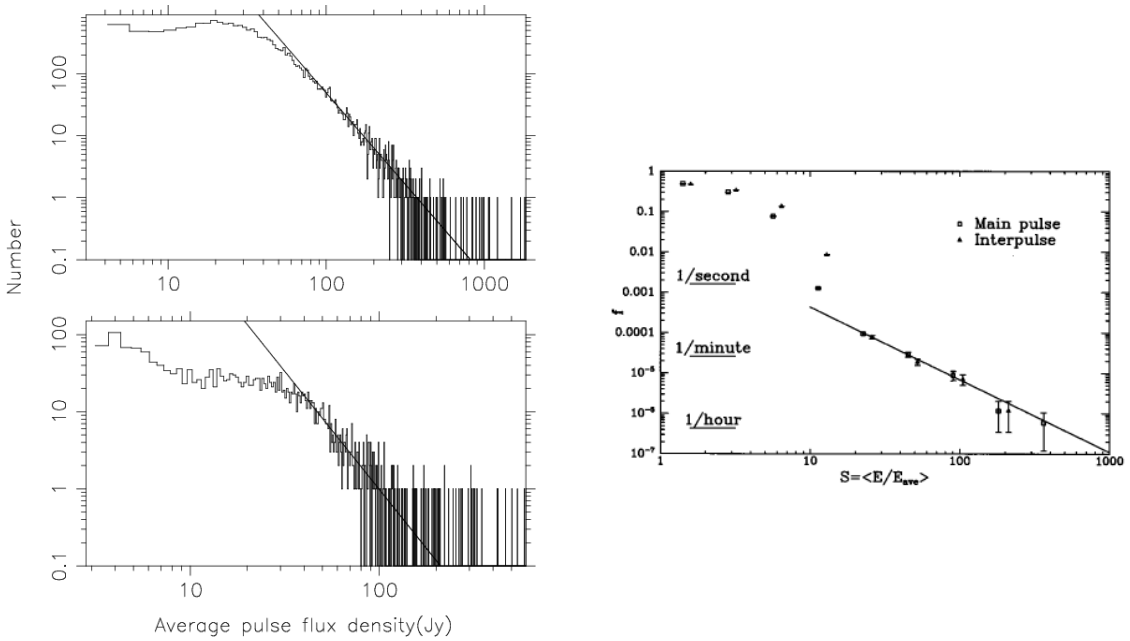

Fig. 2.1.— Left: Distribution of the pulse intensity of GRPs detected at the main- (top) and interpulse (bottom) phases, respectively. The best fit power-law curve is shown with slope -2.79 ± 0.01 for the pulses in main pulse phase and -3.06 ± 0.06 for the pulses in the interpulse phase. This figure is taken from Figure 4 of Karuppusamy et al. (2010). Right: Cumulative distribution of amplitudes grater than S, measured in units of mean amplitudes of the main or interpulse phase windows, reported by Cognard et al. (1996). The solid line represents a best fit power-law function. This figure is taken from Figure 3 of Cognard et al. (1996).

The second point is that the occurrence phases of GRPs are limited to the narrow region(s) within one rotational period. For example, the occurrence phases of GRPs in the Crab pulsar are limited to the main pulse and the interpulse phase, which are the two main components of the average profile (Cordes et al., 2004, see also Figure 2.2). In addition, it is also reported by (Cusumano et al., 2003) that the occurrence phases of GRPs in PSR B1937+21 were not aligned with the average profile, and were concentrated in the trailing edge of the mean radio profile, and roughly match the peak

phase of the mean X-ray profile. The occurrence phases of GRPs in PSR J0218+4232 were also not aligned with the average profile and roughly match the peak phase of the mean X-ray profile (Knight et al., 2006a). It may be suggested that the emission region of GRPs may be related to that at higher energy bands (Figure 2.3).

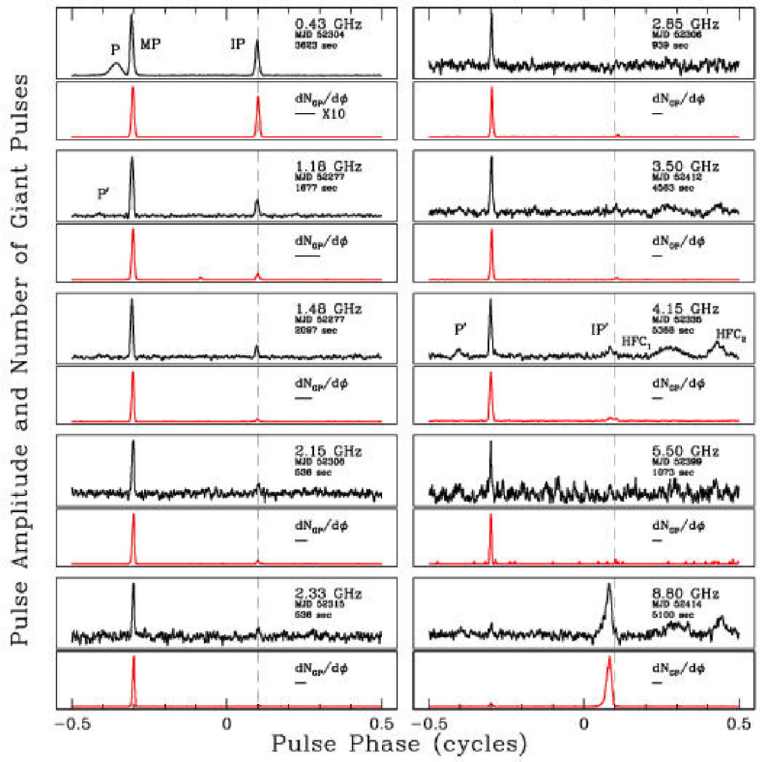

Fig. 2.2.— The average intensity profile (black) and the number counts of GRPs plotted against pulse phase (red) at each frequency band. This figure is taken from Figure 1 of Cordes et al. (2004).

At present, detection of GRPs is reported in fifteen pulsars. In Table 2.1, we summarize those pulsars. The Crab pulsar, PSR B0540-69 and the millisecond pulsars have relatively larger magnetic fields at the position of the light cylinder. It may be suggested that the emission mechanism of GRPs of those pulsars can be related to some process occurring in the outer region of the magnetosphere, which is thought to be the emission region of the high energy bands.

Some researchers reported the detection of GRPs from relatively slowly rotating pulsars. The magnetic fields at the light cylinder of those pulsars are much smaller than those of the Crab or the millisecond pulsars. The widths of the GRPs are ∼ms (e.g. Tsai et al., 2015), considerably longer than the GRPs from the Crab pulsar or the

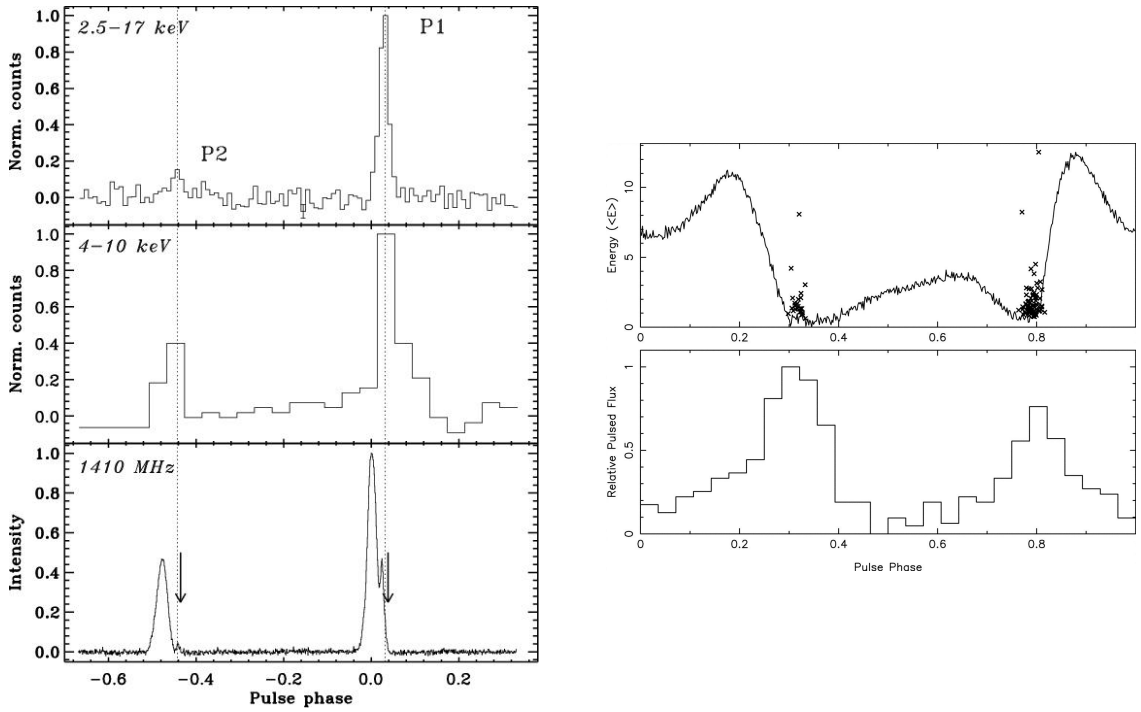

Fig. 2.3.— Left: Pulse profile of PSR B1937+21 in the 2-17 keV energy band (top), the 4-10 keV pulse profile (middle) and radio pulse profile at 1.6 GHz (bottom). Vertical arrows indicate the occurrence phases of the GRPs. This figure is taken from Figure 1 of Cusumano et al. (2003). Right: Phases and energies of GRPs detected from PSR J0218+4232 superimposed on an integrated pulse profile (top) and 0.08-10 keV pulse profile (bottom). This figure is taken from Figure 1 of Knight et al. (2006a).

millisecond pulsars. The GRPs from the slowly rotating pulsars have been observed only at relatively lower frequencies so far. On the other hand, the GRPs from those pulsars might have to be treated carefully. Gajjar et al. (2014) reported that they did not find GRPs from PSR J1752+2359 at 325MHz. Weltevrede et al. (2006) argued that strong pulses from PSR B0656+14 differ from GRPs based on their result that the pulse energy distribution follows a log-normal distribution rather than a power-law one. Crawford et al. (2013) also reported that they could not distinguish whether the intensity distribution of the GRPs from PSR J0529-6652 follows a power-law or a log-normal distribution. Weltevrede et al. (2006) or Karuppusamy et al. (2011) also mentioned that some of the "GRPs" from the ordinary pulsars might be some sort of RRAT-like emissions. RRAT (Rotating RAdio Transients) is one of the bursting neutron stars firstly discovered by McLaughlin et al. (2006). The RRAT is characterized as no detectable pulse for many hundreds of rotational periods followed by a bright detectable emission, and the underlying pulse period of it can be found by the long term observation (e.g. Lyne & Graham-Smith, 2012).

The Crab pulsar was discovered by GRPs (Stalin & Reifenstein, 1968). Since intensity variation of radio pulses from the Crab pulsar is larger than other pulsars, we can detect GRPs from the Crab pulsar more frequently than other pulsars (e.g. Knight et al., 2006a). Therefore, GRPs from the Crab pulsar have been investigated by many researchers since its discovery. GRPs from the Crab pulsar are detected at a wider frequency range than the other GRP pulsars, from 20 MHz (Ellingson et al., 2013) to 46 GHz (Hankins et al., 2015).

Some interesting features of Crab GRPs have been revealed by the observations with $\sim$ GHz bandwidths. Hankins et al. (2003) reported that the Crab MPGRPs were composed of a number of "nanoshots", and these nanoshots were suggested to be strongly circular polarized (see Figure 2.4). Hankins & Eilek (2007) and Jessner et al. (2010) also reported that the Crab IPGRPs were strongly linearly polarized.

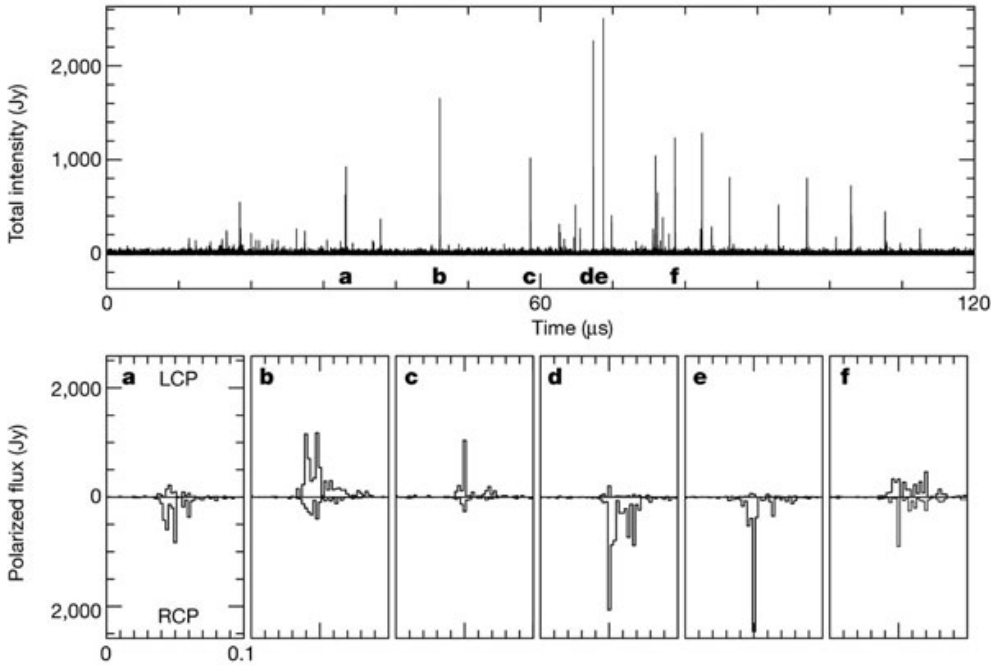

Fig. 2.4.— Intensity and polarization profiles of nanoshots reported by Hankins et al. (2003). The upper panel shows the intensity profile of a GRP plotted with 2-ns resolution. The polarized flux from six of the nanoshots corresponding to the sections shown by the name a-f in the upper panel plotted with 100-ns duration are plotted in the lower panel also with 2-ns resolution.

In the Crab GRPs, some peculiar features in the spectral structures have also been reported. According to the dynamic spectrum[2] of GRPs detected at 8 - 10 GHz (Figure

[2]A two dimensional image of pulse intensity as a observation time and frequency (Lorimer & Kramer,

2.5) reported by Hankins & Eilek (2007), the "emission band" structures were seen in the dynamic spectra of the IPGRPs, while similar structures were not found in the dynamic spectra of the MPGRPs. The origin of the band structure has not yet been resolved, but Lyutikov (2007) constructed the theoretical model to explain the structure (Section 2.3.2).

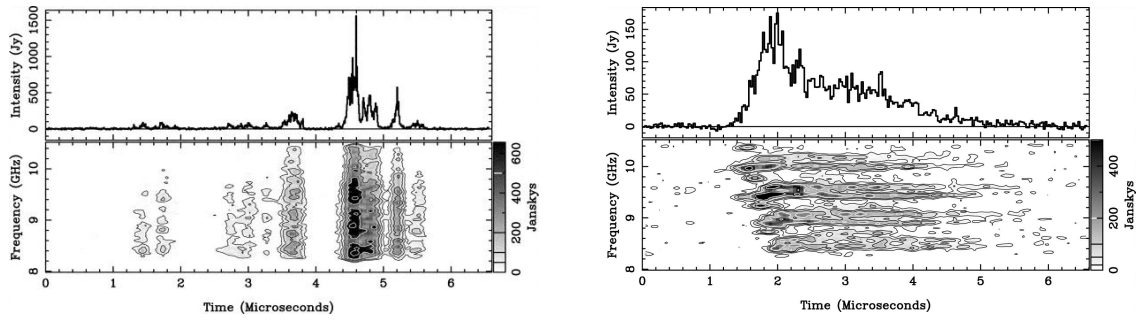

Fig. 2.5.— Total intensity profiles (top) and their dynamic spectra (bottom) for the typical MPGRPs (left) and IPGRPs (right) at 8 - 10 GHz reported by Hankins & Eilek (2007). The dispersive delay (see Section 3.1) is corrected. In the dynamic spectra, flux density is drawn with contours.

The spectra of the Crab GRPs are also investigated by the simultaneous multi-frequency observations. This subject will be discussed in Chapter 4.

From the Crab pulsar, pulsed emission is also detected at the energy bands higher than the radio band, such as optical, X-ray and γ-ray bands (Abdo et al., 2010, see also Figure 2.6). Simultaneous observations of the Crab GRPs and the pulses at higher energy bands may give a clue to the emission mechanism of GRPs. In the Crab pulsar, optical pulses concurrent with GRPs are on average $\sim$ 3% brighter than those not coincident with GRPs (Shearer et al., 2003; Strader et al., 2013). These results suggest that GRPs have some correlation with the emission at higher energy bands. We will discuss more details of this subject in Chapter 5.

2.3.2 Theoretical models of GRPs

Several theoretical models of GRPs have been proposed so far. Petrova (2004) proposed the model that GRPs are generated by the process of induced Compton scattering of radio emission off the plasma particles in the pulsar magnetosphere. Gil & Melikidze (2005) argued that GRPs can be explained by the angular beaming effect due to the relativistic motion of the emitting sources. Lyutikov (2007) argued that GRPs are

2004). See also Figure 3.1.1

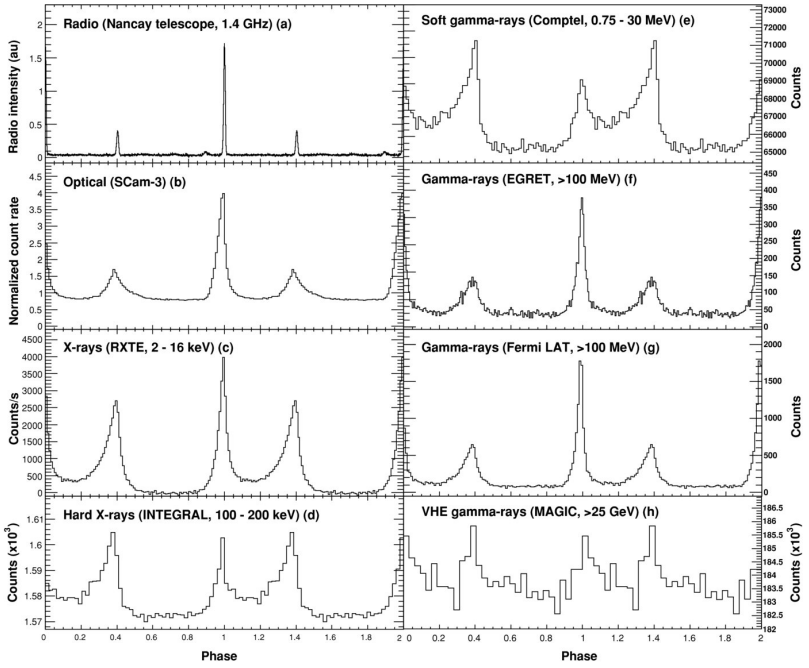

Fig. 2.6.— Average pulse profiles of the Crab pulsar from radio to very high energy γ-ray band. At each frequency band, two cycles of pulse profiles are drawn repeatedly. This figure is taken from Figure 2 of Abdo et al. (2010).

generated by the process of anomalous cyclotron resonance on the L/O-mode waves. Below, we describe the model proposed by Lyutikov (2007).

The model proposed by Lyutikov (2007) intends to explain the band structure (similar to Figure 2.5) in the dynamic spectrum of the GRPs at ~ 8 GHz reported by Eilek & Hankins (2007). He suggested that the separations of those bands came from the anomalous cyclotron resonance (e.g. Terasawa & Matsukiyo, 2012) between the L/O-mode waves and the plasmas in the pulsar magnetosphere. He fitted the separation of the band structure in the dynamic spectrum reported by Eilek & Hankins (2007) to the resonant frequencies for anomalous cyclotron resonance. From the derived parameters by the fit, he made a suggestion that the required Lorentz factor of the plasma particles, $\gamma \sim 10^7$, can be obtained by the magnetic reconnection in the Y-point of the pulsar magnetosphere and those accelerated particles could emit curvature radiation in γ-rays. Therefore, they argued that enhanced γ-ray emission accompanied with GRPs might be found. This is important for a correlation study between Crab GRPs and γ-ray pulses. Bilous et al. (2011) and Mickaliger et al. (2012) investigated a correlation between them

Table 2.1: Some basic data of the pulsars from which detection of GRPs has been reported. The data of pulse period P, Distance, period mean flux density at 400 MHz and 1400 MHz $S_{400/1400}$ and the magnetic field at the position of the light cylinder of each pulsar are taken from the ATNF pulsar catalogue (Manchester et al., 2005). "Freq." is the frequency at which detection of GRPs has been reported.

Name	P [ms]	Dist. [kpc]	Freq. [GHz]	S_{400} [mJy]	S_{1400} [mJy]	B_{LC} [G]
B0531+21 (J0534+2200)	33	2	0.02[a]-46[b]	550	14	9.55×10^5
B0540-69 (J0540-6919)	50	48.1	1.4[c]	0.0007	0.024	3.62×10^5
B1937+21 (J1939+2134)	1.56	4.6	0.1[d]-2.4[e]	240	13.2	1.02×10^6
B1821-24A (J1824-2452A)	3.05	4.9	0.8[f]-3.5[g]	40	2.0	7.40×10^5
J0218+4232	2.32	5.85	0.9,1.4[h]	57.7	0.9	3.21×10^5
B1957+20 (J1959+2048)	1.61	1.53	0.8[h]	20	0.4	3.76×10^5
B1820-30A (J1823-3021A)	5.44	7.9	0.7[i],1.4[j]	16	0.72	2.52×10^5
B1112+50 (J1115+5030)	1656	0.54	0.1[k]	5.3	3	4.24
B0031-07 (J0034-0721)	943	1.08	0.04[l],0.1[m]	52	11	7.02
J1752+2359	409	2.7	0.1[n]	3.5	*	71.1
B0656+14 (J0659+1414)	385	0.29	0.1[o]	6.5	3.7	766
B0950+08 (J0953+0755)	253	0.26	0.04[p], 0.1[q]	400	84	141
B0529-66 (J0529-6652)	976	53.7	1.4[r]	*	0.3	39.7
B1237+25 (J1239+2453)	1382	0.84	0.1[s]	110	10	4.14
B1133+16 (J1136+1551)	1188	0.35	0.1[t]	257	32	11.9

[References. a: (Ellingson et al., 2013), b: (Hankins et al., 2015), c: (e.g. Johnston & Romani, 2003), d: (Kuzmin & Losovsky, 2002), e: (Kinkhabwala & Thorsett, 2000), f: (Bilous et al., 2015), g: (Knight et al., 2006b), h: (Knight et al., 2006a), i: (e.g. Knight, 2007), j: (Knight et al., 2005), k: (Ershov & Kuzmin, 2003), l: (Kuzmin & Ershov, 2004), m: (e.g. Kuzmin et al., 2004), n: (Ershov & Kuzmin, 2005), o: (Kuzmin & Ershov, 2006), p: (Tsai et al., 2015), q: (e.g. Singal & Vats, 2012), r: (Crawford et al., 2013), s: (Kazantsev & Potapov, 2015a), t: (Kazantsev & Potapov, 2015b)]

by the simultaneous observations at radio and γ-ray bands with the *Fermi* satellite, but no significant enhancement has been found so far (see also Chapter 5).

Chapter 3

Radio Observation and Data Analysis

In this chapter, some basic principles and techniques in pulsar radio observations are reviewed.

3.1 The Dispersion Effect and the Dedispersion Technique

3.1.1 Dispersion effect

Here, we consider a (transverse) electromagnetic wave propagating to x-direction in unmagnetized plasma. The electric and magnetic field consisting of the wave is described as $\mathbf{E}$ and $\mathbf{B}$, respectively. The equation of motion of the plasma particles are described as:

$$\frac{\partial \mathbf{v}_e}{\partial t} + \mathbf{v}_e \cdot \nabla \mathbf{v}_e = -\frac{e}{m_e}\mathbf{E} - \frac{e}{m_e c}\mathbf{v}_e \times \mathbf{B}. \tag{3.1}$$

The Maxwell's equations are described as:

$$\mathrm{rot}\mathbf{B} - \frac{\partial \mathbf{E}}{c\partial t} = \frac{4\pi}{c}\mathbf{j} = -\frac{4\pi}{c} n_0 e \mathbf{v}_e, \tag{3.2}$$

and

$$\mathrm{rot}\mathbf{E} + \frac{\partial \mathbf{B}}{c\partial t} = \mathbf{0}. \tag{3.3}$$

By assuming that the velocities of the electrons are initially zero and neglecting the nonlinear terms such as $\mathbf{v}_e \cdot \nabla \mathbf{v}_e$ or $\mathbf{v}_e \times \mathbf{B}$, we get the following equation from Equation (3.1),

$$\frac{\partial \mathbf{v}_e}{\partial t} \simeq -\frac{e}{m_e}\mathbf{E}. \tag{3.4}$$

Taking only the y-component, we get

$$\frac{\partial v_{ey}}{\partial t} = -\frac{e}{m_e} E_y. \tag{3.5}$$

From the y-component of Equation (3.2) and the z-component of Equation (3.3), we get

$$-\frac{\partial B_z}{\partial x} - \frac{\partial E_y}{c\partial t} = -\frac{4\pi n_0 e}{c} v_{ey}, \tag{3.6}$$

and

$$\frac{\partial E_y}{\partial x} + \frac{\partial B_z}{c\partial t} = 0, \tag{3.7}$$

respectively. For the quantities v_{ey}, E_y and B_z taking a from of $\propto \exp\{i(kx - \omega t)\}$, a set of equations for those three parameters is described as follows,

$$\begin{Bmatrix} -i\omega & \frac{e}{m_e} & 0 \\ \frac{4\pi n_0 e}{c} & \frac{i\omega}{c} & -ik \\ 0 & ik & -\frac{i\omega}{c} \end{Bmatrix} \begin{Bmatrix} v_{ey} \\ E_y \\ B_z \end{Bmatrix} = \mathbf{0}. \tag{3.8}$$

The condition that (3.8) has a non-trivial solution is :

$$-i\omega \left(\frac{\omega^2}{c^2} - k^2 - \frac{4\pi n_0 e^2}{m_e c^2} \right) = 0. \tag{3.9}$$

From the equation above, we obtain the following dispersion relation :

$$\omega^2 = c^2 k^2 + \omega_{pe}^2. \tag{3.10}$$

Here, we define the "plasma frequency" as

$$\omega_{pe} \equiv \left(\frac{4\pi n_0 e^2}{m_e} \right)^{1/2}. \tag{3.11}$$

The "group velocity" V_g is calculated as,

$$V_g = \frac{\partial \omega}{\partial k} = \left(\frac{\partial k}{\partial \omega} \right)^{-1} = c\sqrt{1 - \frac{\omega_{pe}^2}{\omega^2}}. \tag{3.12}$$

Therefore, the time T that is taken for pulses with the angular frequencies $\omega = 2\pi f$ to propagate along a path of length L is

$$T = \int_0^L \frac{ds}{V_g} = \int_0^L \frac{ds}{c\sqrt{1 - \frac{\omega_{pe}^2}{\omega^2}}}. \tag{3.13}$$

For the observing frequency f satisfying $f \gg f_{pe}$,

$$T \simeq \int_0^L \frac{1}{c}\left[1+\frac{1}{2}\frac{\omega_{pe}^2}{\omega^2}\right] ds = \frac{L}{c} + \frac{2\pi e^2}{m_e c}\frac{1}{\omega^2}\int_0^L n_0 ds = \frac{L}{c} + \frac{e^2}{2\pi m_e c}\frac{1}{f^2}\int_0^L n_0 ds. \quad (3.14)$$

We define the "dispersion measure" (DM) as

$$DM \equiv \int_0^L n_0 ds. \quad (3.15)$$

From Equation (3.14), difference in the arrival times of pulses with the frequencies (f_1, f_2) is describes as follows;

$$\Delta t \simeq \frac{e^2}{2\pi m_e c}\left(\frac{1}{f_1^2} - \frac{1}{f_2^2}\right) DM. \quad (3.16)$$

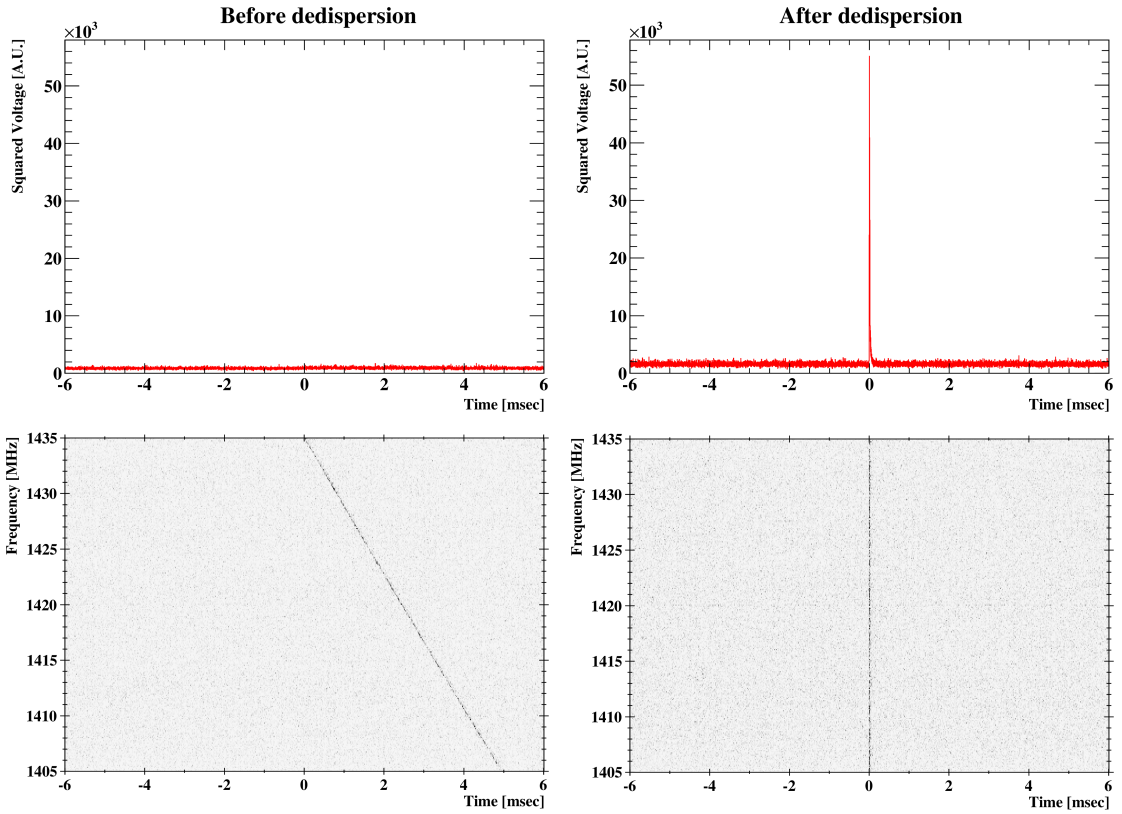

Fig. 3.1.— Example of the pulse profile (top) and the dynamic spectrum (bottom) of a Crab GRP. The non-dedispersed intensity is shown in the left panel, and the dedispersed intensity is shown in the right panel. In the left panel, the dispersion effect can be clearly seen in the dynamic spectrum and the GRP is not seen in the intensity profile. By the dedispersion procedure, the GRP is clearly seen.

3.1.2 Basic principles of the dedispersion procedure

Signals are affected by the dispersion effects described in the previous section. The way to recover the pulse profile at the source position is to divide the frequency band into many independent "channels" and appropriately shift the time samples so that the pulses at each frequency band arrive at the same time. This dedispersion technique is often called a "incoherent dedispersion" (e.g. Lorimer & Kramer, 2004). Another way to correct the dispersion effect is a "coherent dedispersion", which is based on the fact that the delay caused by the interstellar dispersion can be represented as a phase rotation depending on frequency (e.g. Lorimer & Kramer, 2004). Below, we describe a basic principle of the coherent dedispersion.

We represent the signal unaffected by the dispersion effect as $\hat{V}_0(t)$, and its fourier transform is represented as $\hat{V}_0(\omega)$. These signals can be regarded as the signals at the source position. These two quantities satisfy the following relation;

$$\hat{V}_0(t) = \int \hat{V}_0(\omega)\exp\left(i\omega t\right) d\omega. \tag{3.17}$$

Taking into account propagation of the signal over a distance D, $\hat{V}(t)$ is described as

$$\hat{V}(t) = \int \hat{V}_0(\omega)\exp\left\{i\omega t - ik(\omega)D\right\} d\omega. \tag{3.18}$$

$\hat{V}(t)$ is also represented by using a fourier transform as follows;

$$\hat{V}(t) = \int \hat{V}_{\rm obs}(\omega)\exp\left(i\omega t\right) d\omega. \tag{3.19}$$

Therefore, from Equation (3.18)、(3.19), we get

$$\hat{V}_0(\omega) = \hat{V}_{\rm obs}(\omega)\exp\left\{ik(\omega)D\right\}. \tag{3.20}$$

Therefore, $\hat{V}_0(t)$ is reproduced from the observed data and Equation (3.17),

$$\hat{V}_0(t) = \int \hat{V}_{\rm obs}(\omega)\exp\left\{ik(\omega)D\right\}\exp\left(i\omega t\right) d\omega. \tag{3.21}$$

The dispersion relation for the electromagnetic wave in cold plasma is described as;

$$\omega = \sqrt{c^2k^2 + \omega_{pe}^2}, k = \frac{\sqrt{\omega^2 - \omega_{pe}^2}}{c}. \tag{3.22}$$

See Equation (3.10). In the case of $\omega \gg \omega_{pe}$, the wave number $k(\omega)$ is approximated as follows;

$$k(\omega) = \frac{\omega}{c}\left(1 - \frac{\omega_{pe}^2}{\omega^2}\right)^{1/2} \sim \frac{\omega}{c}\left(1 - \frac{\omega_{pe}^2}{2\omega^2}\right) = \frac{\omega}{c} - \frac{\omega_{pe}^2}{2c\omega}. \tag{3.23}$$

Using a "frequency" $f = \omega/2\pi$ and a wavelength (in vacuum) $\lambda = c/f = 2\pi c/\omega$ instead of ω, Equation (3.23) is also represented as;

$$k(\omega) \sim \frac{2\pi}{\lambda} - \frac{e^2}{m_e c} n_e \left(\frac{1}{f}\right). \tag{3.24}$$

Therefore, Equation (3.21) is also represented as;

$$\begin{aligned} \hat{V}_0(t) &= \int \hat{V}_{\rm obs}(\omega) \exp\left\{ i\frac{2\pi D}{\lambda} - iD\frac{e^2}{m_e c} n_e \left(\frac{1}{f}\right)\right\} \exp\left(i\omega t\right) d\omega \\ &= \int \hat{V}_{\rm obs}(\omega) \exp\left\{ i2\pi f \left(t + \frac{D}{c}\right) - i2\pi\alpha D n_e \left(\frac{1}{f}\right)\right\} d\omega. \end{aligned} \tag{3.25}$$

Here, we define a constant α as;

$$\alpha \equiv \frac{e^2}{2\pi m_e c}. \tag{3.26}$$

Dn_e in Equation (3.25) is Dispersion Measure defined in the previous section (see equation 3.15). When D is represented in unit "pc" (parsec) and n_e in unit cm^{-3}, it is convenient to write

$$\alpha \simeq 4.15 \times 10^9 [\mathrm{MHz} \cdot \mathrm{pc}^{-1} \cdot \mathrm{cm}^3]. \tag{3.27}$$

The term $t + D/c$ appearing in the integrand in Equation (3.25) represents the time-shift according to the propagation delay. When we define the time at the "source position" $\tilde{t} = t - D/c$, and regard $\hat{V}_0$ as a function of $\tilde{t}$, Equation (3.25) becomes a more simplified form;

$$\hat{V}_0(\tilde{t}) = \int \hat{V}_{\rm obs}(\omega) \exp\left\{ i2\pi f\tilde{t} - i2\pi\alpha D n_e \left(\frac{1}{f}\right)\right\} d\omega. \tag{3.28}$$

3.1.3 Coherent dedispersion procedure in our analysis

In this section, we apply the dedispersion procedure described in the previous section to the data in our observation. In our observation, a signal received from the antenna is converted to a digitized one. We define the sampling time of the digitized data as Δt. In other words, the data is sampled at the time $t_n = n\Delta t$ $(n = 0, 1, \cdots, N-1)$ when we process of the data with duration $T \equiv N\Delta t$. On the other hand, frequency resolution of this data is represented as $\Delta f = 1/T$ and the expression in a frequency space is discrete one; $f_k = k\Delta f$, where $-(N_{\rm Nyq} - 1) \leq k \leq N_{\rm Nyq}$ and $N_{\rm Nyq} = N/2$ corresponding to the Nyquist frequency.

The fourier transformation is rewritten in a discrete manner;

$$\hat{q}_{\rm obs}(f_k) = \frac{1}{N} \sum_{n=0}^{N-1} Q_{\rm obs}(t_n) \exp\left(-i2\pi f_k t_n\right) \tag{3.29}$$

$$Q_{\rm obs}(t_n) = \sum_{k=-(N_{\rm Nyq}-1)}^{N_{\rm Nyq}} \hat{q}_{\rm obs}(f_k) \exp\left(+i2\pi f_k t_n\right), \tag{3.30}$$

where $Q_{\rm obs}(t_n)$ is a digitized voltage output, and $\hat{q}_{\rm obs}(f_k)$ is its fourier pair. In the procedure of dedispersion, we introduce the complex sampled data $\hat{P}_{\rm obs}(t_n)$ and its fourier pair $\hat{p}_{\rm obs}(f_k)$ for convenience;

$$\hat{p}_{\rm obs}(f_k) = \begin{cases} 2\hat{q}_{\rm obs}(f_k) & [0 < f_k < f_{N_{\rm Nyq}}] \\ \hat{q}_{\rm obs}(0) & [f_k = 0] \\ \hat{q}_{\rm obs}(f_{N_{\rm Nyq}}) & [f_k = f_{N_{\rm Nyq}}] \\ 0 & [f_k < 0] \end{cases} \tag{3.31}$$

$$\hat{P}_{\rm obs}(t_n) = \sum_{k=0}^{N_{\rm Nyq}} \hat{p}_{\rm obs}(f_k) \exp\left(+i2\pi f_k t_n\right) \tag{3.32}$$

Using the expression $\hat{p}_{\rm obs}(f_k)$ obtained in Equation (3.31), Equation (3.28) is rewritten as;

$$\hat{P}_0(\tilde{t}_n) = \sum_{k=0}^{N_{\rm Nyq}} \hat{p}_{\rm obs}(f_k) \exp\left\{+i2\pi f_k \tilde{t}_n - i2\pi\alpha D n_e \frac{1}{f_k}\right\}. \tag{3.33}$$

If the frequency coverage in the data is limited to a finite range (here, $f_{\rm min} \leq f_k \leq f_{\rm max}$), the sum in Equation (3.33) is limited to the range $k_{\rm min} \leq k \leq k_{\rm max}$ corresponding to the frequency range. In this case, we get

$$\hat{P}_0(\tilde{t}_n) = \sum_{k=k_{\rm min}}^{k_{\rm max}} \hat{p}_{\rm obs}(f_k) \exp\left\{+i2\pi f_k \tilde{t}_n - i2\pi\alpha D n_e \frac{1}{f_k}\right\}. \tag{3.34}$$

In this thesis, all of the data described in Chapter 4 are analyzed using Equation (3.33), and all of the data described in Chapter 5 are processed using Equation (3.34).

Here, we consider a quantity $\phi(f_k) \equiv -2\pi\alpha D n_e \frac{1}{f_k}$ in Equation (3.34). From the concept of geometric series, we get

$$\sum_{l=0}^{\infty} \left(\frac{f_{k_{\rm max}} - f_k}{f_{k_{\rm max}}}\right)^l = \frac{1}{1 - \frac{f_{k_{\rm max}} - f_k}{f_{k_{\rm max}}}} = \frac{f_{k_{\rm max}}}{f_k}. \tag{3.35}$$

Therefore, we get

$$\frac{1}{f_k} = \frac{1}{f_{k_{\rm max}}} \sum_{l=0}^{\infty} \left(\frac{f_{k_{\rm max}} - f_k}{f_{k_{\rm max}}}\right)^l. \tag{3.36}$$

Separating the first term and the other terms in Equation (3.36), we get

$$\frac{1}{f_k} = \frac{1}{f_{k_{\rm max}}} \left\{1 + \frac{f_{k_{\rm max}} - f_k}{f_{k_{\rm max}}}\right\} + \frac{1}{f_{k_{\rm max}}} \sum_{l=2}^{\infty} \left(\frac{f_{k_{\rm max}} - f_k}{f_{k_{\rm max}}}\right)^l$$

$$
\begin{aligned}
&= \frac{2}{f_{k_{\max}}} - \frac{f_k}{f_{k_{\max}}^2} + \left(\frac{f_{k_{\max}} - f_k}{f_{k_{\max}}}\right)^2 \frac{1}{f_{k_{\max}}} \sum_{l=0}^{\infty} \left(\frac{f_{k_{\max}} - f_k}{f_{k_{\max}}}\right)^l \\
&= \frac{2}{f_{k_{\max}}} - \frac{f_k}{f_{k_{\max}}^2} + \frac{\left(f_{k_{\max}} - f_k\right)^2}{f_{k_{\max}}^2 f_k}, \qquad (3.37)
\end{aligned}
$$

where in the last equality, we use the expression derived in Equation (3.35). Therefore, we obtain

$$
\phi(f_k) = -\frac{4\pi\alpha D n_e}{f_{k_{\max}}} + \frac{2\pi\alpha D n_e}{f_{k_{\max}}^2} f_k - 2\pi\alpha D n_e \frac{\left(f_{k_{\max}} - f_k\right)^2}{f_{k_{\max}}^2 f_k}. \qquad (3.38)
$$

Here, we pay attention to the three terms in Equation (3.38),

$$
\Phi_0 \equiv -\frac{4\pi\alpha D n_e}{f_{k_{\max}}}, \qquad (3.39)
$$

$$
\Phi_1 \equiv \frac{2\pi\alpha D n_e}{f_{k_{\max}}^2}, \qquad (3.40)
$$

and

$$
\delta\phi(f_k) \equiv -2\pi\alpha D n_e \frac{\left(f_{k_{\max}} - f_k\right)^2}{f_{k_{\max}}^2 f_k}. \qquad (3.41)
$$

Using these expressions, $\phi(f_k)$ is rewritten as;

$$
\phi(f_k) = \Phi_0 + \Phi_1 f_k + \delta\phi(f_k). \qquad (3.42)
$$

Equation (3.34) is simplified with (3.39), (3.40) and (3.41) as follows;

$$
\hat{V}_0(\tilde{t}_n) = \exp(i\Phi_0) \sum_{k=k_{\min}}^{k_{\max}} \hat{p}_{\rm obs}(f_k) \exp\left\{+i2\pi f_k \left(\tilde{t}_n + \frac{\Phi_1}{2\pi}\right)\right\} \exp\left(i\delta\phi(f_k)\right). \qquad (3.43)
$$

The quantity in our interest is a "squared" voltage, which is equivalent to power or flux density. $\exp(i\Phi_0)$ is a constant phase offset and is not affected by calculating a squared voltage. According to the shift theorem, the term is a shift in the time domain. This term is the additional propagating time due to an existence of plasma. Since we are not interested in the pulse "emitted" time at the source, this term can be neglected in the data processing. Therefore, the coherent dedispersion procedure can be described as the following expression;

$$
\hat{P}_0(\tilde{t}_n) = \sum_{k=k_{\min}}^{k_{\max}} \hat{p}_{\rm obs}(f_k) \exp\left(i\delta\phi(f_k)\right) \exp\left(+i2\pi f_k \tilde{t}_n\right) \qquad (3.44)
$$

Using the equation above, we can correct phase rotations corresponding to the frequency dependent delays within our observing frequency band. The factor $\exp\left(i\delta\phi(f_k)\right)$ corresponds to the transfer function, H described in (e.g. Hankins & Rickett, 1975; Lorimer & Kramer, 2004).

3.2 Timing Analysis

3.2.1 Transformation to the time at the Solar system barycenter

In order to compare the pulse TOAs (Times Of Arrival) in the common inertial reference frame, we often covert the pulse TOAs at each observatory (often called the "topocentric arrival times" Lorimer & Kramer (2004)) to Barycentric Dynamical Time (TDB) at the Solar system barycenter (hereafter SSB). The transformations of TOAs are summarized as follows (e.g. Lorimer & Kramer, 2004);

$$t_{\rm SSB} = t_{\rm topo} + \Delta t_{\rm frame} + \Delta t_{\rm D} + \Delta t_{\rm R} + \Delta t_{\rm S} + \Delta t_{\rm E} \tag{3.45}$$

$\Delta t_{\rm frame}$ is the conversion of the time standard. If TOAs of pulses are recorded in Coordinated Universal Time (UTC), UTC is related to TAI (International Atomic Time) by the following relation;

$$\mathrm{TAI} = \mathrm{UTC} + (\text{number of leap seconds}). \tag{3.46}$$

where leap seconds are inserted into UTC so that the difference between UTC and UT1[1] does not exceed 0.9 second. The TAI is maintained by a number of atomic clocks Bureau International des Poids et Mesures (BIPM). TAI is related to TT (Terrestrial Time) by the following relation;

$$\mathrm{TT} = \mathrm{TAI} + 32.184\mathrm{s}. \tag{3.47}$$

The purpose of the offset of 32.184 seconds is to maintain continuity between TT and ET (Ephemeris Time)[2]. Therefore, if pulse TOAs are recorded in UTC,

$$\Delta t_{\rm frame} = (\text{number of leap seconds}) + 32.184\mathrm{s}. \tag{3.48}$$

$\Delta t_{\rm D}$ represents the correction for the dispersive delay described in Section 3.1. $\Delta t_{\rm R}$ represents the correction for the Römer delay, which is the vacuum light travel time between the telescope and the SSB. $\Delta t_{\rm S}$ represents the correction for the Shapiro delay due to the objects in the Solar System, which is the delay caused by propagating with an existence of massive objects. $\Delta t_{\rm E}$ represents the correction for the Einstein delay, which

[1]The timescale determined by the rotation of the Earth. Because of the non-uniform rotation of the Earth, the rate of UT1 is not constant.

[2]e.g. Recommendation IV of Resolution A4 of the XXIst General Assembly of the IAU in 1991 at Buenos Aires,
https://www.iau.org/static/resolutions/IAU1991_French.pdf

is due to the annual variation in the clock rate on Earth. When the TOAs of the pulses from the binary pulsars are treated, the additional corrections accompanied with an existence of the companion star (the additional Römer delay due to the binary motion, the Shapiro delay caused by the companion star, etc.) will be taken into account. Other effects, for example the additional Römer delay due to a proper motion of the pulsar should be corrected, but it is negligible for an one-day observation and is neglected in our work. We can relatively easily carry out the transformation procedures described above with some packages. In our analysis, we used a package "TEMPO2" (Hobbs et al., 2006) for the radio data, and the FTOOLS task "aebarycen" for the X-ray data (Blackburn, 1995).

3.2.2 Folding procedure

Since each pulse signal are usually very weak, a number of pulse signals are added in order that we can see a clear pulse profile exceeding the background noise. This procedure is called the "folding" (Lorimer & Kramer, 2004). The outline of the folding is described as follows; (1) Carry out the dedispersion of the data (see Section 3.1). (2) Create an array with N equally spaced elements (which we refer to as "phase bins" hereafter) across the pulse period to store the dedispersed data (squared voltage). (3) Calculate the phase relative to the pulse period from the data time. (4) Find the appropriate phase bin which is closest to the calculated phase, and add the dedispersed data in this phase bin. (5) Normalize each phase bin in the obtained pulse profile by the number of data samples accumulated per bin.

The obtained pulse profiles in our observation are displayed in Figure 3.2. This folding procedure can be also applied to the X-ray data. The obtained X-ray pulses will be shown in Chapter 5. However, GRPs are much stronger than noise levels and we can see GRPs without the folding procedure (Figure 1).

3.3 Flux Calibration and Estimation

3.3.1 Definition of some basic quantities

The infinitesimal power dP crossing an infinitesimal surface $d\sigma$ is

$$dP = I_\nu \cos\theta d\Omega d\sigma d\nu, \tag{3.49}$$

where $d\nu$ is an infinitesimal bandwidth, θ is the angle and I_ν is called brightness or (specific) intensity (Wilson et al., 2013).

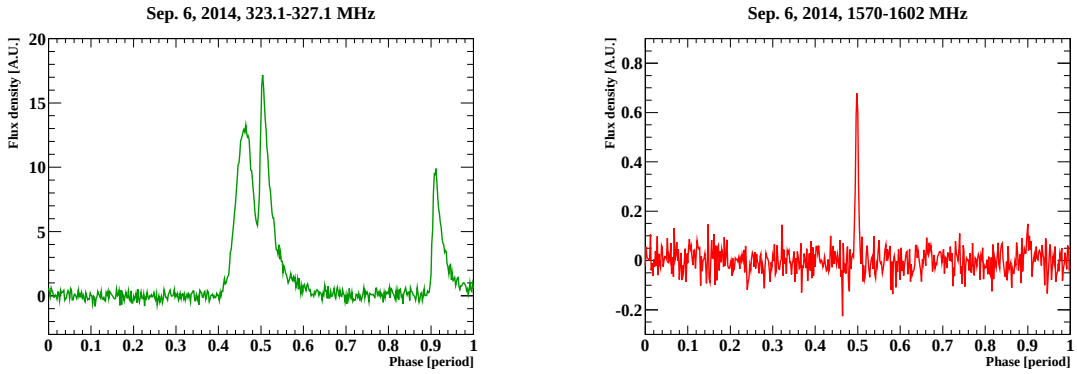

Fig. 3.2.— Folded pulse profiles obtained during the observation of the Crab pulsar on September 6-7, 2014. Left: the 323.1 - 327.1 MHz (P band) profile from the data acquired in the Iitate planetary radio telescope. Right: the 1570 - 1602 MHz (LL band) profile from the data acquired in the Kashima 34 m antenna. The main pulse (MP) component can be seen at the phase ~ 0.5, and the interpulse (IP) component can be seen at the phase ~ 0.9. At P band, the precursor component (e.g. Moffett & Hankins, 1996) can be seen at the phase ~ 0.45.

The total flux density of a source S_ν is obtained by integrating Equation (3.49) over the solid angle Ω_S subtended by the source

$$S_\nu = \int_{\Omega_S} I_\nu \cos\theta d\Omega. \tag{3.50}$$

The flux density is measured in units of W m^{-2} Hz^{-1}, erg s^{-1} cm^{-2} Hz^{-1} or the "Jansky (Jy)" which satisfies the relation

$$1\mathrm{Jy} = 10^{-26}\mathrm{Wm}^{-2}\mathrm{Hz}^{-1} = 10^{-23}\mathrm{erg\ s}^{-1}\mathrm{cm}^{-2}\mathrm{Hz}^{-1}. \tag{3.51}$$

The brightness temperature is the temperature which a blackbody should have so as to reproduce the observed intensity of an object at frequency ν (e.g. Burke & Graham-Smith, 2010). The intensity of black body radiation $I_{\nu,BB}(T)$ at a certain frequency ν is represented as

$$I_{\nu,BB}(T) = \frac{2h\nu^3}{c^2}\frac{1}{\exp(h\nu/k_BT) - 1}, \tag{3.52}$$

where k_B is the Boltzmann constant, h is the Planck constant, and c is the speed of light. In the Rayleigh-Jeans regime ($h\nu \ll k_BT$), Equation (3.52) can be written approximately

$$I_{\nu,BB}(T) \simeq \frac{2h\nu^3}{c^2} \cdot \frac{k_BT}{h\nu} = \frac{2\nu^2 k_BT}{c^2}. \tag{3.53}$$

By using equation above, the brightness temperature T_b is defined as (e.g. Wilson et al., 2013)

$$T_b = \frac{c^2}{2k_B\nu^2} I_\nu. \tag{3.54}$$

Using flux density S_ν, T_b is also written as

$$T_b = \frac{c^2}{2k_B\nu^2\Omega}S_\nu, \tag{3.55}$$

where Ω is a solid angle.

When we observe a pulse with flux density S_ν at a frequency ν and duration Δt from the source at a distance of D, the size of the emission region must be smaller than $c\Delta t$. Therefore, the brightness temperature can be rewritten as (e.g. Lorimer & Kramer, 2004)

$$T_b \geq \frac{D^2}{2\pi k_B\nu^2(\Delta t)^2}S_\nu \sim 10^{29}\mathrm{K}\left(\frac{D}{1\mathrm{kpc}}\right)^2\left(\frac{\nu}{1\mathrm{GHz}}\right)^{-2}\left(\frac{\Delta t}{1\mu\mathrm{s}}\right)^{-2}\left(\frac{S_\nu}{1\mathrm{Jy}}\right). \tag{3.56}$$

The equality in Equation (3.56) is realized when the maximum source size is taken into account.

3.3.2 Antenna temperature and system equivalent flux density

According to Nyquist (1928), the power per unit frequency available at the terminal of a resistor P_ν is related to the temperature of the resistor T_r by the following relation,

$$P_\nu = k_B T_r. \tag{3.57}$$

If we replace an antenna with the resistor, the same relation is satisfied (e.g. Wilson et al., 2013). We define the antenna temperature T_A as follows;

$$T_A = \frac{P_\nu}{k_B}. \tag{3.58}$$

If we receive unpolarized emission of a certain source with an antenna of effective area A_e, received power $P_{\mathrm{r},\nu}$ is expressed as

$$P_{\mathrm{r},\nu} = \frac{1}{2}S_\nu A_e, \tag{3.59}$$

where the factor of $1/2$ is taken into account that each receiving element of an antenna is sensitive to one linear or circular polarization (e.g. Campbell, 2002; Wilson et al., 2013).

In a practical observation, there are many types of contributions to T_A. For example, the radiation from the atmosphere or noise generated by the antenna itself can be contributed to T_A. The galactic synchrotron radiation can be also contributed to the temperature T_A. The total contribution of noise to the system noise temperature, T_{sys}. Using T_{sys}, the system equivalent flux density (SEFD) is also defined as

$$\mathrm{SEFD} = \frac{2k_B T_{\mathrm{sys}}}{A_e}. \tag{3.60}$$

T_{sys} or SEFD is a measure of the sensitivity of a certain radio telescope system.

3.3.3 Flux calibration procedure

In order to determine flux density of a source, we have to determine SEFD. A straightforward way to estimate SEFD is to observe a stable radio source with well-known flux density $S_{\rm src}$, and to measure the received power in an "off-source" position near the source where no strong radio signal exists (Lorimer & Kramer, 2004). In Figure 3.3, we show the schematic image (left) and the real data (right) of change in received power during the observation in an on-/off- source position. As shown in the left of Figure

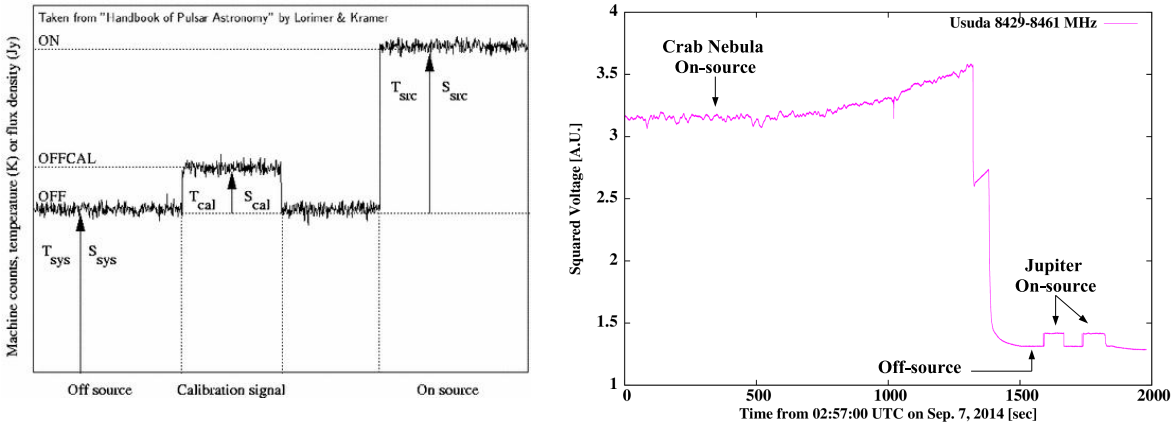

Fig. 3.3.— Left: Schematic picture showing the relationship between the received power (machine counts), antenna temperature and flux density during a typical system calibration measurement. This figure is taken from Figure 7.4 of Lorimer & Kramer (2004). Right: The received power during our observation on September 7, 2014. The received power of the Crab nebula (target source) and Jupiter (calibration source) are shown. Increase of the received power in the time interval from 700 to 1300 seconds is due to increase of a noise level associated with the observation at a low elevation angle.

3.3, the received power during the observation in an on-source position is proportional to the sum of the system noise and the source, while the received power during the observation in an off-source position is proportional to only the system noise. This means that

$$\frac{P_{\rm on} - P_{\rm off}}{P_{\rm off}} = \frac{S_{\rm src}}{\rm SEFD} \left(= \frac{T_{\rm src}}{T_{\rm sys}} \right), \tag{3.61}$$

where $P_{\rm on,off}$ is the received power in an on-/off-source position of the source. Therefore,

$$\rm SEFD = \frac{S_{src}}{\frac{P_{on}}{P_{off}} - 1}. \tag{3.62}$$

If we can estimate SEFD, then we can estimate flux density of the target source $S_{\rm src,t}$ by the on-/off-source observation of it with the SEFD estimated above, assuming that

SEFD during the observation of the calibration source is not different from the SEFD during the observation of the target source. Therefore,

$$S_{\mathrm{src,t}} = \mathrm{SEFD}\left(\frac{P_{\mathrm{on,t}}}{P_{\mathrm{off,t}}} - 1\right), \tag{3.63}$$

where $P_{\mathrm{on/off,t}}$ is the received power in an on-/off-source position of the target source.

Chapter 4

Wide-Band Spectra of the Giant Radio Pulses from the Crab Pulsar

4.1 Introduction

Simultaneous multi-frequency observations of GRPs give a number of clues to understand the emission mechanism of GRPs. Investigation of the GRP spectra is one of the important study making use of simultaneous multi-frequency observations. The spectra of the Crab GRPs have been investigated in several studies. Sallmen et al. (1999) showed that the spectral indices distribute between -4.9 and -2.2 for the GRPs simultaneously detected at 0.6 and 1.4 GHz. Oronsaye et al. (2015) also reported that the spectral indices of the GRPs simultaneously detected at 0.2 and 1.4 GHz distribute between -4.9 and -3.6. At 1.30–1.45 GHz, Karuppusamy et al. (2010) claimed that the spectral indices of the Crab GRPs were -1.4 ± 3.3 and -0.6 ± 3.5 for the GRPs occurring at the main pulse and the interpulse phases. They also reported that ~ 4000 GRPs were not detected at the frequency sub-bands of 1.30–1.45 GHz, which may imply a narrow-band spectral feature intrinsic to the GRPs. From a simultaneous observation at 0.6, 1.65 and 4.85 GHz, Popov et al. (2008) claimed that the GRP spectra seem to be bent harder with increasing frequency. Popov et al. (2009) also reported that the spectra became harder with frequency for 27 GRPs simultaneously detected at 0.6, 1.4 and 2.2 GHz. In those previous studies, spectral indices or shapes were investigated, but the relation between spectral indices and other quantities such as fluences has not yet been reported. In some studies, the numbers of samples were insufficient to discuss the statistical properties of the GRP spectra. In some studies, frequency separation is too small to discuss the global structure of the spectra. Our study is carried on in order to overcome those weak points.

In this chapter, we show the results of our simultaneous observation of the Crab GRPs at 0.3, 1.6, 2.2, 6.7 and 8.4 GHz with the four radio telescopes in Japan. The outline of our observation and data analysis are described in Section 4.2. Spectral analyses with about 3200 main pulse GRPs and about 250 interpulse GRPs at a frequency range from 0.3 to 2.2 GHz, are shown in Section 4.3. A large number of the GRPs have spectra consistent with single power-laws. We find a correlation between the spectral index and the total fluence in those samples. We also show some examples that apparently contradict with a single power-law. Wider spectra from 0.3 to 8.4 GHz are shown in Section 4.4. Our results are summarized with discussion in Section 4.5.

Recently, some researchers have reported the discovery of another sporadic phenomenon, fast radio bursts (FRBs) (e.g. Lorimer et al., 2007; Thornton et al. , 2013). FRBs are radio transients having a few millisecond duration, and they have high dispersion measures which exceed that expected from the interstellar medium of our own Galaxy. The origin of FRBs has been under debate (e.g. Kashiyama et al., 2013; Totani, 2013), but if they come from the extragalactic space, they can be used as a probe of the unknown extragalactic medium (e.g. Macquart et al., 2015). GRPs have similar characteristics to FRBs such as their time scales, and GRPs are discussed as one of the candidates of FRBs (Cordes & Wasserman, 2015; Connor et al., 2015). More recently, FRBs are observed at various frequency bands and some restriction of their spectra are being given (Karastergiou et al., 2015; Tingay et al., 2015). Therefore, revealing the spectral features of GRPs gives some information as a candidate of FRBs.

4.2 Observation and Analysis

Our radio wide-band observational campaign was conducted from UTC 14^h30^m on September 6 to 04^h00^m on September 7, 2014. Simultaneous observations at all observatories were overlapped from UTC 21^h35^m on September 6 to 02^h20^m on September 7. We summarize our observation in Tables 4.1 and 4.2. During the simultaneous observation period, calibration observations were intermittently made. The data for the periods when radio frequency interference (RFI) frequently appeared for Kashima 34m antenna were manually removed. As a result, the effective simultaneous observation time of the Crab GRPs is 2.9 hours.

Table 4.1: Observation summary.

Observatory anntena	start time[a] (duration)	center frequency $\nu_{k,c}$ [MHz] (band name)[b]		Bandwidth[c] $\Delta\nu$ [MHz] (bits/sample) Polarization[d]		SEFD[e] (Jy)	S^{f}_{CN} (Jy)	Selection threshold
Iitate 31m×16.5m, 2 asymetric offset dishes	15:10 (670min)	325.1 (P)		4(8) Linear[g]		1066-1326	1164±128	500μs, 5σ
Kashima 34m dish	14:30 (810min)	1586(L2)	≡ LL	32(4) R		422-543	816±16	10μs, 6σ
		1674(L6)	≡ LH	32(4) R	76	357-443	801±16	
		1696(L7)		32(4) R		400-549	797±16	10μs, 6σ
		1718(L8)		32(4) R		416-525	794±16	
Usuda 64m dish	20:50 (430min)	2198(S1)	≡ S	32(4)R	136	112-122	661±13	
		2224(S2)		32(4)R		106-116	657±13	
		2250(S3)		32(4)R		103-112	653±13	10μs, 6σ
		2276(S4)		32(4)R		102-111	648±13	
		2302(S5)		32(4)R		107-117	644±13	
		8445 (X)		32(4) R		100-110	125±15	1μs, 9σ
Takahagi 32m dish	14:30 (750min)	6672 (C)		16(4) L		289-359	406±9	1μs, 10σ

[a]UTC on September 6, 2014.

[b]L2 is renamed as LL. L6-8 and S1-5 are synthesized as LH and S, respectively (see section 4.2.1). The central frequencies after the synthesizing procedure is shown with underline.

[c]Effective bandwidth after the synthesizing procedure is shown with underline.

[d]R/L: Right/Left-Handed Circular Polarization.

[e]System equivalent flux density. Characteristic values during our observing session are shown.

[f]Received flux density of the Crab nebula. See Appendix A.

[g]Horizontal component.

Table 4.2: Observatory positions.

Obervatory	longitude	latitude
Iitate	140° 40'E	37° 42'N
Kashima	140° 40'E	35° 57'N
Usuda	138° 22'E	36° 08'N
Takahagi	140° 42'E	36° 42'N

The observation at 0.3 GHz (P band) was made with the Iitate Planetary Radio Telescope (IPRT), Tohoku University (Misawa et al., 2003; Tsuchiya et al., 2010). The telescope consists of two sets of asymmetric offset dish antennae of 31m×16.5m. To record the data, we used the K5/VSSP32 sampler (Kondo et al., 2003). The signal was 8-bit sampled at the Nyquist rate of 8 MHz with 4 MHz bandwidth. Only the horizontal polarization signal was recorded.

The GRP data for 1.4-1.6 GHz (L band) was obtained with the 34m telescope at the Kashima Space Research Center operated by the National Institute for Communication Technology (NICT). We recorded the data with the ADS3000+ recorder (Takefuji et al., 2010). The signals were digitized with 4-bit sample at the Nyquist rate of 64 MHz, and the data were divided into 8 ch (L1–L8) with 32 MHz bandwidths. Only the right-handed circular polarization (RHCP) signal was received at all the frequency channels. At Kashima observatory, to avoid RFI from cell phone base stations, a superconductor filter is installed. Nevertheless, frequent RFI occurred during our observation at some frequency channels. We use only the four channels of L2, L6, L7 and L8, which are less affected by the RFI in subsequent analysis.

The 64m telescope, belonging to the Usuda Deep Space Center of the Institute of Space and Astronautical Science (ISAS), took part in the observation at 2.2 GHz (S band) and 8.4 GHz (X band). The data acquisition system is the same as that in Kashima observatory; the ADS3000+ recorder and 4-bit samples with 8 ch × 32 MHz bandwidths at the Nyquist rate of 64 MHz. Seven channels of them were assigned to S band data (S1–S7), and the other one channel was used for X band data. Only the RHCP signal was received at all the frequency channels. Since the receiver sensitivities in S6 and S7 were insufficient, only the data for S1–S5 and X bands were analysed. At Kashima and Usuda observatories, sampling clocks were generated with hydrogen maser references. The recorded times in the two observatories were corrected to Coordinated Universal Time (UTC) in a subsequent off-line processing.

The Takahagi 32m antenna, which received the LHCP signals at 6.7 GHz (C band) with 16 MHz bandwidth, is a branch of Mizusawa VLBI observatory of National Astronomical Observatory of Japan. The K5/VSSP32 sampler recorded the data with 4-bit sample at the Nyquist rate of 32 MHz.

We determined the dispersion measure (DM) by aligning the peak times of some bright main pulse GRPs at the frequency channels of L band (L2, L6, L7 and L8) and S band (from S1 to S5). The times of arrival (TOAs) of the GRPs were converted to those at the solar system barycenter with the pulsar timing package TEMPO2 (Hobbs

et al., 2006). The accuracy of the TOAs in our analysis is within 1μs. According to the dispersion delay formula between frequencies f_1 and f_2,

$$\Delta t \simeq \frac{e^2}{2\pi m_e c}\left(\frac{1}{f_1^2}-\frac{1}{f_2^2}\right)\mathrm{DM}, \tag{4.1}$$

the DM value was determined as 56.764 pc/cm^3 in our observation period. The sampled data for each frequency channel were dedispersed with this DM value, based on the coherent dedispersion method (Hankins & Rickett (1975), Lorimer & Kramer (2004)).

4.2.1 GRP Selection

Below, we describe our methods of GRP selection. To extract real GRPs ,we set two criteria for GRP selection: 1) a peak S/N value of dedispersed data exceeds the threshold tabulated in Table 4.1, and 2) the signal appears at the rotational phase of the main pulse or interpulse.

We smoothed the time series of the dedispersed data for each channel with a time span tabulated in Table 4.1, which is adjusted to draw the typical GRP light curve with a few time-bins. From off-pulse phases, we obtained the noise flux, which is mainly due to the Crab nebula, and its average fluctuation. Based on those noise level and fluctuation, we calculated the signal-to-noise ratio (S/N) of the time series of the data. In order to improve the S/N and mitigate the effects of the interstellar scintillation (see Section 4.3), the data from the L6 to L8 channels, and the data from S1 to S5 channels were merged taking into account the overlaps of the frequency intervals of those channels. Hereafter, we call those merged frequency bands "LH band" and "S band", respectively. Between the LH band and the L2 band, there is a frequency gap. This separated L2 band is called "LL band". RFI and statistical fluctuations of the noise give rise to pseudo-signals.

The thresholds of the S/N for the GRP selection (hereafter, "selection thresholds") were determined to collect as many GRPs as possible and avoid contamination of pseudo-GRPs. The GRP candidates, whose peak S/N exceeds the selection threshold, are plotted in Figure 4.1 during a part of our observation period. We extracted the candidates within the appropriate phase ranges as GRP samples. For P, LL, LH and S bands, the main pulse and interpulse phases were empirically determined from the distribution of the GRP candidates in our samples. For LL, LH and S bands, the phase widths are 0.03 rotational period centering at the peak phases for both the main pulse and interpulse phase ranges. We shift the peak phases of the main pulse to 0.500 at these frequency bands. The width for P band is determined as 0.05 rotational period.

At C and X bands, the number of the candidates is too small to determine the phase ranges for the GRP selection. We adopted the same phase ranges as those at S band for the main pulse. For the interpulse phase, we shift the central position 0.015 rotational period earlier than that in S band with a width of 0.06 rotational period following the results of Cordes et al. (2004), who reported that the occurrence phases of GRPs shifts ~ 0.03 period earlier above ~ 4 GHz.

As shown in the time-phase plot of Figure 4.1, the candidates at inappropriate phases, namely pseudo-signals, are not so many. In our selection method, the expected number of the pseudo-signals appearing accidentally at the GRP selection phases becomes at most $\sim 5.2 \pm 2.3$ (at LH band, assuming a Poisson error) during the entire time of the simultaneous observation at all the observatories.

Examples of the pre-dedispersed dynamic spectra and the dedispersed pulse profiles of the GRP are shown in Figures 4.2 and 4.3, respectively. This GRP is plotted as the stars in Figure 4.1, In Figure 4.2, the dispersive delays of the GRP signal expected from equation (4.1) is clearly shown, indicating that this signal is a real GRP. Even in this case, the peak S/N value (7.2 σ) in C band is lower than the GRP selection threshold. However, the synchronized pulse with the light curves in the other bands suggests that the C band signal is a true GRP. As long as a GRP is selected in a certain band, the fluences or their upper-limits are estimated for all the bands. We explain detailed methods of the fluence estimate in the next section.

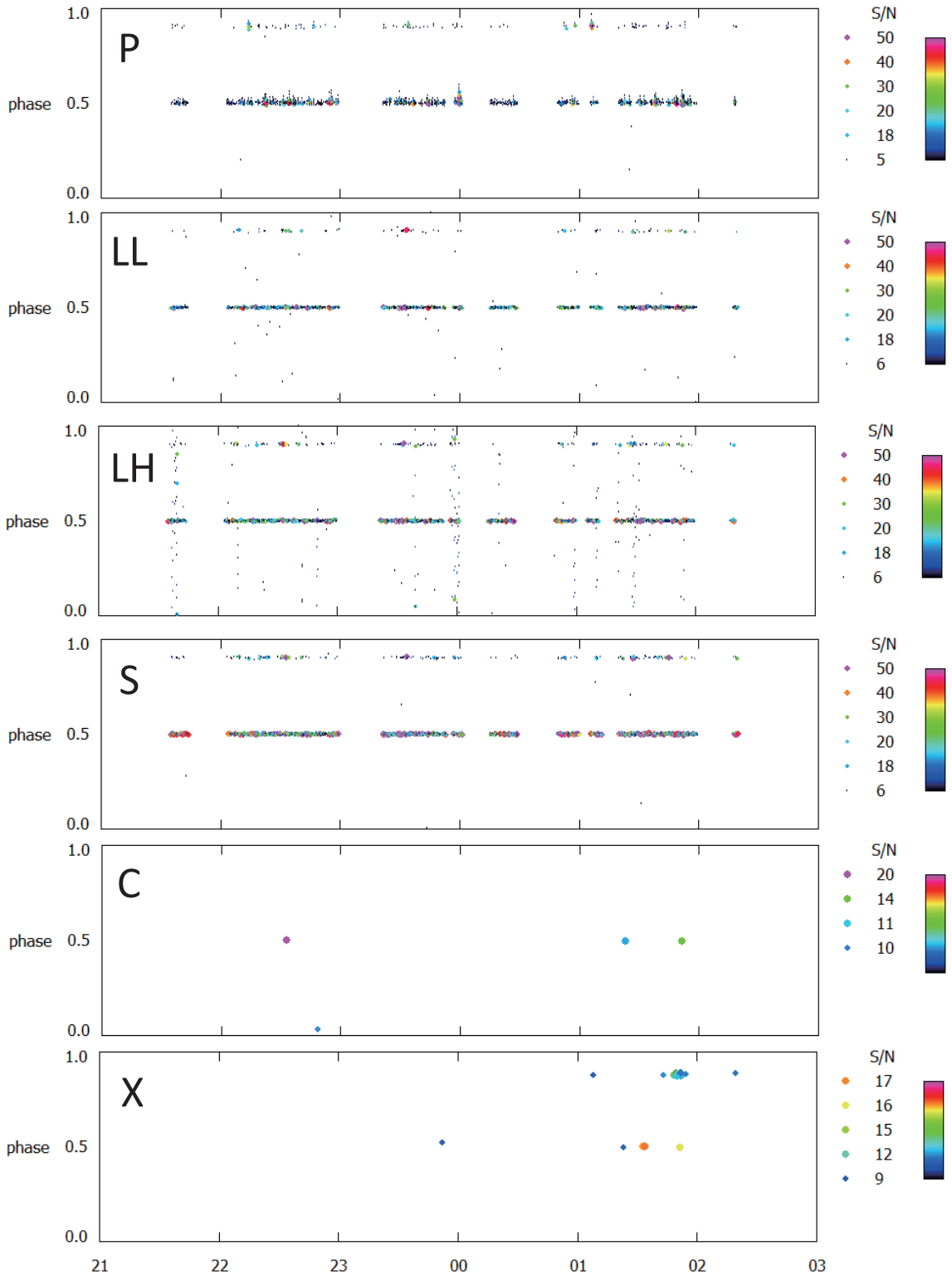

Fig. 4.1.— Scatter plots of phase and time for the GRP candidates from 21^h30^m on 6th September 2014 to 02^h20^m on 7th September 2014 for all the frequency bands. The times at all observatories are converted to Barycentric Dynamical Time at the Solar system barycenter (See section 3.2.1).

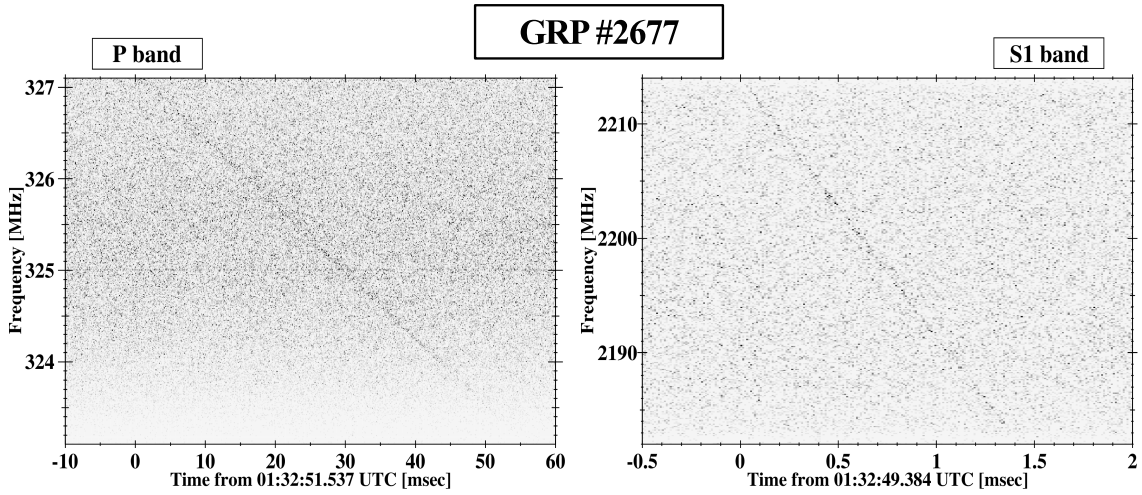

Fig. 4.2.— The dynamic spectra of the GRP #2677.

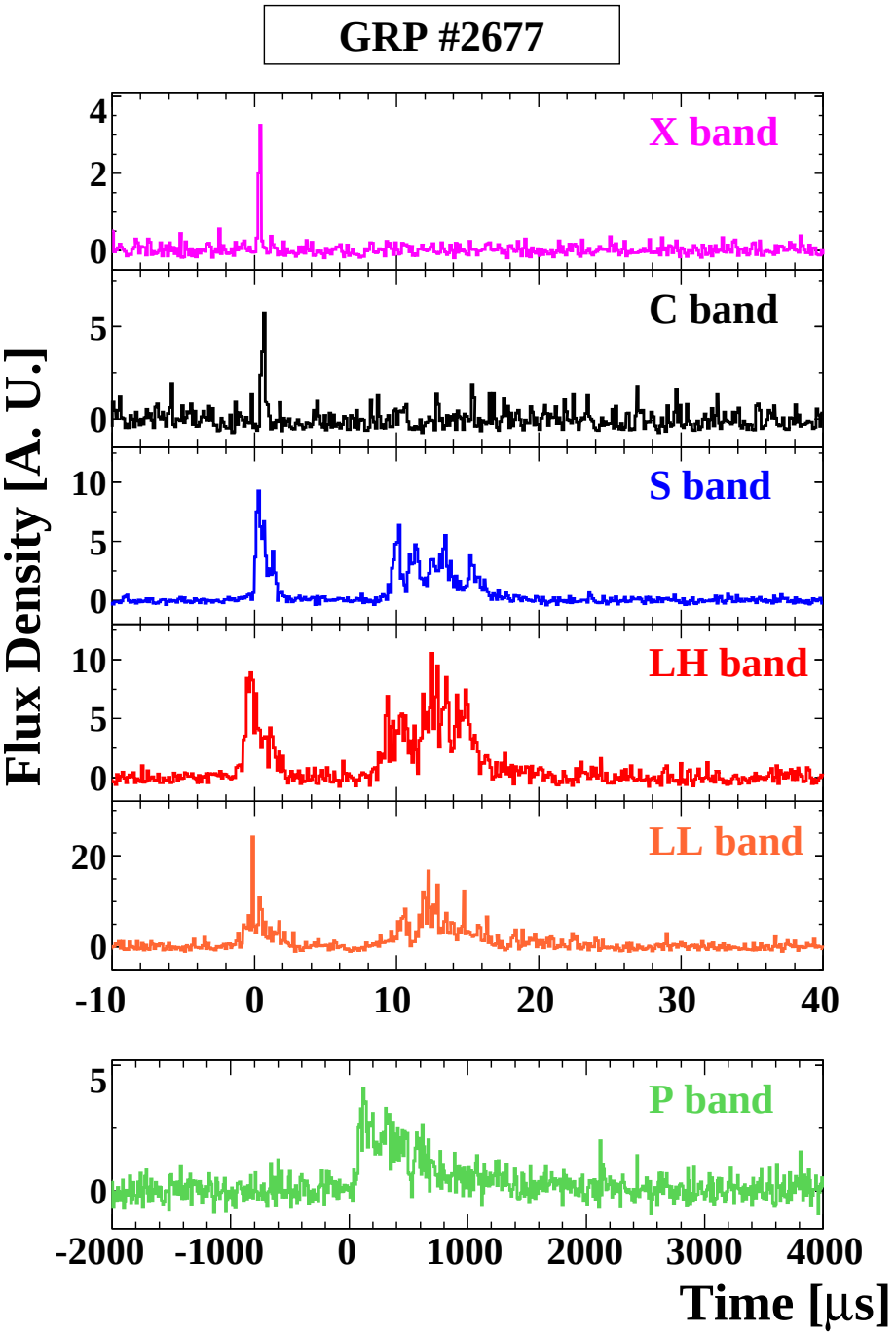

Fig. 4.3.— The dedispersed light curves of the GRP #2677 (same GRP as that shown in Figure 4.2), which is simultaneously detected at all the bands. The curve in P band is smoothed with 10μs time-bin. The other curves are smoothed with 125ns. The spectrum of this GRP is shown in Figure 4.17.

4.2.2 Fluence Estimate

We obtained 3194 GRPs occurring at the main pulse phase (hereafter MPGRPs), and 272 GRPs occurring at the interpulse phase (hereafter IPGRPs) during the effective observation time of 2.9 hours. Hereafter, we focus on the time-integrated flux (fluence) of the GRPs rather than the peak flux, because the scatter broadening of the pulse profile depends on frequency (e.g. Cronyn, 1970). For LL, LH and S bands, we generated time-series of the S/N values with a finer time resolution of 1μs than that used in our GRP selection. Then, the S/N values of all the frequency bands were transformed to the flux density calibrated by reference sources (Cas A, Cyg A etc.). The durations of GRPs distribute widely, but a too long time interval to integrate the flux leads to a too large error in the GRP fluence. Therefore, the time interval to obtain the fluence was individually set for each GRP to contain the entire pulse sufficiently. The details of those methods are summarized in Appendix B. Integrating over this time interval, we estimated the GRP fluence, or upper-limit in each frequency band.

Representing the fluence distribution as $N(F_i) \propto F_i^{\Gamma}$ for the high-fluence portion, the index Γ is obtained for each band as shown in Table 4.3. The detected numbers of the GRPs at C and X bands are too small to estimate the index. The obtained indices Γ at bands from P to S (P–S bands) are consistent with the previous studies (Mickaliger et al., 2012).

Table 4.3. Power-law index Γ for the fluence distribution.

Band	Γ (Sample Number)	
	MPGRP	IPGRP
P	$-2.44^{+0.20}_{-0.24}$ (760)	$-2.73^{+0.55}_{-0.83}$ (101)
LL	$-2.98^{+0.11}_{-0.12}$ (2252)	$-2.88^{+0.37}_{-0.50}$ (182)
LH	$-2.97^{+0.13}_{-0.15}$ (2696)	$-2.75^{+0.72}_{-0.87}$ (210)
S	$-2.68^{+0.11}_{-0.13}$ (2803)	$-3.62^{+0.55}_{-0.70}$ (202)

4.2.3 Single Power-Law Fit

We examined whether the wide band spectra of our samples follow a single power-law (hereafter SPL) or not. The GRP spectra were fitted by the SPL as a function of frequency ν,

$$F(\nu) = F_{0.3} \left(\frac{\nu}{325.1\mathrm{MHz}} \right)^{\alpha}, \tag{4.2}$$

with a normalization parameter $F_{0.3}$ and index α. The goodness-of-fit test was done by means of the modified χ^2 statistic,

$$\begin{aligned} \hat{\chi}^2 &= \sum_{i \in \mathrm{P,LL,LH,S,C,X}} \left(\frac{F_i - F(\nu_i)}{\sigma_i} \right)^2 \\ &- 2 \sum_{j \in \mathrm{P,LL,LH,S,C,X}} \ln \int_{-\infty}^{F_{\mathrm{max},j}} \frac{1}{\sqrt{2\pi\sigma_j^2}} \exp \left[-\frac{1}{2} \left(\frac{F' - F(\nu_j)}{\sigma_j} \right)^2 \right] dF'. \end{aligned} \tag{4.3}$$

to deal with non-detection data points (Avni et al., 1980; Sawicki, 2012). The first sum corresponds to the standard χ^2 statistic for detected data points at a frequency channel i with the fluence F_i and its 1σ error σ_i. The second sum expresses the contribution of non-detection (upper-limit) data points, where $F_{\mathrm{max},j}$ is the 1σ upper-limit of the fluence at the frequency band j. As we describe in Appendix A, the error of the fluence in this analysis consists of the systematic one and the statistical one. Assuming that the systematic error follows a Gaussian distribution in the same manner as the statistical one, the sum of those errors is adopted in the fitting procedure. We also assume that $\hat{\chi}^2$ follows a χ^2 distribution with $n-2$ degrees of freedom for n data points, and set a critical value of $\hat{\chi}^2$ to reject the SPL hypothesis.

For the GRPs whose spectra are consistent with SPLs (hereafter, PL-GRPs), we estimated the confidence intervals or the upper-limits of the fitting parameters as follows. For each pair of the parameters $(F_{0.3}, \alpha)$, we calculate $\hat{\chi}^2$, and express

$$\hat{\chi}^2 = \hat{\chi}^2_{\mathrm{min}} + \Delta\hat{\chi}^2, \tag{4.4}$$

where $\hat{\chi}^2_{\mathrm{min}}$ is the minimum value of $\hat{\chi}^2$. Based on the discussion of Lampton et al. (1976), we assumed that $\Delta\hat{\chi}^2$ follows a chi-square distribution with p degree(s) of freedom, where p is the number of fitting parameters. A 68% confidence interval of each fitting parameter is the interval satisfying

$$\Delta\hat{\chi}^2 = 2.3, \tag{4.5}$$

for $p = 2$ in our case. When we detect a GRP only at P band, the upper-limits at other bands lead to an upper-limit of α. In this case, we set $\hat{\chi}^2_{\mathrm{min}} = 0$. Then, we set the 68% upper-limit of α as the maximum value of α satisfying $\Delta\hat{\chi}^2 = \hat{\chi}^2 = 2.3$.

4.2.4 Detection Category

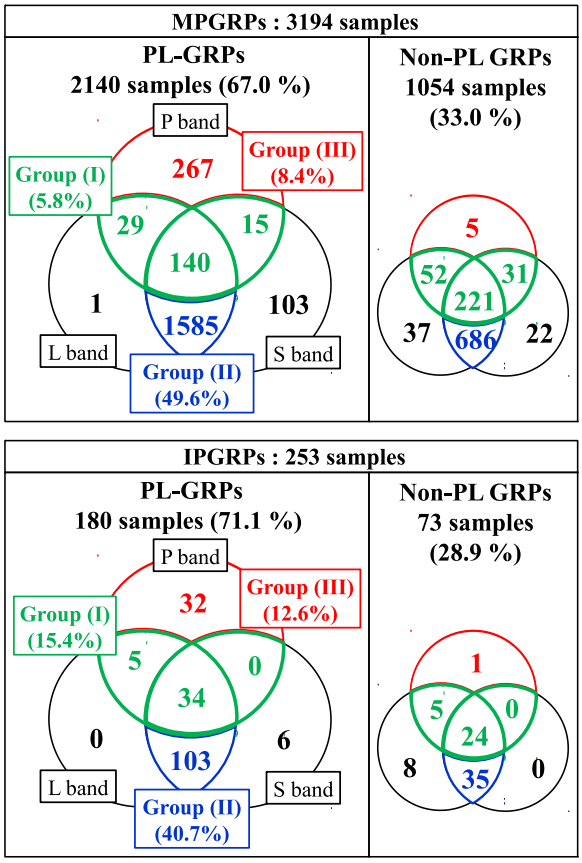

Fig. 4.4.— Categorization of our spectral samples. The numbers of GRPs divided according to the detected bands are shown. The numbers in the regions where circles overlap each other mean the number of GRPs detected at corresponding multiple bands. The GRPs detected at LL band and/or LH band are merged into the category of "L band". See also Tables 4.4 and 4.5.

In Figure 4.4, we categorize our GRPs into the three groups according to the detection/non-detection in the individual bands. The numbers of GRPs are small at C and X bands, we categorize only the GRPs detected at P, L or S band. The GRPs in Group (I) are detected at multiple frequency bands including P band. For Group (I) GRPs, the parameters $F_{0.3}$ and α are determined more precisely than the GRPs in the other groups. An example of the $\hat{\chi}^2$-map of the GRPs in Group (I) is shown in the top panel of Figure 4.5.

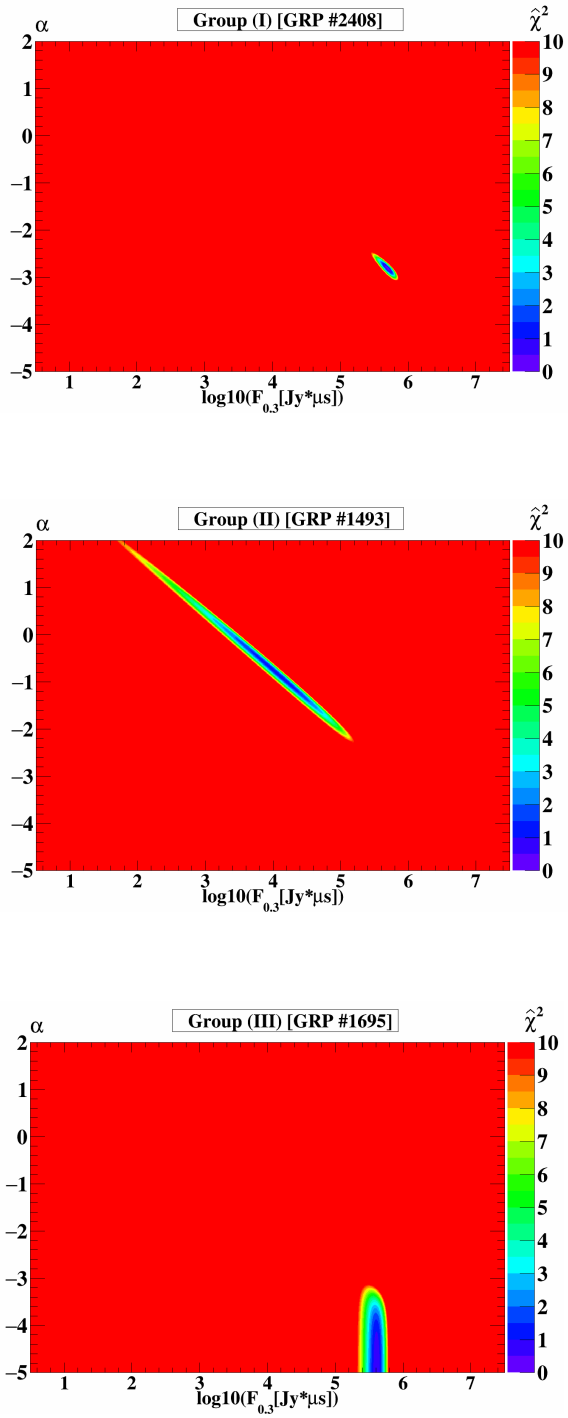

Fig. 4.5.— Behavior of $\hat{\chi}^2$ in the parameter space $(F_{0.3}, \alpha)$ for the typical GRPs in Groups (I)–(III) (see Section 4.2.4).

Group (II) is defined as the GRPs detected at both L and S bands, but not detected (set an upper-limit) at P band. For these GRPs, the P band fluence is estimated by extrapolation using the fluences at L and S bands. For the samples consistent with SPLs in Group (II), of course, the extrapolated value does not conflict with the upper-limit at P band. As shown in the middle panel of Figure 4.5, the typical allowed region in the parameter space for Group (II) GRPs is obliquely elongated. In this case, the spectral index is loosely determined because of the relatively narrow frequency separation between L and S bands.

The GRPs detected at P band, but neither L nor S band, belong to Group (III). For those GRPs, while the fluence at P band, $F_{0.3}$, is precisely determined, the upper-limits at higher frequency bands merely provide an upper-limit on α. The $\hat{\chi}^2$-map in the bottom panel of Figure 4.5 shows the allowed region is vertically elongated.

As will be mentioned below, the fluences at P–S bands (0.3–2.2 GHz) may be less affected by interstellar scintillation so that the fluences in this frequency range are relatively reliable compared to the fluences in higher frequency bands. Therefore, we first discuss the spectra at P–S bands in the next section.

Extrapolating the data in Figure 3 of Rickett & Lyne (1990), the timescales of the refractive interstellar scintillation (RISS) are estimated to be about 12 hours or longer for the frequency range lower than $\sim$ 2 GHz. Therefore, at these frequency bands, the intensity modulation due to the RISS can be almost negligible during our about 5-hour simultaneous observing session. In contrast, the RISS timescales for C and X band observations are estimated to be about one hour so that the pulse flux could be modulated by the RISS during our observing session. Indeed, in the 8.9 GHz observation of the Crab pulsar, Bilous et al. (2011) showed that the numbers of the detected GRPs during 2-hour observing sessions in the same day were quite different. This variation of the detection rate may be due to the RISS rather than the intrinsic variation of the GRP activity. As for the diffractive interstellar scintillation (DISS), in the observation by Cordes et al. (2004), the mean pulse flux density was deeply modulated on timescales as short as 5 minutes at frequencies $\gtrsim$ 3 GHz. To evaluate the effect of the DISS in our case, we compared our bandwidths with the scintillation bandwidths obtained in Cordes et al. (2004). The scintillation bandwidths are < 0.024 MHz, < 0.8 MHz, and 2.3 ± 0.4 MHz, at 0.43, 1.48 and 2.33 GHz, respectively. For our P, L and S bands, they are at least an order of magnitude smaller than our bandwidths of the frequency channels (see Table 4.1). The scintillation modulation is presumed to be averaged out

at those channels [1]. Also, at L and S bands, the synthesis of the multiple channels described in Section 4.2.1 may reduce the effect of the DISS. In contrast, extrapolating the result in Cordes et al. (2004) with $\nu^{4.4}$ scaling (corresponding to the Kolmogorov spectrum for the interstellar electron density fluctuation), the scintillation bandwidths for C and X bands are larger than the observation bandwidths. Therefore, the fluences for our C and X bands may be significantly affected by both the RISS and DISS. We focus on the spectra at P–S bands below.

4.3 GRP Spectra from P to S Bands

Following the method in Section 4.2.3, we fitted the obtained spectra with a SPL function. We limited the parameter ranges from $10^{0.5}$ to $10^{7.5}$Jy μs on the normalization $F_{0.3}$, and from -5.0 to $+2.0$ on the index α. The number of the data points (P, LL, LH, and S bands) results in 2 degrees of freedom (DoF) for χ^2 distribution. We adopted a critical value of $\hat{\chi}^2 = 5.99$ (significance level of 5%) to judge the consistency of the SPL hypothesis. As we mention in Section 4.3.4, spectra with $\alpha > 2$ or < -5 were excluded from the SPL samples even if the $\hat{\chi}^2$-value is small enough. In Figure 4.6, we show some examples of the spectra of the PL-GRPs. For the GRPs detected at P–S bands, the spectral index widely distributes between -1 and -4, while the spectral index of the normal main pulse and interpulse are -3.0 and -4.1, respectively (Moffett & Hankins, 1999). GRP spectra may show wider variety in their indices than those of normal pulses.

The numbers of the GRPs divided according to the consistency of their spectra with SPLs, are summarized in Tables 4.4, and 4.5. In our samples, the fractions of the broadband GRPs, namely GRPs in Group (I), are 15% and 27% for MPGRPs and IPGRPs, respectively. We find that the spectra of 2140 of 3194 MPGRPs (67.0%) and 180 of 253 IPGRPs (71.1%) are consistent with SPLs at a significance level of 5%. The goodness of fit depends on the method of the error estimate. When we impose more conservative errors on the fluences than those in our " standard " analysis, the fraction of the consistent spectra with SPLs becomes more than 95% (see Appendix C).

[1]Note that we obtained some GRPs that show spectral structures in narrow frequency ranges as shown in Appendix C. This may indicate that the DISS effect has not been completely understood yet. Alternatively, the spectral structures may be intrinsic in GRPs.

Table 4.4. The numbers of the MPGRPs.

Detected Band(s)	Group[a]	SPL Hypothesis Consistent ($\hat{\chi}^2_{\rm min} < 5.99$)	SPL Hypothesis Inconsistent ($\hat{\chi}^2_{\rm min} > 5.99$)
P & LL & LH & S	I	117	192
P & LL & LH	I	7	8
P & S	I	15	31
P & LL & S	I	3	3
P & LH & S	I	20	26
P & LL	I	2	25
P & LH	I	20	19
LL & LH & S	II	1230	619 ($\alpha > 2:8$)
LL & S	II	13	7
LH & S	II	342	60 ($\alpha > 2:4$)
LL & LH	···	0	24
S	···	103	22 ($\alpha > 2:22$)
LL	···	0	2
LH	···	1	11
P	III	267	5 ($\alpha < -5:5$)
Total		2140	1054 ($\alpha > 2:34$, $\alpha < -5:5$)

[a]We categorize the GRPs into three groups, from I to III. See Section 4.2.4.

Table 4.5. The number of the IPGRPs.

Detected Band(s)	Group[a]	SPL Hypothesis Consistent ($\hat{\chi}^2_{\rm min} < 5.99$)	SPL Hypothesis Inconsistent ($\hat{\chi}^2_{\rm min} > 5.99$)
P & LL & LH & S	I	31	22
P & LL & LH	I	1	1
P & S	I	0	0
P & LL & S	I	0	0
P & LH & S	I	3	2
P & LL	I	1	1
P & LH	I	3	3 ($\alpha < -5:1$)
LL & LH & S	II	88	34
LL & S	II	0	0
LH & S	II	15	1
LL & LH	···	0	1
S	···	6	0
LL	···	0	2
LH	···	0	5
P	III	32	1 ($\alpha < -5:1$)
Total		180	73 ($\alpha > 2:0$, $\alpha < -5:2$)

[a]We categorize the GRPs into three groups, from I to III. See Section 4.2.4.

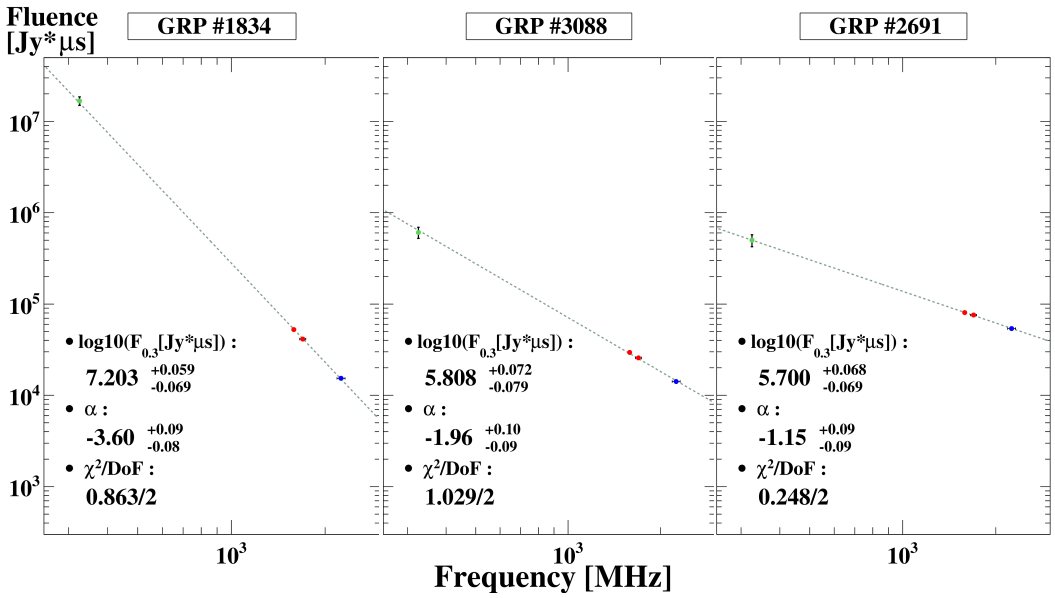

Fig. 4.6.— Examples of the GRP spectra consistent with SPLs. The best-fit power-law functions are plotted with the dotted lines. The obtained parameters with 68% confidence intervals and the minimum $\hat{\chi}^2$ are also shown.

4.3.1 Correlation between the L/S-Band Fluence and Hardness

Our results of the spectral analysis show apparent correlations between the parameters. We choose PL-GRPs in Group (I) (see Tables 4.4 and 4.5, and Section 4.2.4). The uncertainty in the spectral index tends to be small owing to the wide frequency separation between P and L/S bands (see Section 4.2.4).

We show scatter plots of the fluences at LL, LH or S band and the indices α in Figures 4.7 and 4.8 for the MPGRPs and IPGRPs, respectively. In these figures, we also draw the "observation bias" lines indicating the regions where the fluence at P or the corresponding frequency band is below the detection limit. In these figures, there seems to be apparent correlations between the fluences and the indices α. For those GRPs, we calculate the Spearman rank correlation coefficient, R (e.g. Press et al., 1992). From the values of R, we reject the hypothesis that those the fluences and the indices are unrelated at $\sim 10\sigma$, $\sim 13\sigma$ and $\sim 13\sigma$ level at LL, LH and S band, respectively. These values of R are merely reference ones. GRPs in the upper-left region have harder and dimmer spectra, and may be hard to be detected at P band. Therefore, the deficit of samples in the upper-left region can be due to the selection bias. However, the deficit in the lower-right region cannot be explained by the selection bias. Those results rule

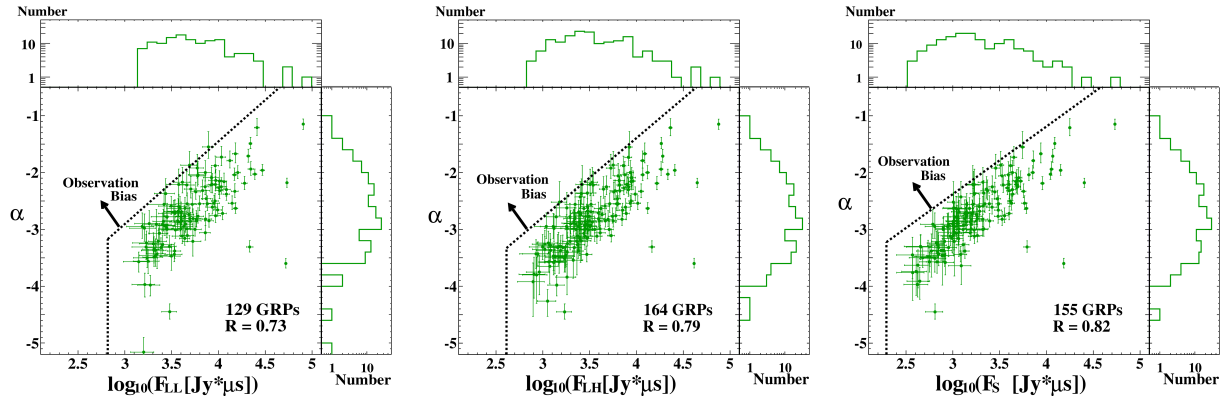

Fig. 4.7.— Scatter plots of the observed fluences at LL (left), LH (middle) and S (right) bands and the spectral indices α for MPGRPs belonging to Group (I). The distributions of the fluences and indices are projected on the upper and left sides of each panel. On the upper-right panel of each figure, the Spearman rank correlation coefficient R (e.g. Press et al., 1992) is shown.

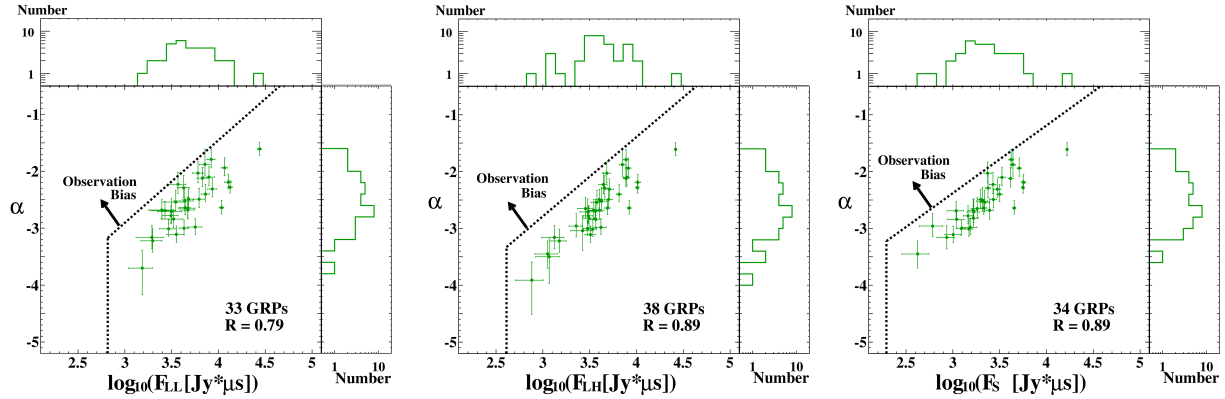

Fig. 4.8.— Same as Figure 4.7 but for IPGRPs.

out at least an uniform distribution of α between ~ -4 and ~ -1. An alternative interpretation is that the typical spectral index is ~ -1 or harder. In such cases, a small fraction of GRPs in the tail of the α-distribution is seen beyond the detection limit in our plots. This may result in the apparent correlations. Adding the GRPs in Group (II) for the correlation analysis, we did not find a significant correlation. This may be partially due to the large errors in the index of Group (II) GRPs. Alternatively, another type of GRPs whose spectra are not SPLs may be contaminated in Group (II) samples.

4.3.2 Correlation between the P-Band Fluence and Hardness

Subsequently, we investigated the correlation between the P-band fluence and hardness. We show the scatter plots of the GRP fluences at P band and the spectral indices α in the central panel of Figures 4.9 and 4.10 for the MPGRPs and IPGRPs, respectively. We also show the histograms of the spectral indices sorted by $F_{\rm P}$ or $F_{0.3}$ in Figures 4.11 and 4.12. The mean spectral indices of them in Table 4.6. In figures 4.9 and 4.10, we plot the observed fluences $F_{\rm P}$ for Groups (I) and (III), while the values $F_{0.3}$ estimated from Equation 4.2 are plotted for Group (II). With the 68% confidence interval, the errors in the figures are plotted in the standard manner for Group (I), but the confidence region ellipses (Press et al., 1992) are directly drawn for Group (II). This is because the allowed regions for Group (II) are inclined and elongated, as shown in the middle panel of Figure 4.5, reflecting the fact that the value of $F_{0.3}$ estimated from extrapolation largely depends on α. For Group (III), we plot the upper-limits on α with the observed $F_{\rm P}$. We also draw the "observation bias" lines similar to Figures 4.7 and 4.8.

If we extract only the samples in Group (I) (green points), whose parameters are determined most accurately, the values of the Spearman rank correlation coefficients R are -0.41 for the MPGRPs and -0.37 for the IPGRPs. From the values of R, the hypothesis that those two variables are unrelated is rejected at $\sim 5.9\sigma$ level for MPGRPs, and at $\sim 2.7\sigma$ level for IPGRPs. As we mentioned in the previous section, since R is evaluated without considering error bars, obtained significance levels are only reference ones. Contrary to L/S bands, a negative correlation between the fluence and spectral hardness is found at P band although it is less significant than that at L/S bands.

In the scatter plots of Figures 4.9 and 4.10, dimmer and softer GRPs are not found in the lower-left region. Such GRPs are expected to be very dim also at L/S bands so that the deficit of GRPs in that region can be due to the observation bias. On the other hand, the brighter and harder (the upper-right region) GRPs are expected to be easily detected at L/S band as long as the spectrum extends. It is also seen from those scatter plots that whereas the samples in Group (II) imply an existence of a significant number of hard GRPs ($\alpha \gtrsim -1$), there are not so much hard GRPs in Group (I). Note that the existence of such dim–hard GRPs may be not so convincing because the fluences of Group (II) GRPs at P band are extrapolated ones. In order to obtain such dim–hard GRPs, we make a stacking analysis in the next section.

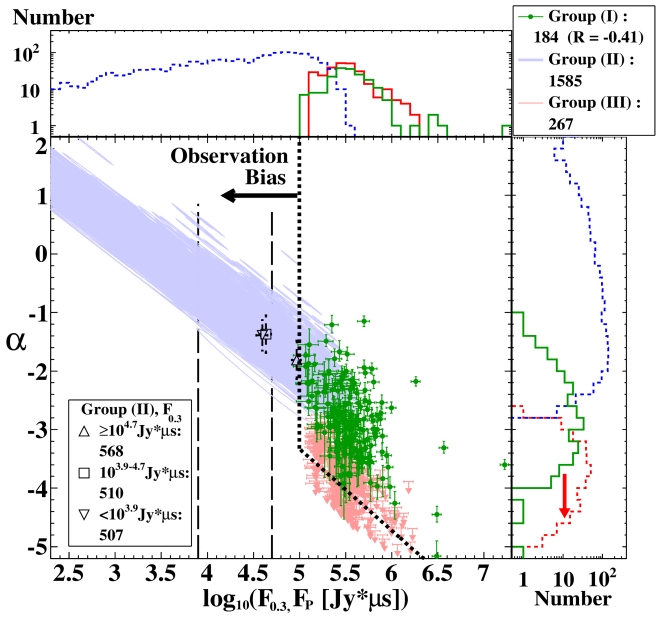

Fig. 4.9.— Scatter plot of the observed/extrapolated P-band fluences and the spectral indices α for the MPGRPs whose spectra are consistent with SPLs. The data for Groups (I), (II), and (III) are shown with green, blue, and red symbols, respectively. The upper-left and the lower-right panels are the number distributions for the parameters of their axes, where we put samples into a bin neglecting the errors. Note that the histogram of Group (III) for α consists of the upper-limit values. On the upper-right panel, the Spearman rank correlation coefficient R is shown for Group (I). Based on the vertical dashed lines in the central panel, we further divide the samples in Group (II) into sub-groups. The average values of $F_{\rm P}$ and α ($\bar{F}_{\rm stack}$ and $\bar{\alpha}_{\rm est}$) obtained with the stacking analysis for each sub-group are plotted with the triangles and the square (see Section 4.3.2 and Table 4.7).

4.3.3 Stacking Analysis of the GRPs in Group (II)

We collect the light curves at P band in the rotational periods when Group (II) GRPs occurred. Then, we divide those light curves into a few sub-groups according to the values of $F_{0.3}$, and superpose the light curves in each sub-group. The obtained average pulse profiles are shown with the colored lines in Figures 4.13 and 4.14 for the MPGRPs and the IPGRPs, respectively. Compared to the average pulse profile of the off-GRP periods, it is clearly seen that the pulse at P band is on average enhanced at the GRP period defined with L/S bands. The average fluences $\bar{F}_{\rm stack}$ and $\bar{F}_{\rm Off-GRP}$ for on- and off-GRP periods, respectively, are evaluated for phase intervals shown with arrows in

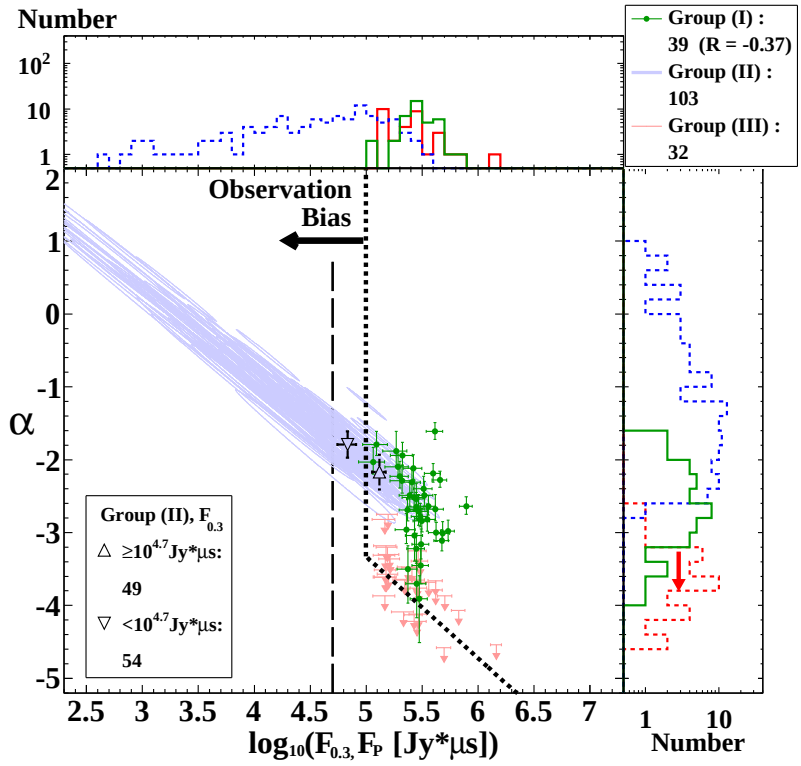

Fig. 4.10.— The same plot as Figure 4.9, but for the IPGRPs.

Figures 4.13 and 4.14. The width of the intervals is 0.11 period, which is the sum of the width for the GRP selection (0.05 period) and the characteristic duration of the GRPs at P band ($\sim$ 2ms, 0.06 period). The calculated values of $\bar{F}_{\rm stack}$ and $\bar{F}_{\rm Off-GRP}$ are summarized in Table 4.7. From $\bar{F}_{\rm stack}$ and the fluence $F_{\rm S}$ of each GRP at S band, we deduce a spectral index $\bar{\alpha}_{\rm est}$ as

$$\bar{\alpha}_{\rm est} \equiv \frac{1}{N_{\rm GRP}} \sum_{i}^{N_{\rm GRP}} \frac{\log\left(\bar{F}_{\rm stack}/F_{\rm S,i}\right)}{\log\left(325.1{\rm MHz}/2250{\rm MHz}\right)} \tag{4.6}$$

. The mean values of $\alpha_{\rm est}$ are tabulated in Table 4.7, and $(\bar{F}_{\rm stack}, \bar{\alpha}_{\rm est})$ are plotted in Figures 4.9 and 4.10 as the open black points.

If all the spectra in each sub-group are followed by SPL, $\bar{F}_{\rm stack}$ is expected to be within the range predicted by $F_{0.3}$. For the sub-groups of the GRPs with larger $F_{0.3}$, especially for $F_{0.3} \geq 10^{4.7}$Jy μs (mean fluence of the "normal" pulse, including MP, IP and also the precursor components), the values of $\bar{F}_{\rm stack}$ are $\sim 10^{4.97}$Jy μs for the MPGRPs, and $\sim 10^{5.12}$Jy μs for the IPGRPs, consistent with the range of $F_{0.3}$. However, for the sub-groups of the MPGRPs with $F_{0.3} < 10^{3.9}$Jy μs and the IPGRPs with $F_{0.3} < 10^{4.7}$Jy μs, the values of $\bar{F}_{\rm stack}$ are $\sim 10^{4.58}$Jy μs for the MPGRPs, and $\sim 10^{4.83}$Jy μs for the IPGRPs, which are inconsistent with the range of $F_{0.3}$, Since we

Table 4.6. Mean spectral index α sorted by $F_{\rm P}$ or $F_{0.3}$.

GRP fluences at P band	Group	α	
		MPGRP	IPGRP
$\geq 10^{6.0}$ Jy μs	I	-3.54 ± 0.85	···
	II	···	···
	III	< -3.89	< -4.54
$10^{5.5} - 10^{6.0}$ Jy μs	I	-2.98 ± 0.53	-2.61 ± 0.40
	II	-2.59	-2.61
	III	< -3.21	< -3.66
$< 10^{5.5}$ Jy μs	I	-2.65 ± 0.56	-2.68 ± 0.57
	II	-0.91 ± 0.98	-1.38 ± 0.82
	III	< -2.75	< -2.75
ALL	I	-2.85 ± 0.59	-2.65 ± 0.52
	II	-0.91 ± 0.98	-1.39 ± 0.82
	III	< -2.75	< -2.75

Table 4.7. The mean fluences $\bar{F}_{\rm stack}$, $\bar{F}_{\rm Off-GRP}$ and spectral indices $\bar{\alpha}_{\rm est}$

	MPGRP			IPGRP	
$\log_{10} F_{0.3}$[Jy μs]	≥ 4.7	$3.9 - 4.7$	< 3.9	≥ 4.7	< 4.7
$N_{\rm GRP}$[a]	568	510	507	49	54
$\bar{F}_{\rm stack}[10^4$Jy μs]	9.32 ± 1.05	4.33 ± 0.58	3.94 ± 0.55	13.11 ± 1.80	6.81 ± 1.29
$\bar{F}_{\rm Off-GRP}[10^4$Jy μs]		1.92 ± 0.21		0.96 ± 0.10	
$\bar{\alpha}_{\rm est}$	-1.81 ± 0.33	-1.37 ± 0.32	-1.39 ± 0.26	-2.17 ± 0.24	-1.79 ± 0.18

[a]Number of GRP samples.

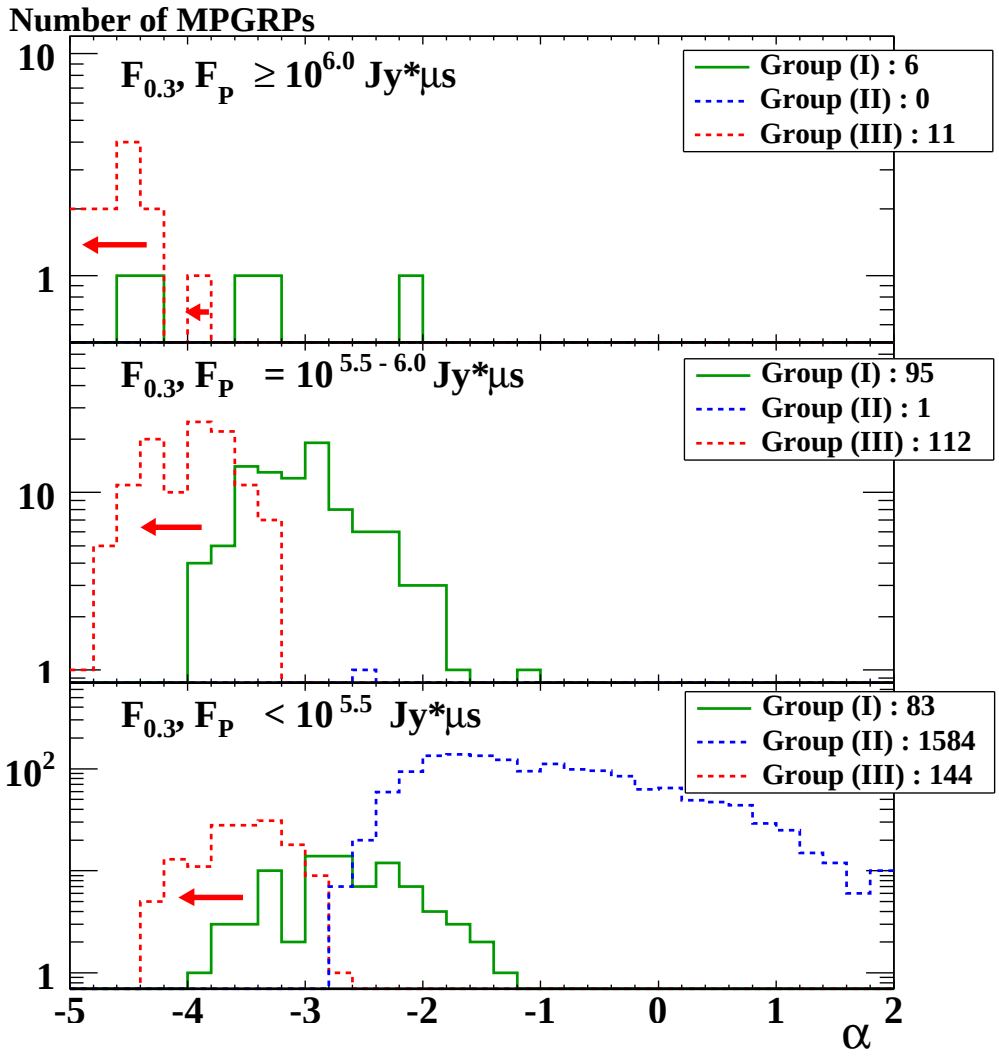

Fig. 4.11.— Histograms of the spectral index α for the MPGRPs. Each panel is divided according to the fluence at P band: $(F_{0.3}, F_{\rm P}) \geq 10^6$Jy μs (top), $10^{5.5}$Jy μs $\leq (\rm F_{0.3}, F_P) < 10^6$Jy μs (middle), and $(F_{0.3}, F_{\rm P}) < 10^{5.5}$Jy μs (bottom). The errors in α are neglected, and the histogram of Group (III) corresponds to the upper-limit values.

have assumed that the normal pulse is absent at the GRP periods, we have not subtracted the contribution of the normal pulse. For such low-fluence GRPs, the method to distinguish GRPs from the normal pulses is not established so far. Here we avoid to conclude the fluences at P band for such GRPs.

4.3.4 Inconsistent Spectra with SPLs

The non-PL GRPs include 1) the GRPs whose spectra are inconsistent with SPLs at a significance level of 5%, and 2) the "ultra-soft/hard" GRPs whose spectral indices are lower than -5 and higher than $+2$, respectively.

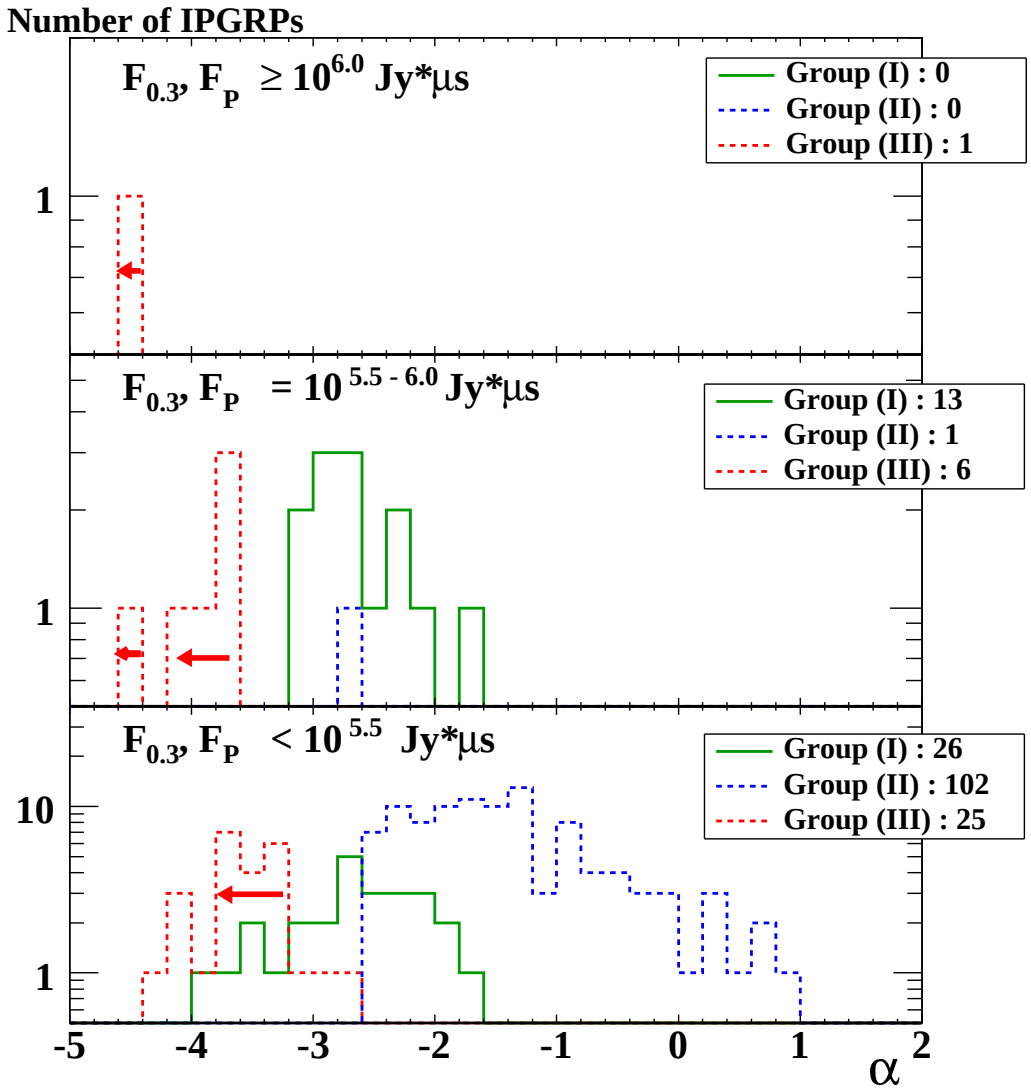

Fig. 4.12.— The same plot as Figure 4.11, but for the IPGRPs.

The fractions of the GRPs judged to be inconsistent with SPLs at a significance level of 5% are 33.0% and 28.9% for the MPGRPs and the IPGRPs, respectively. When the significance level is set to 0.1% ($\hat{\chi}^2 < 13.82$), the fractions are 15.9% and 15.8% for the MPGRPs and the IPGRPs, respectively. Examples of the spectra apparently inconsistent with SPLs are shown in Figure 4.15. Some spectra show softening (hardening) at higher frequencies. Such hard-to-soft (left), soft-to-hard (center), and other (right) examples are displayed in Figure 4.15. Popov et al. (2008, 2009) claimed that GRP spectra tend to show soft-to-hard behavior at 0.6 - 2.2 GHz. In order to examine this tendency, we choose 192 MPGRPs and 22 IPGRPs that are detected at all the bands from P to S, and are inconsistent with SPL spectra at a significance level of 5%. In those MPGRP samples, the fractions of hard-to-soft, soft-to-hard, and irregular spectra

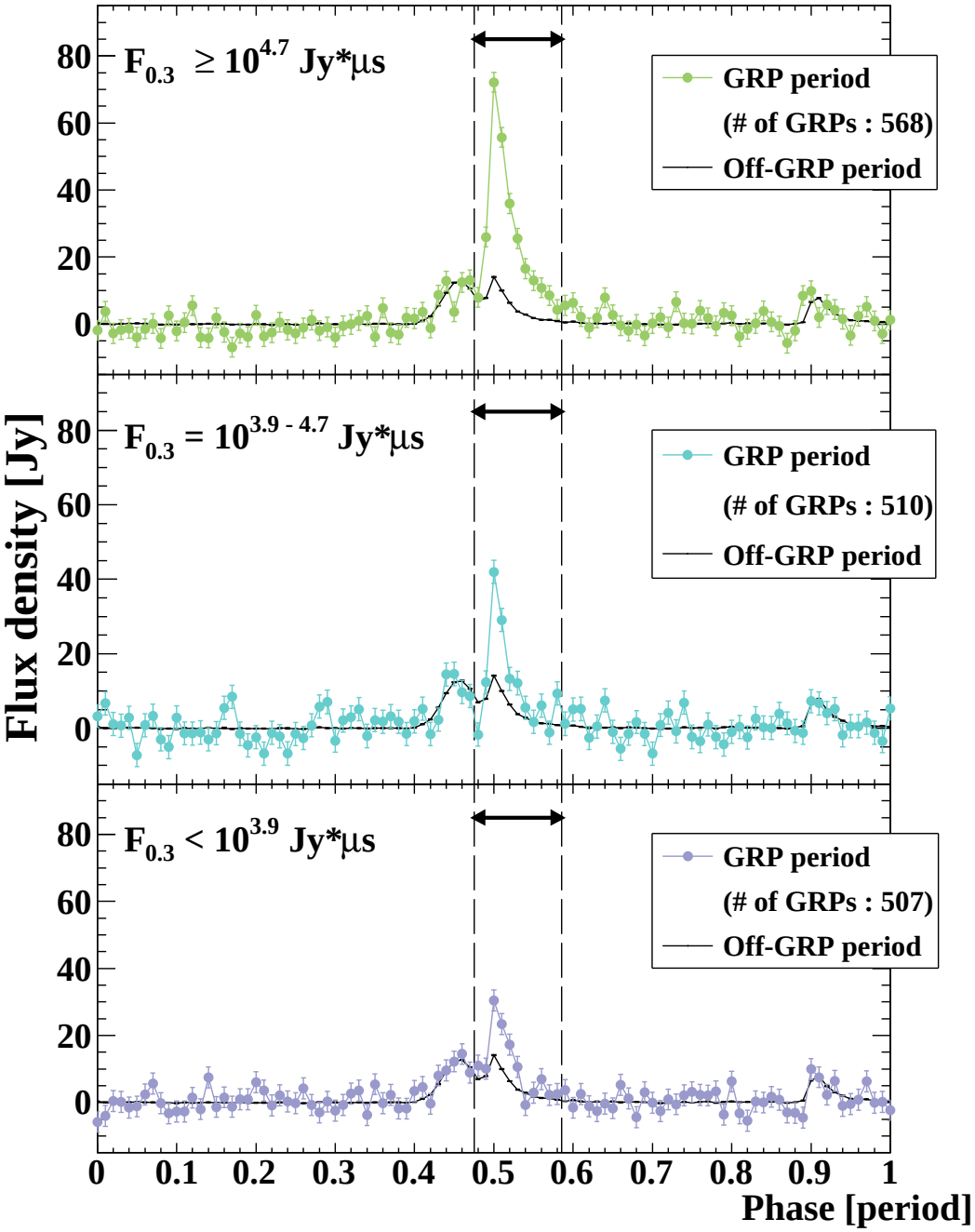

Fig. 4.13.— The average pulse profiles at P band when Group (II) MPGRPs occurred. The samples are divided into three sub-groups according to the fluence $F_{0.3}$. We also show the average profile for the off-GRP periods. The 1σ statistical errors are shown with the error bars. The phase intervals to estimate the fluence are shown by the arrows.

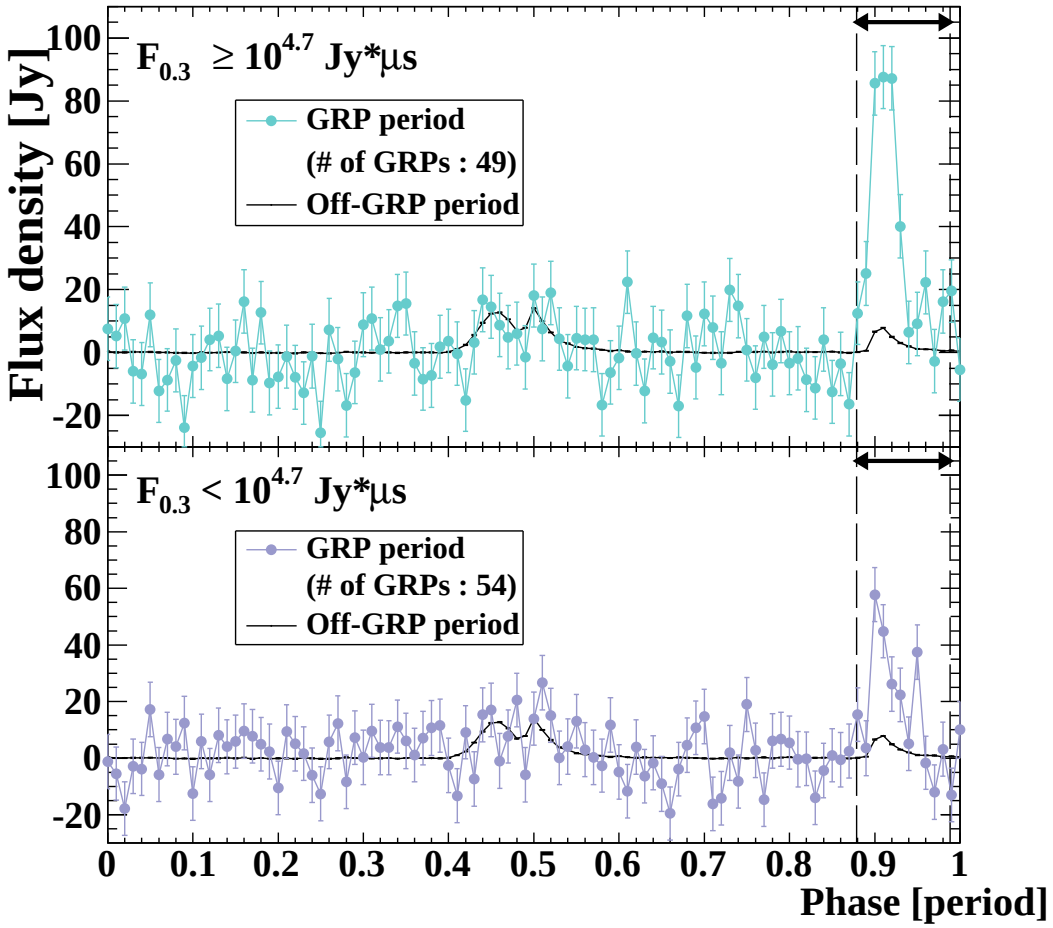

Fig. 4.14.— The same as Figure 4.13, but for the IPGRPs.

are 49 (26%), 81 (42%), and 62 (32%), respectively. For the 22 IPGRPs, the numbers are 3 (14%), 5 (23%), and 14 (64%), respectively. We do not find a clear tendency in the spectral behavior.

We find 5 (0.2%) ultra-soft and 34 (1.1%) ultra-hard MPGRPs, and we also find 2 (0.8%) ultra-soft IPGRPs. In our GRP samples, no ultra-hard IPGRP is found.

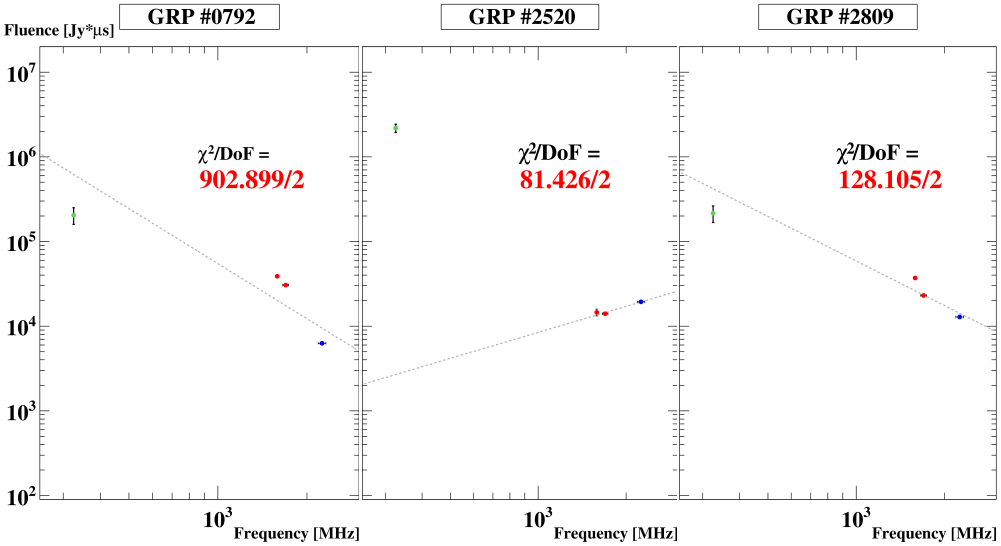

Fig. 4.15.— Examples of the GRP spectra inconsistent with SPLs: hard-to-soft (left), soft-to-hard (middle), and other (right) spectra. The minimum $\hat{\chi}^2$ values and corresponding SPL functions (dotted lines) are shown.

Examples of the spectra for such ultra-soft or ultra-hard GRPs are shown in Figure 4.16.

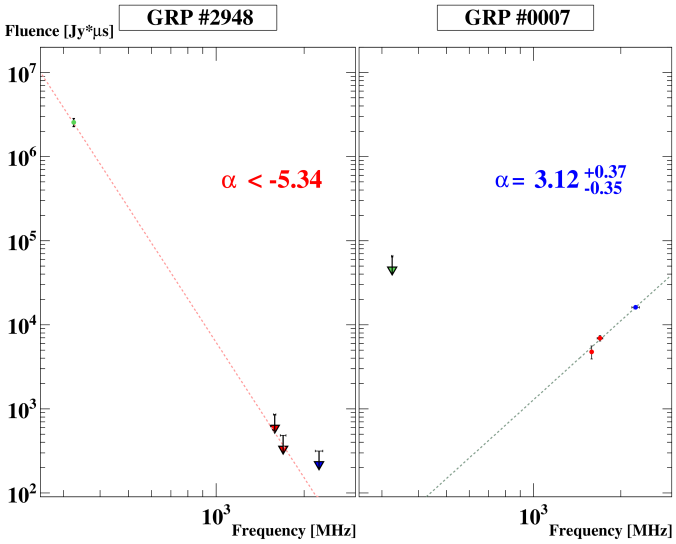

Fig. 4.16.— Examples of the spectra of the "ultra-soft" (left) and the "ultra-hard" (right) GRPs. For the ultra-soft GRP, the SPL function with the 68% confidence upper-limit of α is plotted with the dotted line. Also for the ultra-hard GRP, the best-fit SPL function is plotted.

4.4 GRPs Detected at C/X Band

In this section, we discuss the GRPs detected at C and/or X band(s). Note that the fluences at C and X bands are expected to be affected by intensity modulation due to the interstellar scintillation.

We found 5 MPGRPs and 19 IPGRPs exceeding the selection thresholds (see Section 4.2.1 and Table 4.1) at C and/or X band(s). All of these 5 MPGRPs were simultaneously detected at some of the frequency bands of P, L or S band. In contrast, all the 19 IPGRPs were detected only at X band. As for the IPGRPs in Groups (I) and (II) discussed in Section 4.3, the spectra may have a cut-off below the X band frequency.

In Figure 4.17, we show the spectrum of the MPGRP #2677, whose pulse profiles and dynamic spectra are shown in Figures 4.2 and 4.3, respectively. The spectrum is consistent with a SPL at P–X bands at a significance level of 5%. This is only the case consistent with a SPL in the 5 MPGRPs.

As seen in Figure 4.17, the light curve shows two distinct components. For such bright GRPs, we can easily identify the distinct components, but it is difficult to resolve components for weaker GRPs. Therefore in the previous sections, we have discussed only the fluence spectra integrated over the whole duration of each GRP. Here, we attempt to obtain the temporally divided spectra. When we divide the light curve into two intervals A and B as shown in Figure 4.17, it turns out that the spectrum for the interval B needs a high-frequency cut-off. In Figure 4.3, many finer (sub-μs) structures (e.g. Hankins et al., 2003) are found in the light curve. Therefore, the spectrum may consist of further more components as well.

The spectra of the other four MPGRPs are inconsistent with SPLs as shown in Figure 4.18. The P band fluence of GRP #3012 is about three orders of magnitude brighter than fluences at the higher frequency bands. The spectrum seems to consist of two or more different components, which may be supported by the slight misalignment of the peak times (~ 4 μs) between S and C/X bands. Taking into account uncertainty of the TOA between LL and X band (~ 1.5 μs), the $\sim 4\mu$s misalignment may be intrinsic. The pulse profile of GRP #0703 appears to have multiple components (especially at L and S bands), similarly to the GRP #2677 (Figure 4.17). The stringent upper-limit at X band may require a sharp high-frequency cut-off in the spectrum. For GRP #0703, the temporally divided spectra are also inconsistent with SPLs and need low/high frequency breaks or cut-offs.

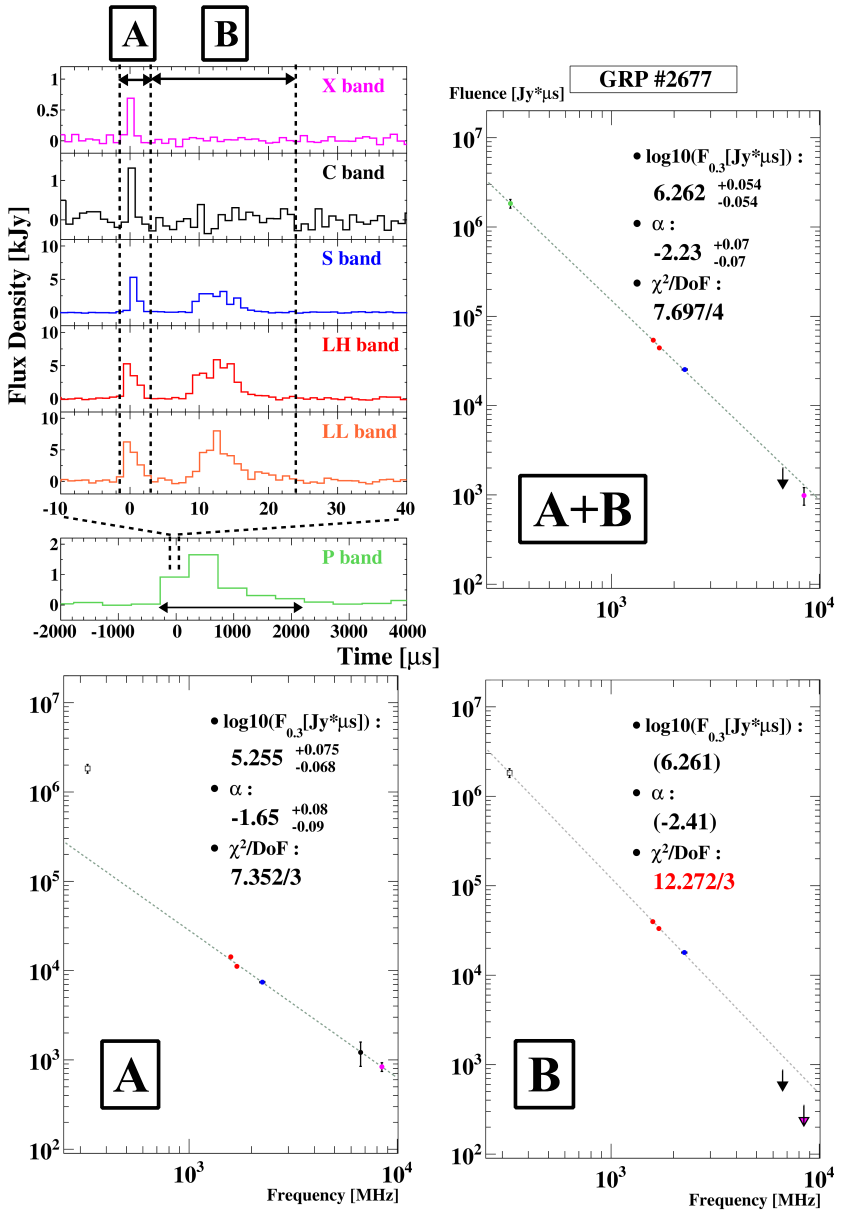

Fig. 4.17.— The spectra of the GRP (upper-right), whose dynamic spectra and pulse profiles are shown in Figures 4.2 and 4.3. The spectra for time intervals A and B defined in the upper-left light curve are shown in the bottom panels. In the fitting of the spectra for time intervals A and B, the data point at P band is neglected.

4.5 Discussion and Conclusion

The broadband (0.3, 1.6, 2.2, 6.7 and 8.4 GHz) simultaneous observation of the GRPs from the Crab pulsar was conducted with four Japanese observatories, Iitate, Kashima, Usuda, and Takahagi, on September 6-7th, 2014. We obtained 3194 MPGRPs and five

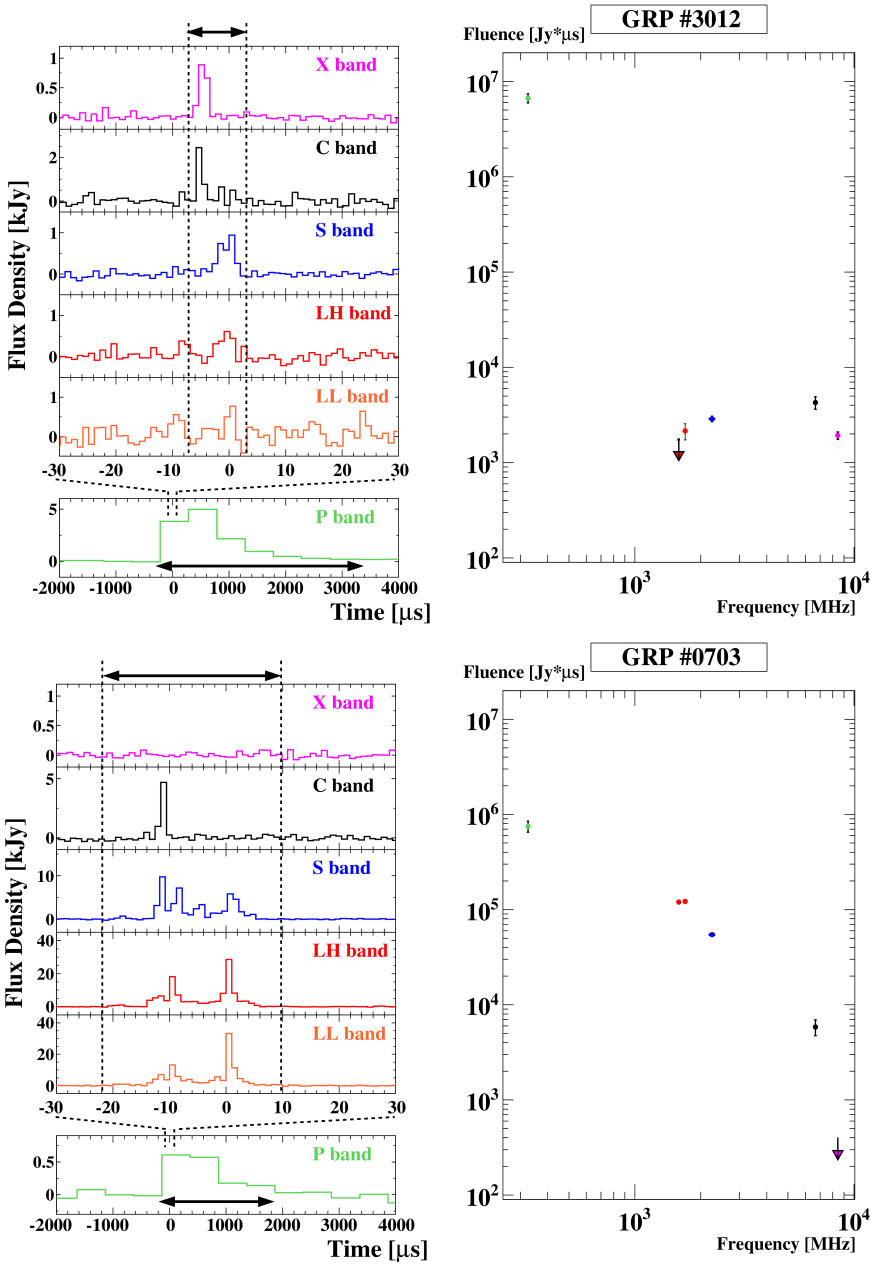

Fig. 4.18.— Examples of broadband GRP spectra (right) inconsistent with SPLs. The pulse profiles (left) are also shown with the time intervals for flux integration.

of them were detected at the multiple frequency bands including 6.7 and/or 8.4 GHz. We also obtained 272 IPGRPs and 19 of them were detected only at 8.4 GHz. We investigated the spectra of those GRPs. Our results are as follows:

- In the frequency range at P, L and S bands (0.3–2.2 GHz), about 70% of the spectra in our GRPs are consistent with single power-laws.

- For the GRPs which are detected at all the frequency bands of 0.3–2.2 GHz and whose spectra are consistent with SPLs, the spectral index is widely distributed from ~ -4 to ~ -1.

- There are apparent positive correlations between the fluence at L/S bands and the spectral hardness. Conversely at P band, an apparent negative correlation between the fluence and the spectral hardness is indicated. Those results rule out at least an uniform distribution of α. Alternatively, the typical spectral index may be ~ -1 or harder.

- For the L/S band GRPs which are not detected at P band, we carry out the stacking analysis of the P band light curve. We find significant enhancement in the P band light curves compared to the light curves in the non-GRP periods. This indicates dim P-band GRPs correlated with the L/S-band(s) GRPs. The average spectral index for such dim samples at P band is harder than the bright GRPs. Since the dim and hard GRPs (Group (II)) occupy about a half of our GRP samples, it might be suggested that most of GRPs may have intrinsically harder spectra than that suggested in the previous studies. This is consistent with the apparent correlations between L/S band(s) fluences and spectral hardness we found.

- We find several ultra-soft ($\alpha < -5$) and ultra-hard ($\alpha > 2$) GRPs.

- A small fraction of spectra apparently deviate from SPLs. We do not find any tendency in the spectral shape for such GRPs.

- Those features or trends mentioned above are seen in not only MPGRPs but also IPGRPs.

4.5.1 Comparison with the previous studies

Karuppusamy et al. (2010) reported that the distribution of the spectral index is extremely wide (from about -15 to $+10$) for a narrow frequency range of 1.3–1.45 GHz. In our observation, the fluences at the 4 channels in L band significantly fluctuate (see Appendix C). If we fit such data with a SPL, a similar result to Karuppusamy et al. (2010) may be obtained. Such fluctuation might be intrinsic, or due to the scintillation modulation. It should be noticed that a large fraction of our broad band spectra do not

conflict with SPLs from P to S bands. Our broadband analysis seems more convincing than the results based on the narrow frequency range.

Sallmen et al. (1999) investigated the spectral index between 0.6 and 1.4 GHz, and obtained their distribution ranging from -4.9 to -2.2. Although the frequency range is slightly different, the index for Group (I) is distributed within a similar range (see Figures 4.11 and 4.12). Oronsaye et al. (2015) investigated the spectral index between 0.2 and 1.4 GHz, and obtained their distribution ranging from -4.9 to -3.6. However, fluences at 1.4 GHz which they estimated are about 2 order of magnitude smaller than those of (e.g. Sallmen et al., 1999; Bhat et al., 2008). Our estimated fluences at L band are roughly consistent with (e.g. Sallmen et al., 1999; Bhat et al., 2008), the fluences Oronsaye et al. (2015) estimated are something wrong.

4.5.2 Emission Mechanism

The emission mechanism for the broadband GRPs may be different from the anomalous cyclotron resonance model (Lyutikov, 2007) proposed for the characteristic property of the IPGRPs above 4 GHz (Eilek & Hankins, 2007), for which we did not detect the signal of the counterpart at P–S bands. In the induced scattering model (Petrova, 2004), the intensity variation is attributed to the fluctuation of the optical depth to the induced scattering. Petrova (2004) suggested that the intensity amplification for the Crab GRPs is more efficient at the lower frequencies, which agrees with the correlation we found. Alternatively, a larger energy release may enhance the efficiency of the electron–positron pair production. The resultant high density pairs may screen out the electric field relatively soon, which may reduce the fraction of higher energy electrons/positrons. Considering the unstable behaviour of the magnetosphere as demonstrated by Timokhin & Arons (2013), the above simple interpretation can be an option to explain the correlation. In any case, before jumping to a conclusion, we need to examine various non-linear processes in the GRP activity such as the detailed properties of the charge bunching due to two stream instability (Cheng & Ruderman, 1980) and the photon softening due to the induced Compton scattering (e.g. Tanaka, Asano & Terasawa, 2015).

4.5.3 Future Prospects

The dim and hard GRPs in Group (II) implies a negative correlation between the fluence at P band and the hardness. Taking into account the results in the previous subsection,

our results suggest that the fluences at P band and L/S bands have an anti-correlation. Since the most of the GRP energy is released at P band or lower frequencies, the anti-correlation means that brighter GRPs tend to show softer spectra. The correlation between the fluence and the hardness seen at P band is weaker than that at L/S bands. This may be because the variation of the fluence at P band is relatively smaller than that at L/S bands, as seen in Figure 4.9, 4.10 or 4.7. Furthermore, the contribution of the normal pulse may disturb the correlation at P band. More observational studies will be required to confirm the correlation we found. The correlation seen at P band is weaker than that for L/S bands. Considering the possible anti-correlation between the P band fluence and the L/S band fluences, there may exist a pivot frequency between P and L bands. In the pivot frequency, the fluence variation may be smaller than those in this paper. Simultaneous observations at a frequency between P and L (for example, ~ 0.7 GHz), and other frequencies may verify the correlation we found.

As for PSR B1133+16, each single pulse, not GRP, can be detected. Kramer et al. (2003) claimed that only the pulse at 4850 MHz showed a large fluence fluctuation, while the fluences in other frequencies (341, 626, 1412 MHz) distributed below a few times the mean value. For the "GRP-like" pulses at 4.85 GHz, Kramer et al. (2003) found the correlation between the flux density at 4850 MHz and the spectral index for 341 MHz–4850 MHz. However, no significant correlation was found for the fluences at 341, 626, and 1412 MHz. Also in this case, most of energies are emitted at lower frequencies. Thus, the correlation we found is qualitatively different from that in Kramer et al. (2003). Studies based on more spectra of GRPs or normal pulses for other pulsars are desired to compare with the results for the Crab GRPs. Since single pulses in a narrow band tend to be affected by the intensity modulation due to the interstellar scintillation, ultra-wideband observations with the next generation telescopes, such as SKA, will be promising for such studies.

Chapter 5

Hard X-ray Observations at the time of Giant Radio Pulses from the Crab Pulsar

5.1 Introduction to this work

As mentioned in the previous section, some coherent process should be concerned with the mechanism of the radio emission from pulsars, while the non-coherency is the dominant nature of the emission process of higher energy (optical, X-ray or γ-ray) pulses. Thus, it was thought that GRPs are not necessarily accompanied with enhancement of photons at higher energy.

However, for optical pulses from the Crab pulsar, there is a statistically significant brightening coincident with GRPs ($\sim$ 3%) over those accompanying with normal radio pulses (Shearer et al., 2003; Strader et al., 2013, see Figure 5.1). Furthermore, in the emission mechanism of GRPs proposed by Lyutikov (2007, see also Chapter 2), enhanced GeV-γ ray emission accompanied by GRPs was predicted. The existence of correlation, if proved, would provide useful information to elucidate the enigmatic mechanisms of emission as well as those of particle acceleration in the pulsar magnetosphere.

Some correlation studies have been carried out in the energy bands other than the optical band. In Table 5.1, we summarize the correlation studies which have been carried out so far. For example, Bilous et al. (2012) made the simultaneous radio ($\sim$ 1.5 GHz) and soft X-ray (1.5 - 4.5 keV) observation with the *Chandra* X-ray observatory. They did not find a significant enhancement of soft X-ray emission coincident with GRPs, but set the 2σ limits on flux changes during GRPs to $\pm$10% and $\pm$30% in the main pulse (hereafter MP) and the interpulse (hereafter IP) emission region, respec-

tively. Bilous et al. (2011) carried out the simultaneous observations at radio ($\sim$ 9 GHz) and γ-ray ($>$ 100 MeV) wavelengths with the *Fermi* satellite. Significant correlation between them was not found and set the upper limit of flux increase at the γ-ray band to four times of the average flux. At higher energy bands, it is difficult to examine a correlation mainly because of insufficient number of photons at high energy bands. For example, Mickaliger et al. (2012) collected more than 9×10^4 GRPs, but the number of γ-ray photons detected with the *Fermi* satellite was only 393. However, setting upper limits on flux increase is important for the future theoretical studies.

We have been investigated a correlation between GRPs and hard X-ray pulses of the Crab pulsar, which has not been examined so far. Using the radio data from a parabola antenna in Japan, either Kashima 34m or Usuda 64m, and the hard X-ray data from the Suzaku satellite, we made simultaneous radio and hard X-ray observations of the Crab pulsar, and found a marginal increase (21.5%, 2.7σ) of hard X-ray flux in a limited phase-angle interval (3-6°) from the peak of the main phase of GRPs for the PIN 15 - 75 keV data (Mikami et al., 2014a). We also searched for a correlation between GRPs and X-ray emissions at 35 - 315 keV (Mikami et al., 2014b). We did not find a significant correlation between them, but set 1σ upper limits on X-ray flux increase concurrent with the GRPs occurring at the main pulse phase to 70% at the peak phase of the X-ray pulse. In this thesis, we analyze the new data acquired in September, 2013 and March, 2014 and try to improve our results. During about 12 hour observation, we collected about 8000 GRPs and $\sim 10^6$ photons. Our observation and data analysis in Section 5.2. The results of our correlation analysis are shown in Section 5.4. In Section 5.5, we discuss the results of our analysis and the possibility of improvement of our study with the next generation X-ray telescopes.

5.2 Observation

The simultaneous observations at radio and X-ray frequencies were made on April 6, 2010, September 16-17, 2013 and March 6, 2014. Our observations are summarized in Table 5.2.

5.2.1 Radio Observation

Our radio observations were conducted with the 34 m antenna at the Kashima Space Technology Center of the National Institute of Information and Communications (NICT), and the 64 m antenna at the Usuda Deep Space Center of the Institute of Space and

Table 5.1: Previous correlation studies between GRPs and emissions at other frequency bands.

Energy range	Satellite or Telescope	Flux variation concurrent with GRPs [in units of average flux]	Ref.
Optical (600-750 nm)	William Herschel Telescope	3% (7.8 σ) increase	(1)
Optical (400-1100 nm)	Palomer	3.2% (7.2 σ) increase	(2)
Soft X-ray (1.5-4.5 keV)	Chandra HRC-S	<10% (2 σ) (MP phase window)	(3)
Soft γ-ray (50-220 keV)	CGRO OSSE	<250% (1 σ) (GRP $\pm$ 5 periods)	(4)
γ-ray (0.1-5 GeV)	Fermi LAT	<400% (95% CL) (on-pulse window)	(5)
Very High Energy γ-ray (>150 GeV)	VERITAS	<500-1000% (95% CL) (around IP GRPs)	(6)

[References. 1: Shearer et al. (2003), 2: Strader et al. (2013), 3: Bilous et al. (2012), 4: Lundgren et al. (1995), 5: Bilous et al. (2011), 6:Aliu et al. (2012)]

Astronautical Science (ISAS). For the observations at Kashima, we sampled the signal of 1378 - 1442 MHz at the Nyquist rate of 128 MHz. Only the right-handed circular polarization signal was recorded. Due to frequent RFI, only the data at 1405–1435 MHz were used. In the observation in 2014, we also sampled the signal of 2182 - 2396 MHz in 8 channels at the Nyquist rate of 64 MHz. However, the total observing time at this frequency band is small (about 3 hours), and it was completely overlapped with the observation time in Usuda. Therefore, we decided to use those 2 GHz data only for precise determination of the value of DM described below.

For the observations at Usuda, 1392 - 1456 MHz at the Nyquist rate of 128 MHz. However, due to frequent RFI, only the data at 1424-1456 MHz were used. The data were dedispersed with the values of DM tabulated in Table 5.2.

For each observation in 2010 and 2013, we adopted the value of DM reported in the Jodrell bank Crab pulsar monthly ephemeris[1] (Lyne et al., 1993) nearest our observation date. For the observation in 2014, the DM value was determined more accurately by aligning the peak times of some strong GRPs simultaneously detected at 1.4 GHz band (Usuda) and 2 GHz band (Kashima) with the accuracy of 1 μs.

From off-pulse phases, we obtained the noise flux and its average fluctuation. Based on those noise level and fluctuation, we calculated the signal-to-noise ratio (S/N) of the

[1]http://www.jb.man.ac.uk/ pulsar/crab.html

time series of the data. The thresholds of the S/N for the GRP selection were determined to collect as many GRPs as possible and avoid contamination of false GRPs. In our analysis, the thresholds were set as 6 at both Kashima and Usuda for all observing sessions.

Table 5.2: Summary of the radio and hard X-ray observations.

Date	Apr. 6, 2010	Sep. 16-17, 2013	Mar. 6, 2014	Total
Observatory	Kashima	Usuda	Kashima/Usuda	
Radio freq. [MHz]	1405–1435	1424–1456	1405–1435 (K) 1424–1456 (U)	
DM [pc/cm^3]	56.8228	56.7679	56.761	
Simultaneous obs. time [hr]	5.5	2.1	4.9 (K: 2.1, U: 2.8)	12.4
No. of GRPs				
MPGRP	2974	1168	3272 (K: 1690, U: 1582)	7414
IPGRP	194	89	273 (K: 139, U: 134)	556
No. of photons				
PIN (15-75 keV)	596293	227262	537865	1361420
GSO	1303586	390459	897228	2591273

For comparison with the arrival times of X-ray photons, the arrival times of the GRPs were then converted to the solar system barycenter with the TEMPO2 package Hobbs et al. (2006).

5.2.2 X-ray Observation

The X-ray data were acquired by the hard X-ray detector (HXD, Kokubun et al., 2007; Takahashi et al., 2007) aboard the Suzaku satellite (Mitsuda et al., 2007, , Figure 5.2.2). The sequence numbers of the data used in our analysis are 105002010, 408008010 and 108012010. We use the PIN data only at 15 - 75 keV and the GSO data in our analysis. We converted their times of arrival to those at the solar system barycenter using the FTOOLS[2] (Blackburn, 1995) task "`aebarycen`". In the observation in 2014, there has been a trouble in assignment of the data time. We used the corrected data by the Suzaku team (Koyama, private communication).

[2]http://heasarc.gsfc.nasa.gov/ftools/

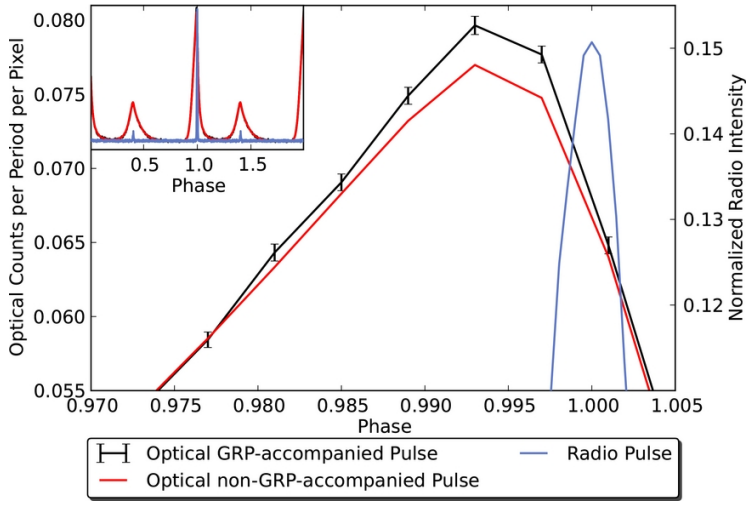

Fig. 5.1.— Average optical pulse profiles reported by Strader et al. (2013). This figure is taken from Figure 1 of Strader et al. (2013). At the peak phase, the optical pulses concurrent with GRPs (black) are reported to be on average $3.2 \pm 0.5\%$ brighter than those of non-GRP periods (red). The radio pulse profile is also shown as a reference.

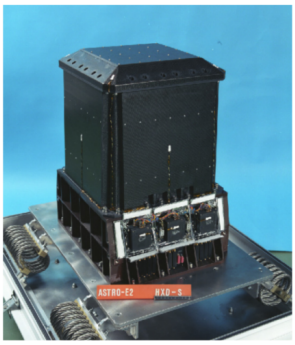

Fig. 5.2.— Left : X-ray Astronomy Satellite, Suzaku (ASTRO–EII). This picture is taken from the JAXA website.
(http://jda-strm.tksc.jaxa.jp/archive/photo/P-021-08577/038c4adcba5244a5426f3dcad4652e2f.jpg)
Right : Hard X-ray Detector (HXD). This picture is taken from Figure 1 of Takahashi et al. (2007).

5.3 Correlation Analysis

We selected the data used in our correlation analysis in the way described below. First, in order to extract the X-ray data not affected by the earth occultation, we stack the X-ray photons every second, and use the data of the time when the number of photons is larger than the threshold value. Next, for the radio data, the time of severe RFI is not used in the subsequent analysis. The resulting simultaneous observation time is 5.5, 2.1 and 4.9 hours for the observations in 2010, 2013 and 2014, respectively. The numbers of the GRPs and X-ray photons obtained during those observing sessions are summarized in Table 5.2. From the whole of simultaneous radio and X-ray observations, we accumulated 7414 and 556 GRPs occurring at the main pulse (hereafter MPGRPs) and the interpulse phase (hereafter IPGRPs), respectively. The expected number of the pseudo-GRPs was at most a few for all observing sessions. The amplitude (peak S/N) distributions of the obtained GRPs during each observing session is shown in Figure 5.3 to 5.6. The power-law indices Γ obtained in those distributions are consistent with the previous studies (e.g. Mickaliger et al., 2012). The examples of the obtained GRPs from the three observing sessions are also shown in Figure 5.7 to 5.10.

Then, the mean X-ray pulse profiles are made every $\sim$ 5000 seconds by the folding procedure described in Section 3.2.2. We determine the peak phase of each pulse profile by fitting a Gaussian function with a constant. The determined peak phases are plotted in Figure 5.11. While the peak phases in the observations of 2010 and 2013 are stable, those in the observation in 2014 were gradually shifted due to the trouble of time assignment mentioned in the previous section. Since it is sure that the corrected arrival times of the photons do not vary more than one pulse period (Koyama, private communication), We correct the time of arrival of each photon based on the peak

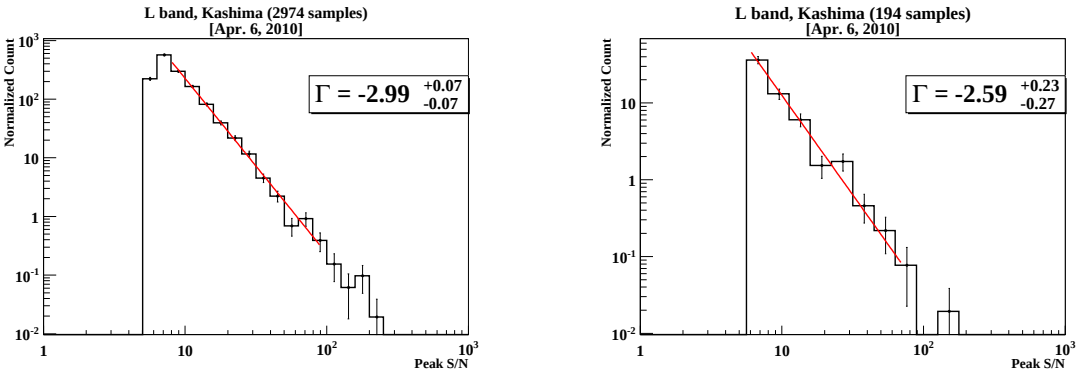

Fig. 5.3.— Peak S/N distribution in 10 μs time bin for the MPGRPs (left) and the IPGRPs (right) detected on April 6, 2010.

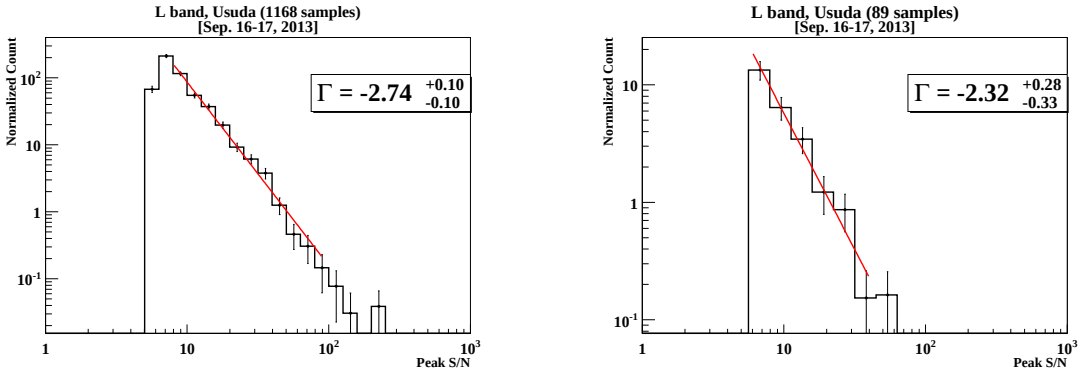

Fig. 5.4.— Peak S/N distribution in 10 μs time bin for the MPGRPs (left) and the IPGRPs (right) detected on September 16–17, 2013.

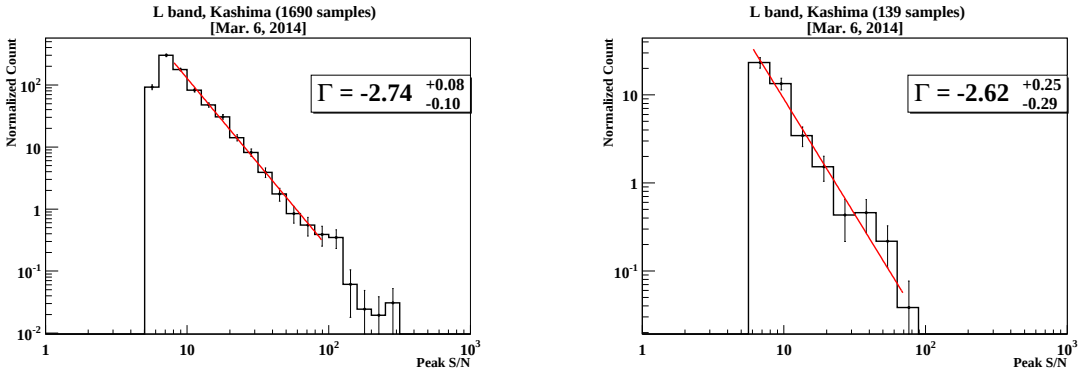

Fig. 5.5.— Peak S/N distribution in 10 μs time bin for the MPGRPs (left) and the IPGRPs (right) detected in the Kashima 34m antenna on March 6, 2014.

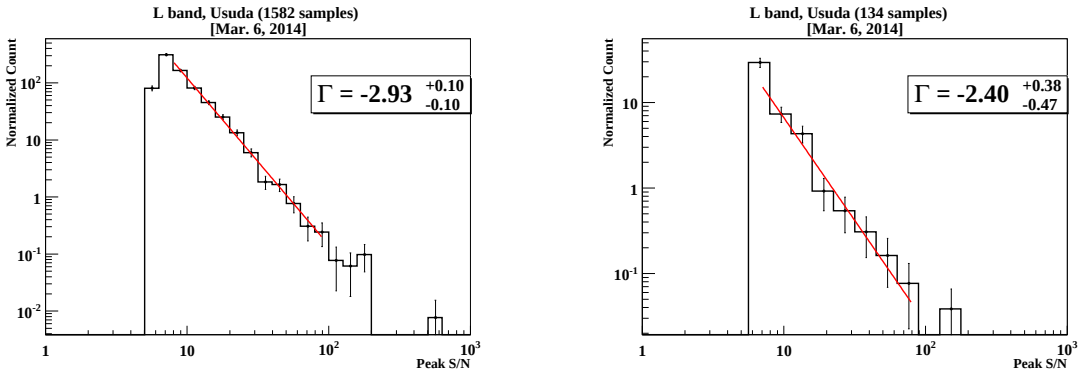

Fig. 5.6.— Peak S/N distribution in 10 μs time bin for the MPGRPs (left) and the IPGRPs (right) detected in the Usuda 64m antenna on March 6, 2014.

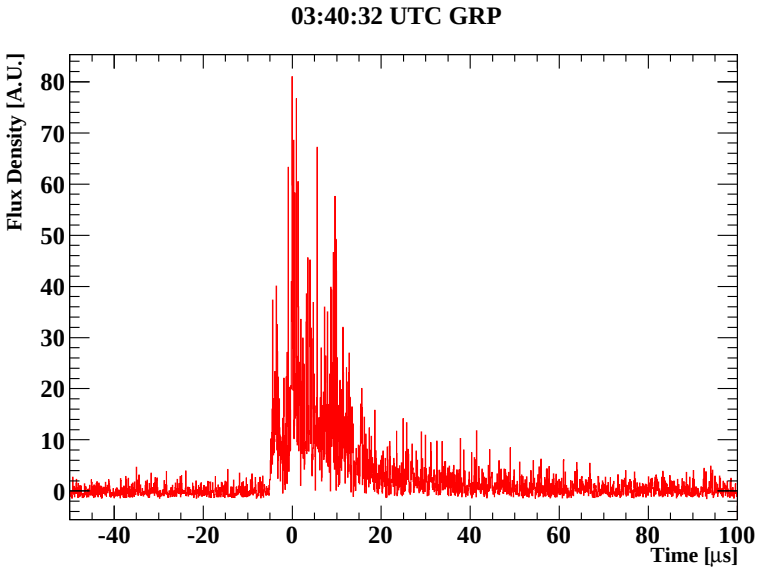

Fig. 5.7.— The light curve of the strongest GRP detected with the Kashima antenna on April 6, 2010.

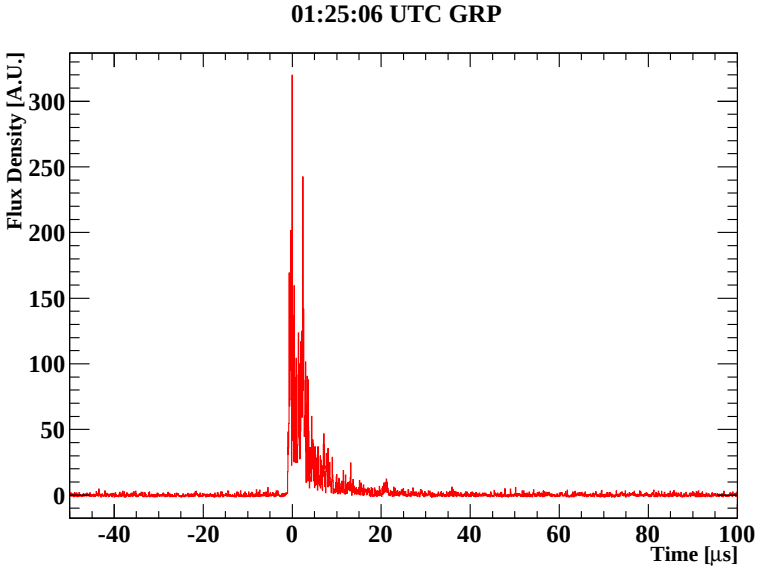

Fig. 5.8.— The light curve of the strongest GRP detected with the Usuda antenna on September 17, 2013.

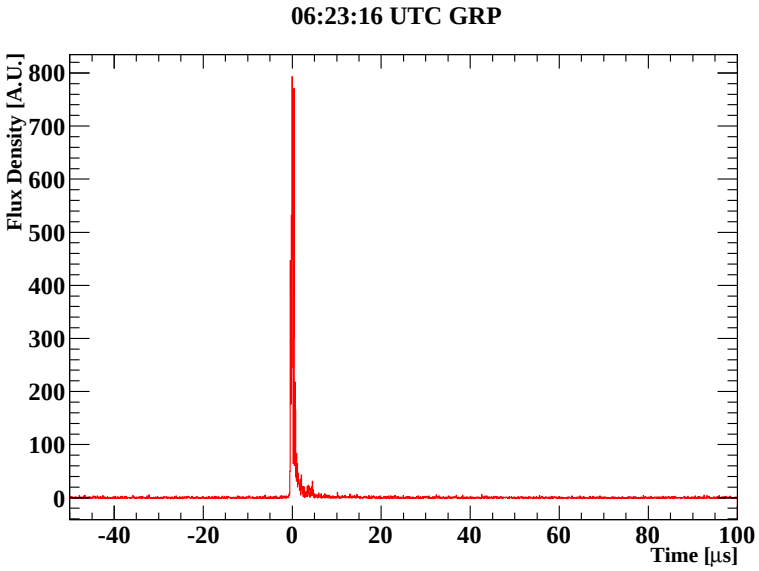

Fig. 5.9.— The light curve of the strongest GRP detected with the Usuda antenna on March 6, 2014.

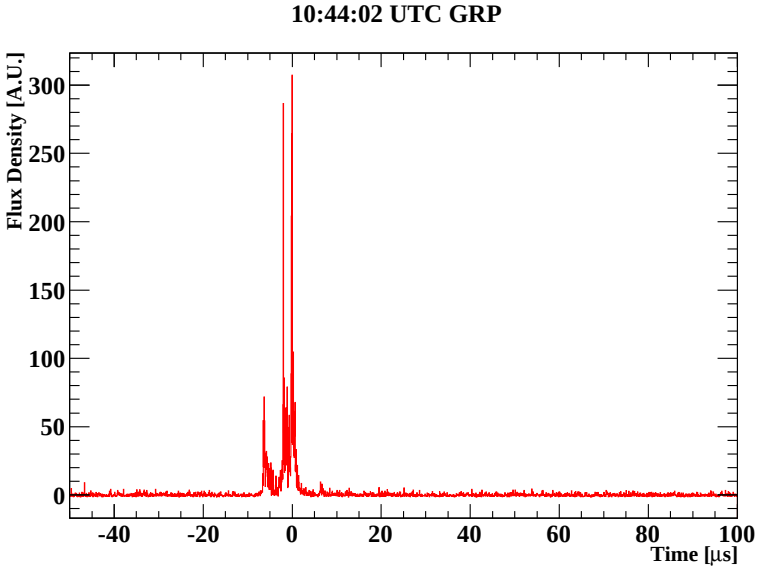

Fig. 5.10.— The light curve of the strongest GRP detected with the Kashima antenna on March 6, 2014.

phases of the pulses obtained in the other two observations. The pulse peak phases in the observation in 2014 after correction are shown in Figure 5.12.

The bin width of each profile is adopted to 0.05 period, taking into account the absolute timing accuracy of the Suzaku HXD ($\sim 360\mu$s) and the additional error in time assignment for the data in the observation in 2014.

We define the "off-pulse" phase interval as the range from -0.45 to -0.15, and calculate the off-pulse count rate, $f_{\rm BG}$, by fitting a constant function to the data in that range. The value of $f_{\rm BG}$ for each observing session is tabulated in Table 5.3. For the PIN data, we do not find a significant difference of the values of $f_{\rm BG}$ in the three observing sessions. On the other hand, for the GSO data, the values of $f_{\rm BG}$ are different from each other. We normalize the data by multiplying the factor C so that the values of $f_{\rm BG}$ are equal to that in the observation in 2014. Then, we subtracted $f_{\rm BG}$ from the raw count rate in each phase bin because we are interested in flux variability of only the "pulse" component.

5.4 Results

The pulse profiles made from the PIN and GSO data are displayed in Figure 5.13 to 5.28. For the data in each observing session, we divide the photons into the two groups; one includes the photons detected in the same rotational periods as GRPs, and the other includes the photons detected in the non-GRP periods. We make the folded profiles from each group of photons, and compare the count rate (flux) of them. We define a flux enhancement at the peak phase $E_{\rm p}$ and its significance $s_{\rm p}$ as

$$E_{\rm p} \equiv \frac{f_{\rm p,onGRP} - f_{\rm p,offGRP}}{f_{\rm p,offGRP}} \cdot 100[\%], \tag{5.1}$$

and

$$s_{\rm p} \equiv \frac{f_{\rm p,onGRP} - f_{\rm p,offGRP}}{\sqrt{\sigma^2_{\rm p,onGRP} + \sigma^2_{\rm p,offGRP}}}[\sigma], \tag{5.2}$$

respectively. Here, $f_{\rm p,onGRP}$ and $f_{\rm p,offGRP}$ denote the count rate of X-ray photons at the peak phase during the GRP periods and the off-GRP periods, respectively. $\sigma_{\rm p,onGRP}$ and $\sigma_{\rm p,offGRP}$ are those 1σ statistical errors. Significance of flux enhancement at the peak phase is at most $\sim 2.5\sigma$. We do not find a significant increase of X-ray flux coincident with GRPs, but at a confidence level of 95%, we can set its upper limits to 33% and 88% for the PIN data concurrent with the MPGRPs and the IPGRPs, respectively. For the GSO data, the upper limit for flux increase concurrent with the MPGRPs and the IPGRPs can be set to 63% and 193% , respectively, at a confidence level of 95%.

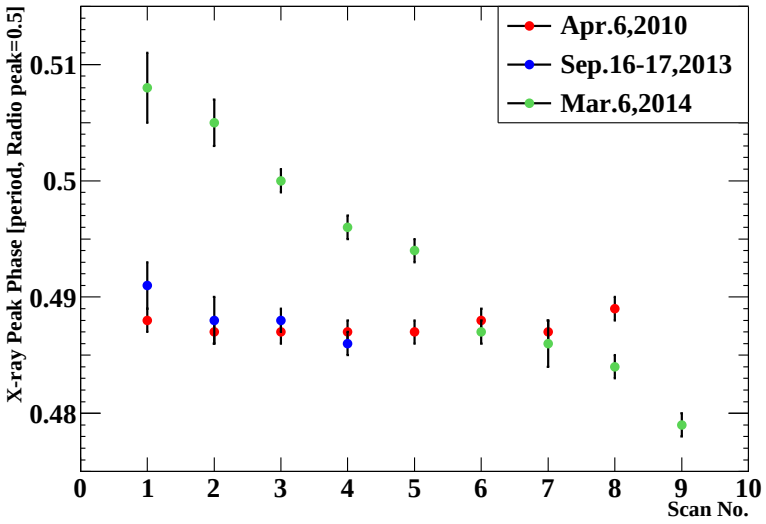

Fig. 5.11.— The peak phases of the average X-ray pulse profiles in each $\sim$ 5000 second observation ("scan"). The peak phases of the mean radio pulses during the three observing sessions are defined as 0.5. The additional correction of the data time of the observation in 2014 is not done.

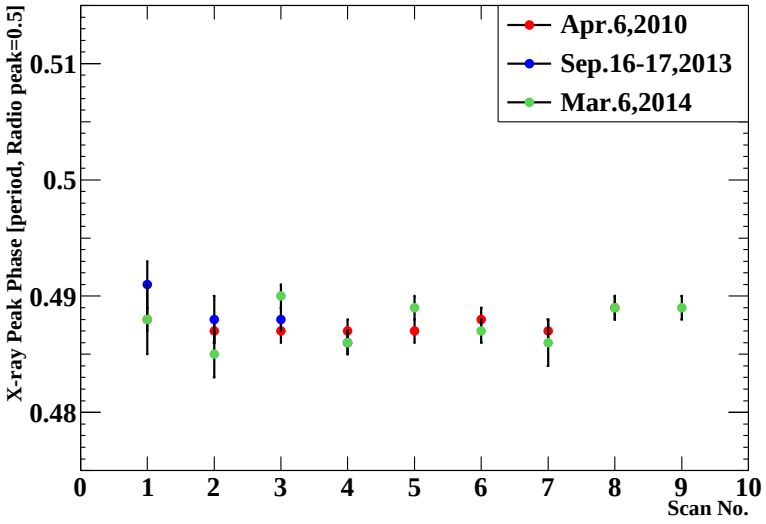

Fig. 5.12.— Same as Figure 5.11, but the additional correction of the data time of the observation in 2014 is carried out.

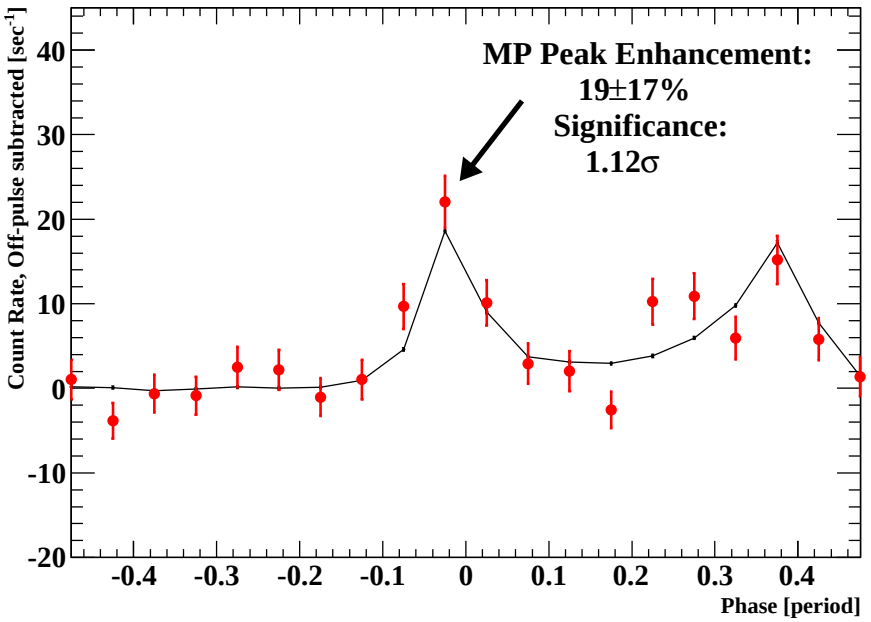

Fig. 5.13.— Average pulse profiles at PIN 15-75 keV band for the observation on April 6, 2010. The average profile coincident with MPGRP periods is represented by the red data points, and the profile averaged over non-GRP periods is represented by the black line. Phase 0 corresponds to the peak phase of the average radio pulse profile.

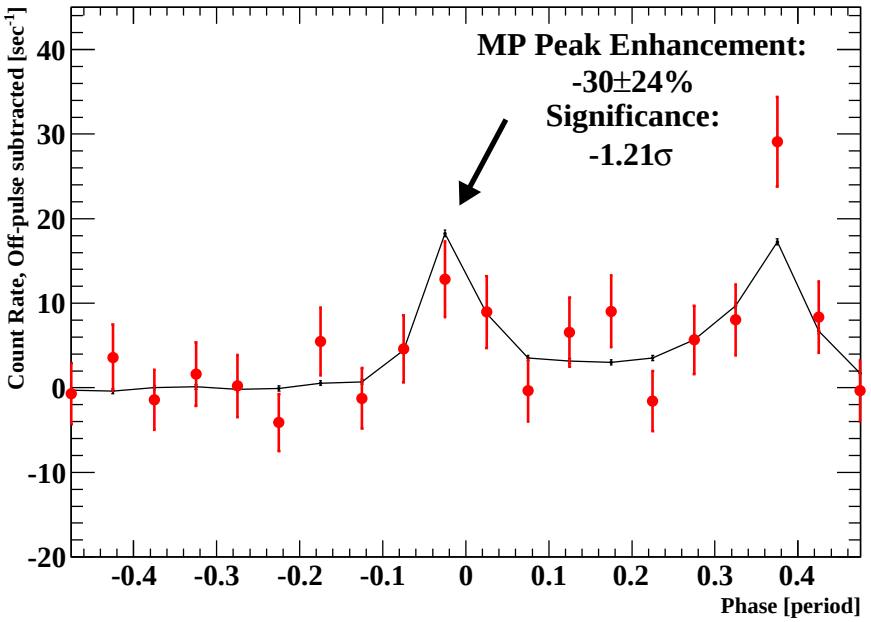

Fig. 5.14.— Same plot as Figure 5.13, but for the observation on September 16-17, 2013.

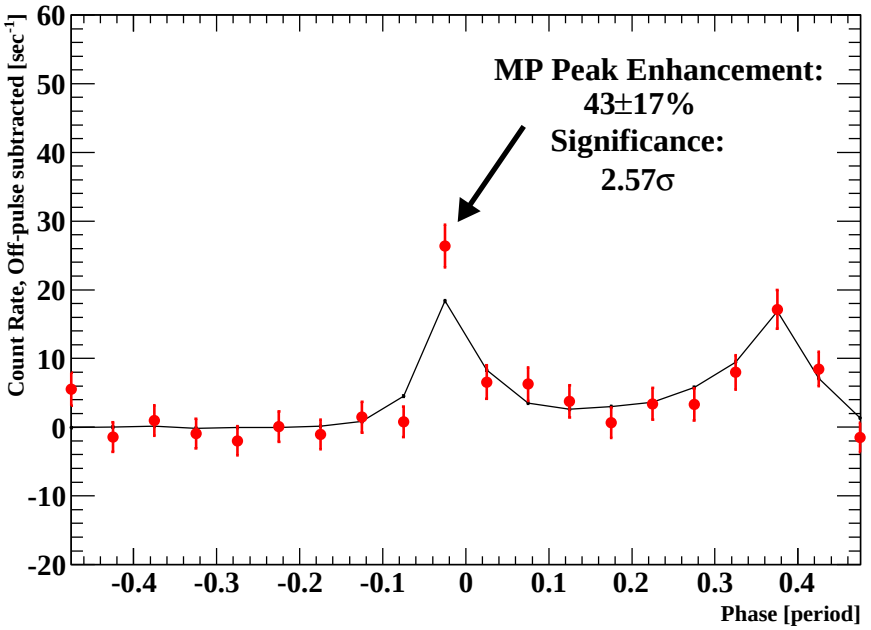

Fig. 5.15.— Same plot as Figure 5.13, but for the observation on March 6, 2014.

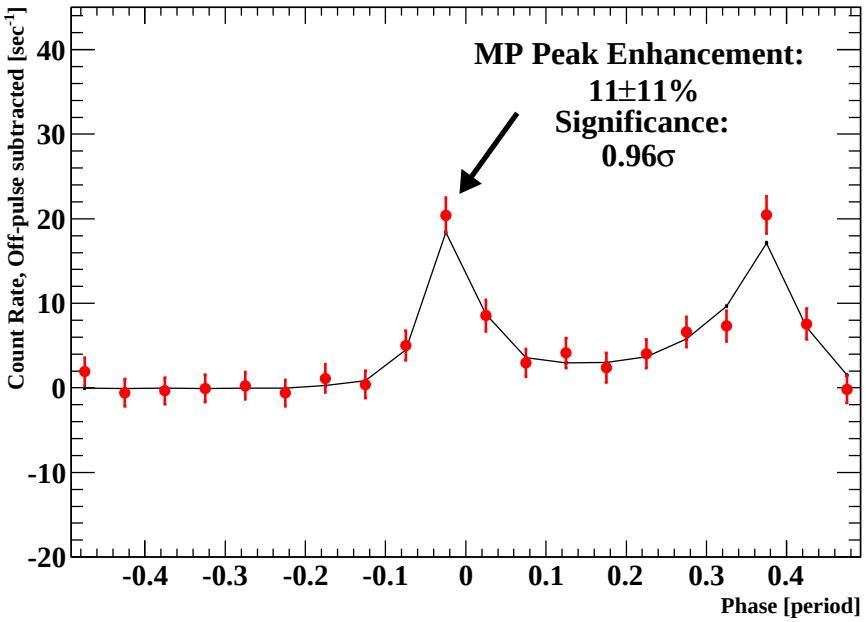

Fig. 5.16.— Same plot as Figure 5.13, but the data of the three observations are merged together.

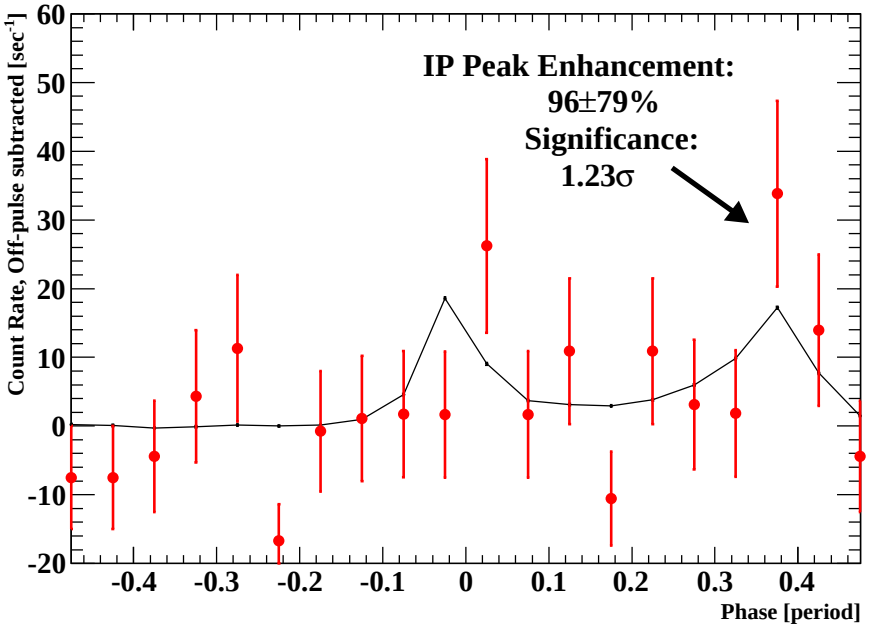

Fig. 5.17.— Average pulse profiles at PIN 15-75 keV band for the observation on April 6, 2010. The average profile coincident with IPGRP periods is represented by the red data points, and the profile averaged over non-GRP periods is represented by the black line. Phase 0 corresponds to the peak phase of the average radio pulse profile.

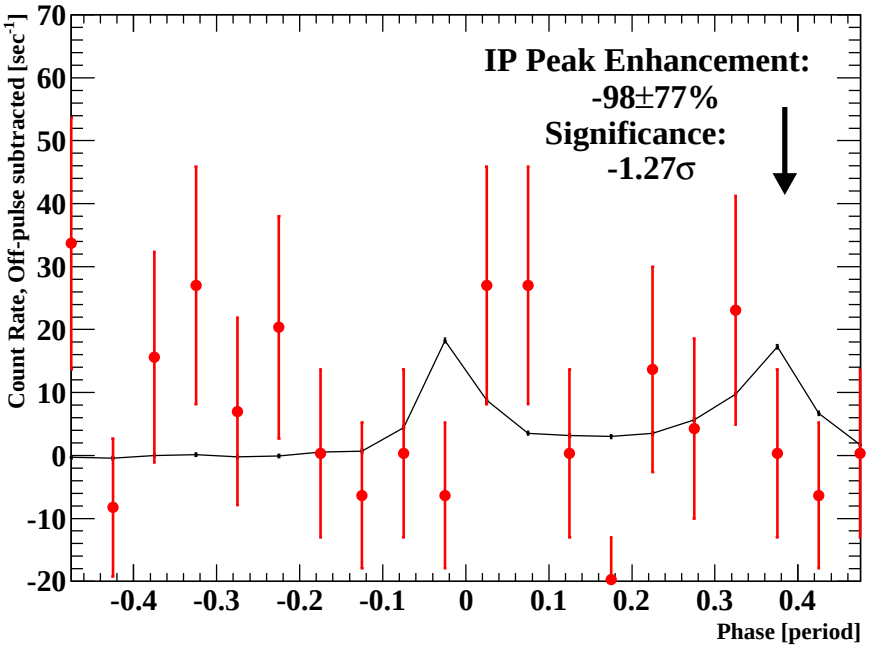

Fig. 5.18.— Same plot as Figure 5.17, but for the observation on September 16-17, 2013.

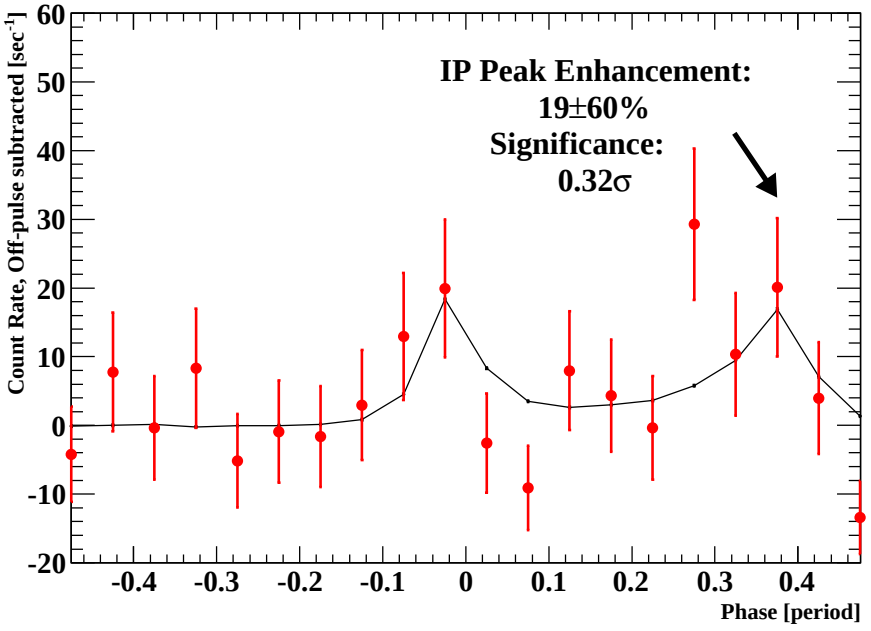

Fig. 5.19.— Same plot as Figure 5.17, but for the observation on March 6, 2014.

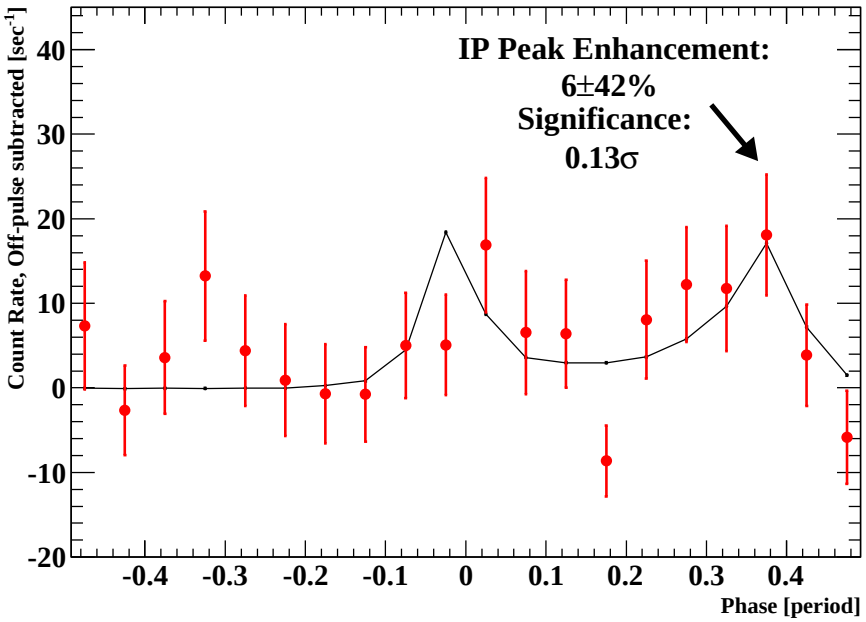

Fig. 5.20.— Same plot as Figure 5.17, but the data of the three observations are merged together.

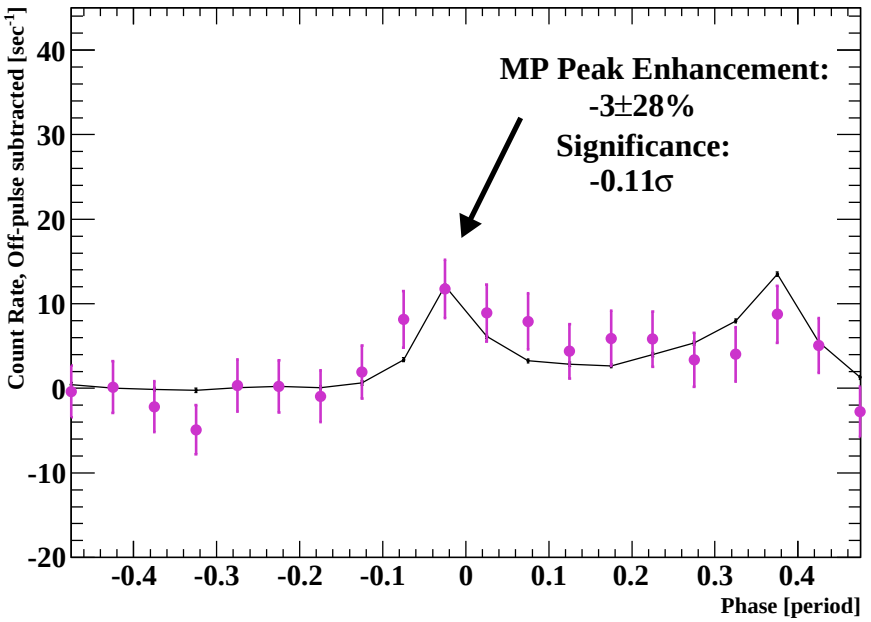

Fig. 5.21.— Average pulse profiles at GSO band for the observation on April 6, 2010. The average profile coincident with MPGRP periods is represented by the purple data points, and the profile averaged over non-GRP periods is represented by the black line. Phase 0 corresponds to the peak phase of the average radio pulse profile.

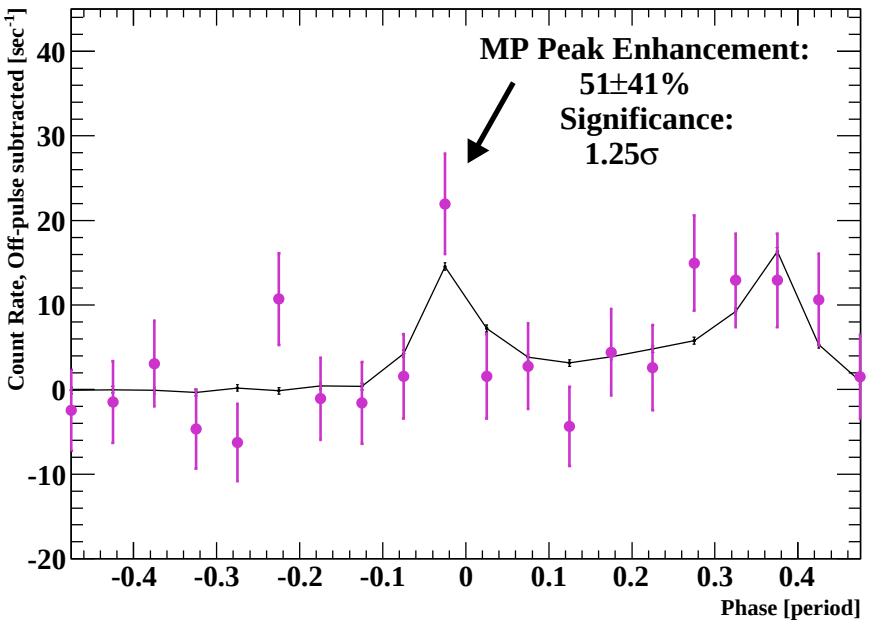

Fig. 5.22.— Same plot as Figure 5.21, but for the observation on September 16-17, 2013.

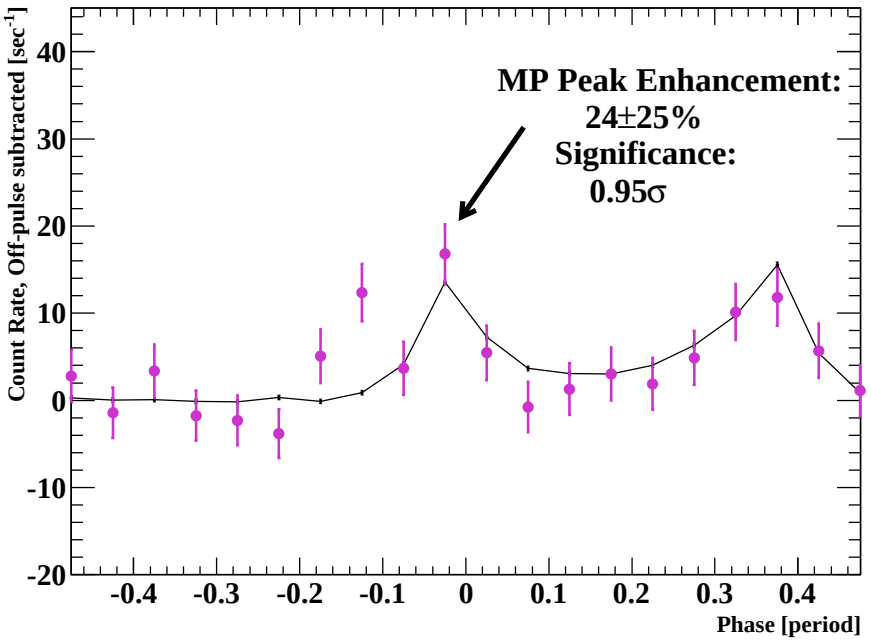

Fig. 5.23.— Same plot as Figure 5.21, but for the observation on March 6, 2014.

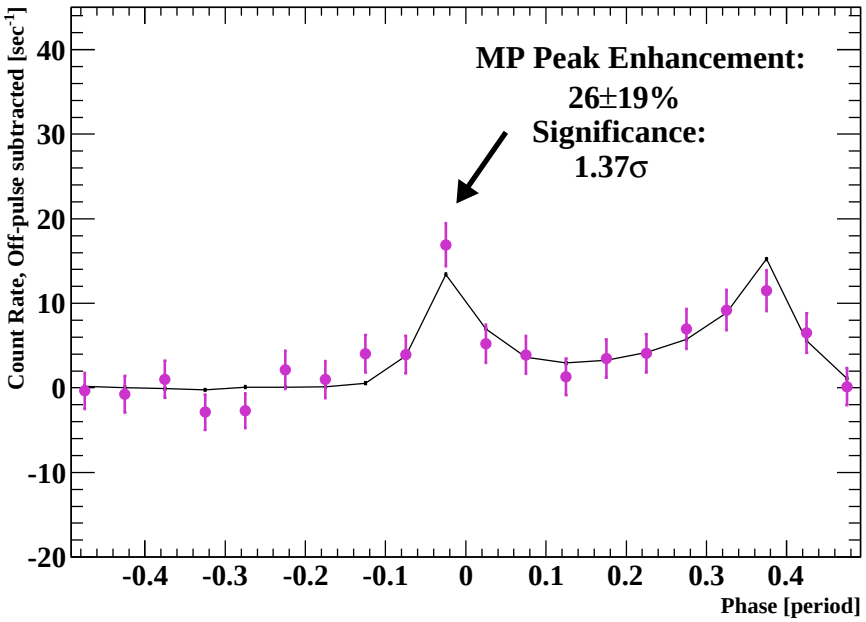

Fig. 5.24.— Same plot as Figure 5.21, but the data of the three observations are merged together.

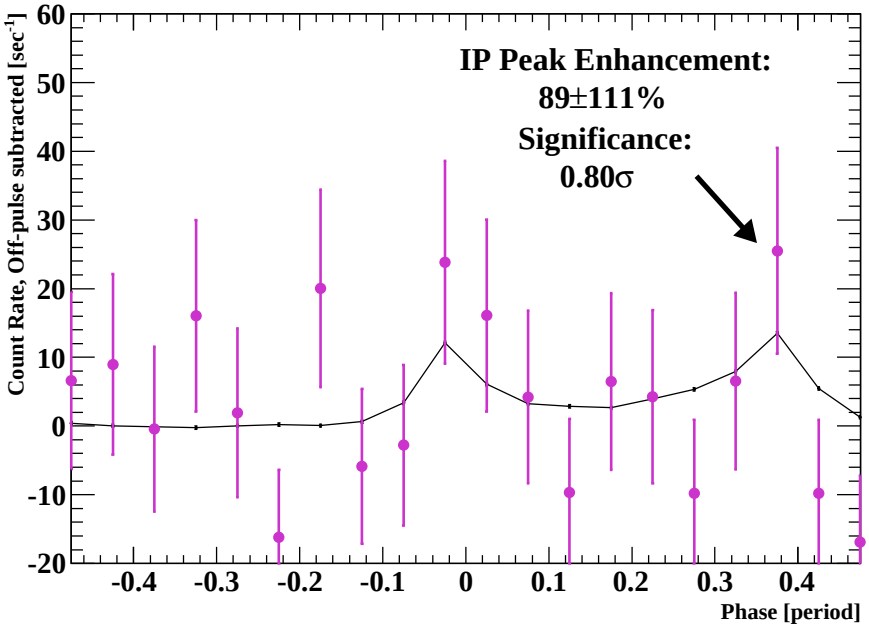

Fig. 5.25.— Average pulse profiles at GSO band for the observation on April 6, 2010. The average profile coincident with IPGRP periods is represented by the purple data points, and the profile averaged over non-GRP periods is represented by the black line. Phase 0 corresponds to the peak phase of the average radio pulse profile.

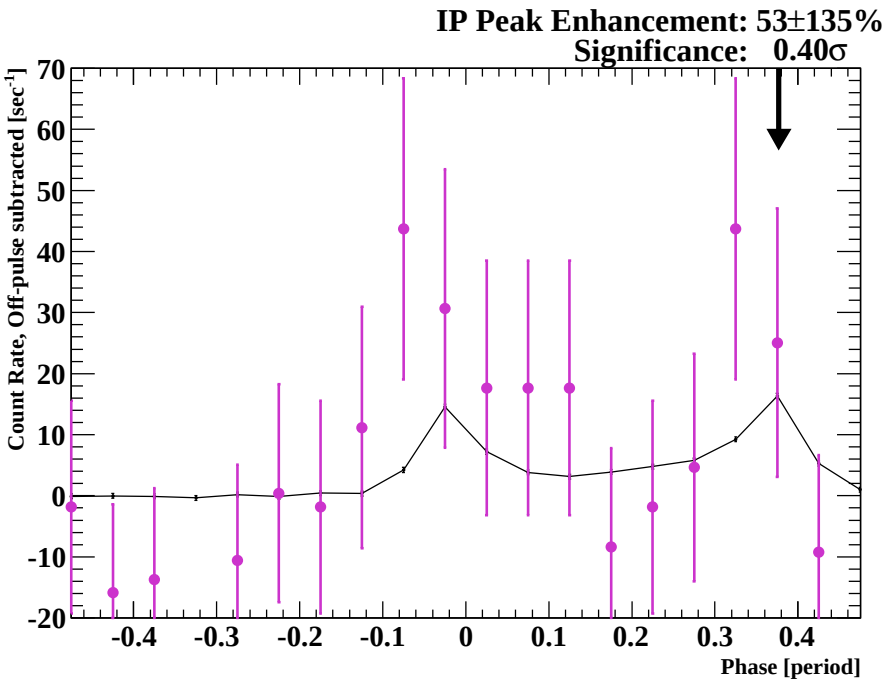

Fig. 5.26.— Same plot as Figure 5.25, but for the observation on September 16-17, 2013.

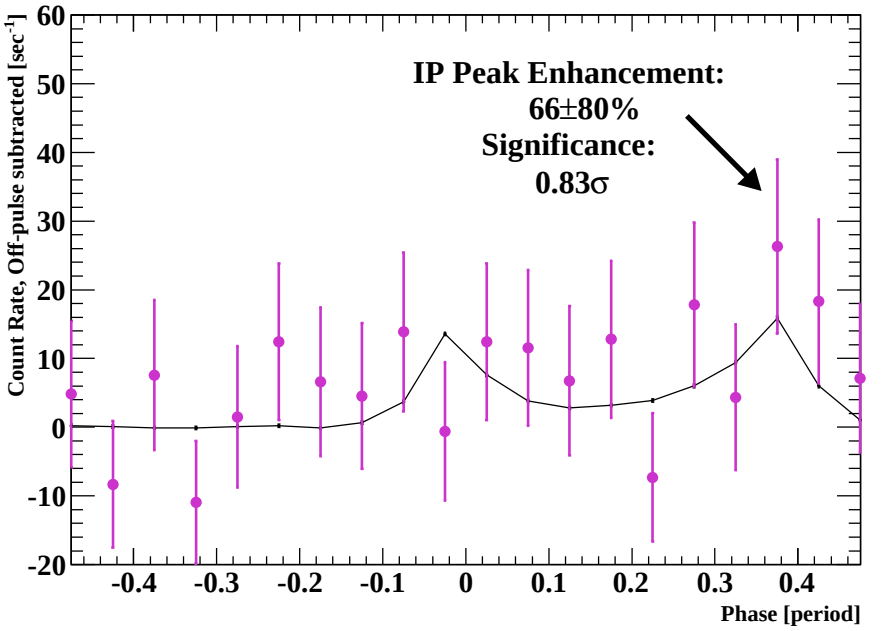

Fig. 5.27.— Same plot as Figure 5.25, but for the observation on March 6, 2014.

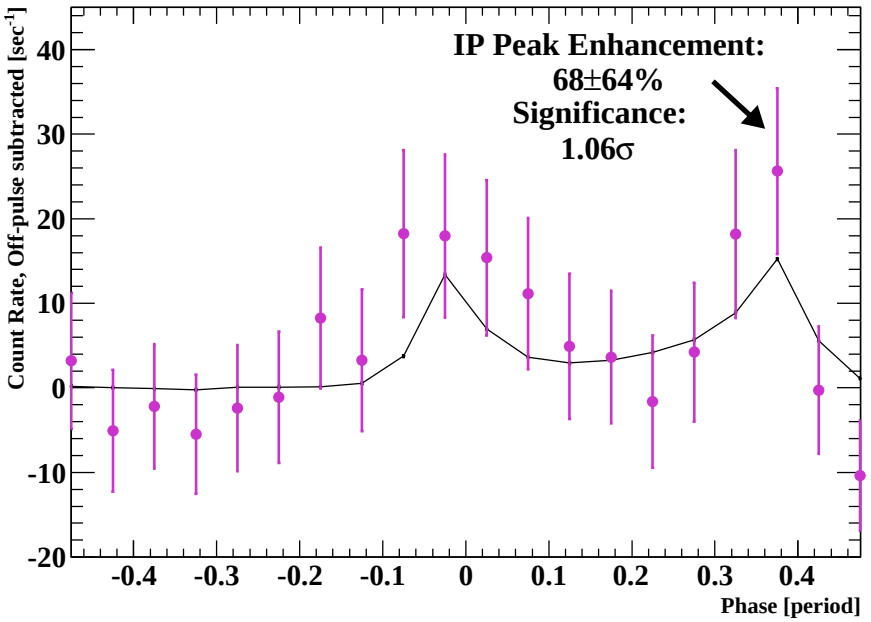

Fig. 5.28.— Same plot as Figure 5.25, but the data of the three observations are merged together.

Table 5.3: Derived parameters from the hard X-ray pulses. For more details, see text.

Date		PIN/MPGRP	PIN/IPGRP	GSO/MPGRP	GSO/IPGRP
Apr. 6, 2010	$f_{\rm BG}$	25.88 ± 0.07		61.83 ± 0.10	
	C	1		0.767	
	$E_{\rm p}$	$19 \pm 17\%$	$96 \pm 79\%$	$-3 \pm 28\%$	$89 \pm 111\%$
	$s_{\rm p}$	1.12σ	1.23σ	-0.11σ	0.80σ
Sep. 16-17, 2013	$f_{\rm BG}$	26.35 ± 0.11		48.60 ± 0.15	
	C	1		0.975	
	$E_{\rm p}$	$-30 \pm 24\%$	$-98 \pm 77\%$	$51 \pm 41\%$	$53 \pm 135\%$
	$s_{\rm p}$	-1.21σ	-1.27σ	1.25σ	0.40σ
Mar. 6, 2014	$f_{\rm BG}$	26.47 ± 0.07		47.38 ± 0.10	
	C	1		1	
	$E_{\rm p}$	$43 \pm 17\%$	$19 \pm 60\%$	$26 \pm 25\%$	$66 \pm 80\%$
	$s_{\rm p}$	2.57σ	0.32σ	1.01σ	0.83σ
Total	$E_{\rm p}$	$11 \pm 11\%$	$6 \pm 42\%$	$26 \pm 19\%$	$68 \pm 64\%$
	$s_{\rm p}$	0.96σ	0.13σ	1.37σ	1.06σ

5.5 Summary and Future Prospects

We made the simultaneous radio and hard X-ray observations of the Crab pulsar on April 6, 2010, September 16-17, 2013 and March 6, 2014. We did not find a significant flux enhancement of the X-ray pulses concurrent with GRPs. However, for the PIN 15-75 keV data coincident with the MPGRPs and the IPGRPs, the upper limit for the flux enhancement can be set to 33% and 88%, respectively, at a confidence level of 95%. For the GSO data, the upper limit for the flux enhancement coincident with the MPGRPs and the IPGRPs at a confidence level of 95% can be also set to 63% and 193%, respectively. From our results, we can not yet conclude an existence of a correlation between GRPs and hard X-rays from the Crab pulsar. In this section, we qualitatively discuss a correlation between GRPs and pulses in higher energy bands at first, and we also roughly estimate the improvement of our results expected with the future hard X-ray telescope.

In the Crab pulsar, the average radio pulse profile is roughly aligned with the X-ray profile (see Figure 2.6). Since the occurrence phases of the Crab GRPs are aligned with the average radio profile, they are also aligned with the X-ray profile. Therefore, it may be suggested that the radio (GRP) emission may occur at the same location as the X-ray emission. As mentioned before, the optical or X-ray emission from the Crab pulsar can be modeled by the incoherent synchrotron radiation from the outer gap region (e.g. Takata & Chang, 2007). Therefore, it may be suggested that GRPs also generate within the outer gap region. As we also mentioned in Section 5.1, the optical pulses concurrent with the Crab GRPs showed an enhancement at only the peak phase (Shearer et al., 2003; Strader et al., 2013). This result may imply that within the outer gap region, only the limited region is affected by the occurrence of GRPs. Therefore, some process(es) might generate the GRP emission in the limited region within the outer gap region, and affect the emission at higher energy bands.

In order to examine the correlation more accurately, we need to collect more X-ray photons with a good timing precision. Since the flux enhancement which we discuss is the photon count rate, the accuracy of the flux enhancement is improved roughly by a factor of $\sim T_{\rm obs}^{-1/2}$ assuming a Poisson statistics, where $T_{\rm obs}$ is the duration of an observation. The flux enhancement coincident with GRPs seen at the optical band was $\sim$3% at the peak phase (Shearer et al., 2003; Strader et al., 2013). In the discussion below, we roughly estimate the observation time required to examine 3% enhancement with 1σ accuracy, assuming that the same enhancement is seen at the hard X-ray band.

We also take into account that the bin width within which Shearer et al. (2003) or Strader et al. (2013) detected optical flux enhancement is 0.01period, 5 times narrower than ours.

With the Suzaku HXD, the observation time required to examine 3% enhancement with 1σ accuracy at 15 - 75 keV is $\sim 8.3 \times 10^2$ hours, which is ~ 67 times longer than our work. Now that the Suzaku satellite completed the scientific mission[3], we expect to improve our correlation study with the next generation X-ray telescopes. In Table 5.4, we summarize the next generation X-ray telescopes covering the hard X-ray band. At the hard X-ray band, the number of photons from the Crab pulsar becomes larger at lower energies (e.g. Kuiper et al., 2001). Therefore, the effective areas of the telescopes at 15 keV corresponding to the minimum energy of the PIN data used in our analysis are summarized in Table 5.4. NuSTAR (Nuclear Spectroscopic Telescope ARray, Harrison et al., 2013) is the first telescope focusing on high-energy X-ray band, and was launched on June 13, 2012. The observation of the Crab pulsar and nebula with NuSTAR was reported by Madsen et al. (2015). The raw (not live-time corrected) pulse profile is distorted due to 2.5 ms data readout, and therefore additional correction may be needed in the data analysis. However, the effective area of NuSTAR is about four times larger than the Suzaku HXD at 15 keV and the observation time needed to examine 3% enhancement with 1σ accuracy will be $\sim 2.0 \times 10^2$ hours. ASTRO-H (Takahashi et al., 2014) is the sixth satellite in a series of X-ray astronomy missions by the Institute of Space and Astronautical Science (ISAS) of Japan Aerospace Exploration Agency (JAXA), and is scheduled to be launched by the end of Japanese fiscal year 2015 (e.g. Ohno et al., 2015). Its effective area is $\sim 5-6$ times larger than that of the Suzaku satellite at 15 keV. We plan to improve our results with these two satellites. LOFT (the Large Observatory For X-rat Timing, Feroci et al., 2012) was one of the candidates of an Medium-size mission selection (M3). The Large Area Detector (LAD) is planned to achieve an effective area of $\sim 10\mathrm{m}^2$, about 10^2 times larger than the Suzaku HXD, or about 20 times larger than the area of the past timing mission such as RXTE (e.g. Bradt et al., 1993). If we compare only the effective areas of the Suzaku HXD and LOFT, the required time to examine 3% enhancement with 1σ accuracy will be about ~ 1.4 hours. Mignani et al. (2015) also simulated observed flux enhancement concurrent with GRPs using the LAD. Assuming that GRPs occurred every second ($\sim 3\%$ of rotational period) and X-ray flux was enhanced by 3% accompanied with GRPs, they estimated that 3% peak flux enhancement could be detected at 13.7 σ during an observation of

[3]http://global.jaxa.jp/press/2015/08/20150826_suzaku.html

$\sim 10^4$ seconds . The energy coverage of LOFT is lower than the Suzaku HXD, and therefore, the collected number of photons may be relatively large due to the spectrum of the Crab pulsar as described above. However, the LOFT satellite may be a powerful tool for correlation studies in the future.

Revealing the link between coherent and incoherent emission from pulsars is important for understanding the physical mechanism in the pulsar magnetosphere. The future X-ray telescopes described above will give a new perspective in our knowledge.

Table 5.4: Performance parameters of some telescopes covering the hard X-ray band.

Telescope (Detector)	Suzaku[1] (HXD)	NuSTAR[2]	ASTRO-H[3] (HXT)	LOFT[4] (LAD)
Energy range	10 - 600 keV	3 - 78.4 keV	5 - 80 keV	2 - 30 keV
Timing resolution	61μs	2μs	25.6μs	10μs
Effective area (at 15 keV)	$\sim 130\mathrm{cm}^2$ (PIN)	$\sim 550\mathrm{cm}^2$	$\sim 700\mathrm{cm}^2$	$\sim 8 \times 10^4\mathrm{cm}^2$
Launch Date	July, 2005	June, 2012	2016 ?	?

[1] Suzaku technical description. See https://heasarc.gsfc.nasa.gov/docs/suzaku/prop_tools/suzaku_td/

[2] Harrison et al. (2013)

[3] Takahashi et al. (2014). The data of the effective area is extrapolated from Mori et al. (2014). The total effective area of HXT-1 and HXT-2 is shown.

[4] Feroci et al. (2012)

Chapter 6

Overall Conclusions

In this thesis, we study Giant Radio Pulses (GRPs) from the Crab pulsar in terms of the multi-wavelength observations. Here, we summarize the results from our observations.

- We make the simultaneous observation of the GRPs from the Crab pulsar at 0.3, 1.6, 2.2, 6.7 and 8.4 GHz, whose frequency coverage ($\sim$ 1.5 decades) is the most broadband among ever reported. We collect more than 3000 GRPs, which are the largest samples among the past multi-frequency observations.

- We find that at the bands from 0.3 to 2.2 GHz, about 70% or more of the GRP spectra are consistent with single power-laws.

- The spectral indices of GRPs at the bands from 0.3 to 2.2 GHz are distributed widely from the range which was already reported by the previous studies to the range harder than ever reported.

- We perform the stacking analysis to obtain weak GRPs below the detection limit. From this analysis, we find dim GRPs at 0.3 GHz correlated with the 1.6/2.2-GHz GRPs. The average spectral index for such dim samples at 0.3 GHz is harder than the bright GRPs and normal pulses. Since the dim and hard GRPs occupy about a half of our GRP samples, it might be suggested that most of GRPs have intrinsically harder spectra than those suggested in the previous studies.

- We find an apparent correlation between fluences and spectral indices of GRPs, which indicate that less energetic pulses tend to show harder spectra. The result of the stacking analysis supports such a correlation. To decide whether the correlation is true or not, we need to collect more GRP samples and to improve our detection limits.

- We make the simultaneous radio and hard X-ray observations of the Crab pulsar. We set the first constraint on the flux enhancement coincident with GRPs at hard X-ray band.

As we mentioned in Chapter 1, no widely accepted, self-consistent model of the pulsar magnetosphere is constructed. In this situation, it is premature that we determine the emission mechanism of GRPs from our results and what we should do now is to accumulate observational results to approach the emission mechanism. If the correlation between fluences and spectral indices of GRPs which we find is true, it will be absolutely a clue to understand the emission mechanism of GRPs. Also, if the GRPs truly have harder spectra than normal pulses, it will be useful to construct the theoretical models of GRPs in the future. We also draw the future prospects from our results. We discuss them below.

It is interesting that all the IPGRP detected at X band are not detected at the other frequency bands. Since the occurrence phases of the Crab GRPs at $\gtrsim$ 4 GHz are slightly different from those at lower frequency bands (Cordes et al., 2004, see also Figure 2.2), the particles generating $\gtrsim$ 4 GHz emission may be originated from another region. At the frequency higher than S band, few GRPs can be collected due to our limited sensitivity or the effect of the interstellar scintillation. The statistical study of the GRP spectra including $\gtrsim$ 4 GHz will be one of our future work.

We also found the spectra inconsistent with single power-laws. In our work, we integrate all the pulse components within one GRP and investigate the total fluence spectra. However, some GRPs have distinct components in one GRP. For those GRPs, different spectral components may be superposed in the fluence spectra. Looking at the GRP profiles, there is a diversity of microstructures of GRPs and it seems difficult to make a systematic analysis of the structures of GRPs. Therefore, we neglected them in this work. Investigating a relationship between fine structures of GRPs and spectral features may bring deep insight into the spectra of GRPs. We will work on this subject.

In many previous studies, only a small number of strong GRPs were analyzed. We focused on a number of "weak GRPs" at P band through the method of the stacking analysis. Those GRPs can not be found at a single frequency band, and can be detected making use of the information that they are detected at the other frequency bands. As a result, we detected "dim-hard" GRPs, and from them, it might be suggested that GRPs might have intrinsically harder spectra than normal ones, or that GRPs might require such emission mechanism that their brightness and spectral hardness are correlated each other. Due to the limited sensitivity of our observation, those hypotheses are still

only speculations. They should be tested in the future by high sensitivity observations and more GRP samples.

The spectral study of GRPs from the pulsars other than the Crab pulsar will be also interesting. According to Popov & Stappers (2003), in PSR B1937+21, there was no GRP detected simultaneously at 1.4 GHz and 2.2 GHz. If their observation at 1.4 and 2.2 GHz can be associated with our observation L and S bands (see Section 4), we will not find GRPs simultaneously detected at L and S bands, which correspond to Group (II) GRPs and a part of Group (I) GRPs in Section 4. They occupied about a half of all the GRP samples in the case of the Crab pulsar. Although the detection rate of the GRPs from PSR B1937+21 is much smaller than that of the Crab pulsar, it is possible to test their result using our Japanese observation network. Multi-frequency observations of the GRPs from the pulsars other than the Crab pulsar may reveal the pulsar-dependent spectral features. This subject will be also carried out as a future work.

We also investigated a correlation between hard X-ray pulses and GRPs from the Crab pulsar. We do not find any significant correlations between them, but set upper limits of flux enhancement concurrent with GRPs. The upper limits which we set will be improved with the future X-ray telescope. As we mentioned in Section 5.5, the correlation study with the LOFT satellite will be very promising. As we mentioned in Chapter 5, the optical pulses concurrent with the Crab GRPs showed an enhancement at only the peak phase (Shearer et al., 2003; Strader et al., 2013). This result may imply that within the outer gap region, only the limited region may be affected by the occurrence of GRPs. Therefore, some process(es) might generate the GRP emission in the limited region within the outer gap region, and might affect the emission at higher energy bands. If a sufficient number of photons is collected with a sufficient timing precision, we can determine more precisely the pulse phase showing enhancement of X-ray flux concurrent with GRPs. This may reveal the emission region of GRPs and the corresponding X-ray emission region.

Appendix A

Flux Density and Error

The flux density in each time bin τ is calculated from its signal-to-noise ratio S/N as

$$S_\tau = S_1(\mathrm{S/N})_\tau, \tag{A.1}$$

where S_1 is obtained from the radiometer equation (Dicke, 1946; Lorimer & Kramer, 2004) as

$$S_1 = \frac{S_{\mathrm{CN}} + \mathrm{SEFD}}{\sqrt{\Delta\nu \Delta t n_{\mathrm{p}}}}. \tag{A.2}$$

Here, S_{CN} is the received flux density of the Crab nebula in each frequency channel, and SEFD is the system equivalent flux density. The definitions of $\Delta\nu$, Δt, and n_{p} are the observation bandwidth [Hz], the width of the time bin [s], and the number of polarization directions, respectively. In our observation, $n_{\mathrm{p}} = 1$ in all the observatories.

For L, S and C bands, we used the Crab nebula itself as a calibration source. The method to obtain S_{CN} is as follows. We assume that the antenna pattern is axisymmetric Gaussian one,

$$P(\theta) = \exp\left[-4\ln 2 \left(\frac{\theta}{\theta_{\mathrm{b}}}\right)^2\right], \tag{A.3}$$

where $P(\theta)$ is the normalized power pattern (Wilson et al., 2013), and θ is the distance from the center of the Crab nebula in the sky coordinate. The half power beam width (HPBW) θ_b is given by λ/D, where λ is the observed wavelength and D is the antenna diameter. From Figure 1 of Amato et al. (2000), the spatial intensity distribution of the Crab nebula is approximated by a linear function of θ,

$$B_{\mathrm{CN}}(\theta) = B_0\left(1 - \frac{\theta}{\theta_{\mathrm{CN}}}\right). \tag{A.4}$$

We adopt $\theta_{\mathrm{CN}} = 3$ arcmin in all the frequency bands (e.g. Bietenholz et al., 2015). The coefficient B_0 is determined by

$$2\pi \int_0^{\theta_{\mathrm{CN}}} B_{CN}(\theta)\theta d\theta = S_{\mathrm{CN,tot}}. \tag{A.5}$$

The total flux $S_{\rm CN,tot}$ is calculated from the value in Macías-Perez et al. (2010) as

$$S_{\rm CN,tot} = 973 \pm 19{\rm Jy} \left(\frac{\nu}{1{\rm GHz}}\right)^{-0.296\pm0.006} \exp\left(-\kappa(T_{\rm obs} - 2003)\right), \tag{A.6}$$

where $\kappa = 1.67 \times 10^{-3}$/year, ν is the observed frequency, and $T_{\rm obs}$ is the epoch of observation [year]. We estimate the reception of the Crab nebula R as

$$R \equiv \frac{\int_0^{\theta_{\rm CN}} d\theta\theta B_{\rm CN}(\theta) P(\theta)}{\int_0^{\theta_{\rm CN}} d\theta\theta B_{\rm CN}(\theta)}. \tag{A.7}$$

Then, the received flux density of the Crab nebula S_{CN} is obtained as

$$S_{\rm CN} = R \cdot S_{\rm CN,tot}. \tag{A.8}$$

A standard on-off observation provides SEFD as

$$\begin{aligned} {\rm SEFD} &= \frac{S_{\rm CN}}{y-1}, & \text{(A.9)} \\ y \equiv \frac{P_{\rm on}}{P_{\rm off}} &= \frac{{\rm SEFD} + {\rm S_{CN}}}{\rm SEFD}, & \text{(A.10)} \end{aligned}$$

where $P_{\rm on/off}$ is the received power pointing at the on-source/off-source. The off-source observation was pointed at a direction 1 degree away from the nebula center.

For X band, we observed Jupiter as a calibration source. We estimate SEFD with an on-off observation of Jupiter. When estimating SEFD, we assume that the spatial intensity distribution of Jupiter is uniform within $\theta < 16.15$ [arcsec], and we use the total flux of Jupiter reported by Imke de Pater et al. (2003). Then, using the value of SEFD estimated above, we estimate $S_{\rm CN}$ with an on-off observation of the Crab nebula. For P band, the calibration source was Cyg A. The flux density of Cyg A is given by Baars et al. (1977), and the receptions of Cyg A and the Crab nebula are set to unity, because the sizes of those sources are sufficiently smaller than the beam size.

Taking into account the overlaps of the frequency intervals, the calibrated flux densities for L6–L8 and S1–S5 channels are synthesized into the values for LH and S bands, respectively. The statistical error $\sigma_{\rm sta} = S_1$ is imposed on the flux density in each time bin. The systematic error $\sigma_{\rm sys}$ includes uncertainty of the literature values of flux density used in our analysis, and the time fluctuation of $P_{\rm on/off}$. For each GRP, setting a time interval with a method described in Appendix B, we integrate the flux to obtain the fluence F. The systematic error in F is written as

$$\sigma_{\rm sys} = F \cdot a_{\rm sys}, \tag{A.11}$$

where $a_{\rm sys}$ is defined by using the errors of SEFD (ΔSEFD) and the errors of S_{CN} ($\Delta S_{\rm CN}$), as

$$a_{\rm sys} \equiv \frac{\Delta{\rm SEFD} + \Delta{\rm S_{CN}}}{{\rm SEFD} + {\rm S_{CN}}}. \tag{A.12}$$

Therefore, the total error for the fluence F_i at a given band i is described as

$$\sigma_i = \sqrt{N(\sigma_{\rm sta}\Delta t)^2 + (\sigma_{\rm sys})^2}, \tag{A.13}$$

where N is the number of time bins in the interval to estimate the fluence. When $F_i < 3\sigma_i$, we set an upper-limit on the fluence. Note that we use $F_i + \sigma_i$ as an upper-limit value to estimate $\hat{\chi}^2$.

In order to verify our calibration, we also observed Cas A with Kashima and Iitate telescopes, and Jupiter at S band with Usuda telescope. We estimated the total flux densities of these objects. For the intensity distribution of Cas A, a shell with an outer radius of 130 ± 5 arcsec and a thickness of 32 ± 5 arcsec were assumed, based on the observation of Rosenberg (1970). As shown in Figure A.1, our flux calibration seems to be roughly consistent with previous observations (Imke de Pater et al., 2003; Baars et al., 1977; Vinyaikin, 2014).

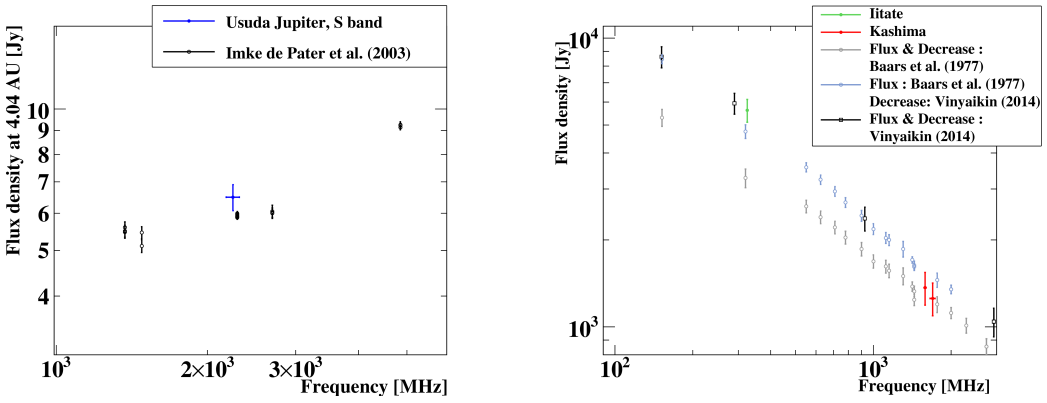

Fig. A.1.— Flux densities of Jupiter (left) and Cas A (right). Our data and previous observations (Imke de Pater et al., 2003; Baars et al., 1977; Vinyaikin, 2014) are plotted. As for Jupiter, our data is normalized to the flux at the distance of 4.04 AU for comparison with the other data. Taking into account that the fluxes of Cas A show secular decrease with a frequency-dependent rate, we plot three cases with different combinations of the literal flux density and decrease rate of Baars et al. (1977) and Vinyaikin (2014).

We also compare the period mean flux density of the Crab pulse $\bar{S}_{\rm CP}$ (e.g. Maron et al., 2000) with previous studies in each frequency band. In Figure A.2, our results

are roughly consistent with previous studies (Sieber, 1973; Lorimer et al., 1995; Moffett & Hankins, 1996). The significant pulse signals were not detected at C and X bands, which may be due to the effects of interstellar scintillation.

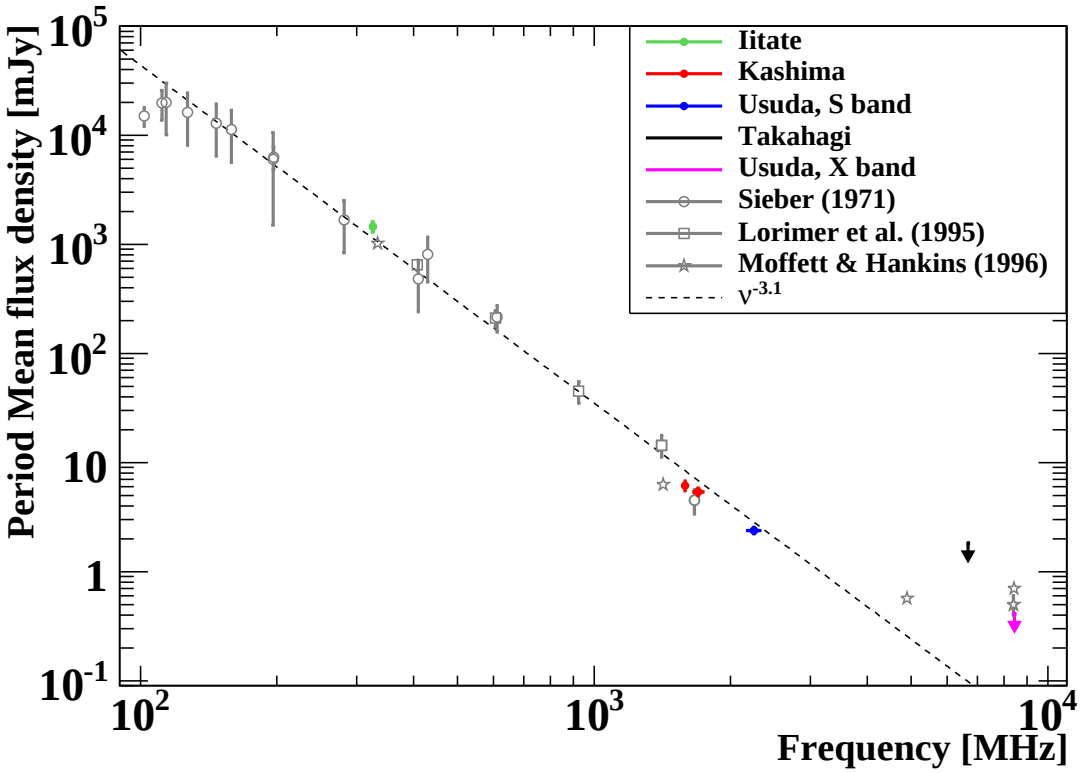

Fig. A.2.— Period mean flux density of the Crab pulse. Our data and previous observations (Sieber, 1973; Lorimer et al., 1995; Moffett & Hankins, 1996) are plotted The dotted line is a reference one showing $\propto \nu^{-3.1}$ (Lorimer et al., 1995). For C and X bands, our observation leads to just upper-limit values.

Appendix B

Time Interval for Fluence Estimate

We need to determine the time interval to estimate the fluence for each GRP. This time interval is different from the selection width defined in Section 4.2.1. According to the phase distributions of the GRP signals detected at both LL and P bands, we empirically established the method to determine the interval as follows. Following the method described in Section 4.2.1, we search for GRPs at P–S bands. To determine the time interval, we divided the GRP samples into two cases: 1) there are signals above the GRP selection thresholds in the LL, LH, and S bands data. 2) there are signals above the GRP selection thresholds only in the P band data.

B.1 GRPs Selected at LL/LH/S Bands

First, for LL, LH, and S bands, in the light curves with 10μs time bin, we search for signals of S/N$\geq$ 4 around the peak time bin, where the signal is above the selection threshold (Section 4.2.1). Next, we set a minimal time interval that includes all the signals of S/N$\geq$ 4, then we estimate the S/N values with 1μs time bin for this interval. We denote the bin numbers of the first and last time bins where the signal exceeds 3 σ as $\tau_{i,1}$ and $\tau_{i,2}$, respectively, for each band i. Finally we determine the interval of the bin numbers from $\min(\tau_{i,1}) - 1$ to $\max(\tau_{i,2}) + 1$ to adopt for LL, LH, and S band commonly, and estimate fluences and their errors or upper-limits.

Since the interstellar scattering largely broadens the pulse profile at P band, another method is required. The bin number $\tau_{\rm P}$ is defined as the 500μs time bin in which the peak time of the highest S/N signal in LL/LH/S bands is included. When there is no time bin of S/N$\geq$ 4 for an interval from $\tau_{\rm P} - 1$ to $\tau_{\rm P} + 1$, this GRP is judged as non-detection at P band. We set an upper-limit based on the fluence for an interval from $\tau_{\rm P} - 1$ to $\tau_{\rm P} + 2$, whose duration 2000 μs corresponds to the interval 95% of the our

GRP samples detected at P band are contained. When we find a time bin of S/N$\geq$ 4 signal(s), a minimal interval that contains all the S/N$\geq$ 4 signal(s) is set. Then, we extend the interval as long as S/N values of the consecutive bins are larger than 2.

B.2 GRPs Selected at only P band

When signals above the selection threshold are found only at P band, we need to determine an interval for L–S bands in spite of the much broader pulse profile in P band. For LL, LH and S bands, in the 10μs-resolution light curve, we tentatively determine an interval first. When multiple and successive time bins with S/N$\geq$ 4 are found between the bin numbers $\tau'_{i,1}$ and $\tau'_{i,2}$, an interval from $\tau'_{i,1} - 1$ to $\tau'_{i,2} + 1$ is defined. Then, from the 1μs-resolution light curve in this interval, we determine a final interval with the same method in the previous subsection, and calculate fluences and their errors or upper-limits. If there is no time bin with S/N$\geq$ 3 in the 1μs light curve for all the bands, we adopt the tentative interval based on the 10μs light curve as the final interval.

When, in the 10μs light curve, multiple and successive time bins with S/N$\geq$ 4 are not found, we set a tentative interval of 30μs (3 bins) centering the time bin with the largest S/N value among LL, LH and S bands. Then, the final interval with 1μs-resolution is determined in the same way described above.

For P band, a minimal interval that contains all the S/N$\geq$ 4 signal(s) is set. Then, we extend the interval as long as S/N values of the consecutive bins are larger than 2.

Appendix C

Error Estimate for LH and S Bands

In our analysis, we synthesized the flux densities for L6–L8 and S1–S5 channels into LH and S bands, respectively. While statistical errors in the synthesized flux are estimated with the standard manner taking into account the overlaps of the frequency intervals, systematic errors $\sigma_{\rm sys,LH}$ and $\sigma_{\rm sys,S}$ are the sums of the systematic errors of the individual channels. The total error is given by $\sigma_{LH/S} = \sqrt{\sigma^2_{\rm sta,LH/S} + \sigma^2_{\rm sys,LH/S}}$. The obtained errors become significantly small owing to the channel synthesis as shown in the central panel of Figure C.1. Hereafter, this method is called "method A", which is the method adopted in the analysis in the main text.

The obtained fluences for the individual channels frequently show significant variations within their narrow frequency range as seen in the left panel of Figure C.1. As Karuppusamy et al. (2010) claimed, the fluence fluctuation in the narrow bands may be intrinsic property in the GRP spectra similarly to the band spectral structure seen in Hankins & Eilek (2007). Although the modulation due to the diffractive interstellar scintillation may be negligible at the channels in L and S bands as discussed in Section 4.3, the fluctuation may be the result of the unknown effects of the interstellar scintillation. In order to take into account this uncertainty, we attempt another method for the error estimate of the synthesized fluences, "method B". In this method, the actual fluence is assumed to be between the highest and the lowest values in the fluences for the channels in each band. For example, at LH band, the upper and lower fluence $F_{\rm max,LH}$ and $F_{\rm min,LH}$ are defined as follows:

$$F_{\rm max,LH} \equiv \max(F_{\rm ch} + \sigma_{\rm ch}), \quad F_{\rm min,LH} \equiv \min(F_{\rm ch} - \sigma_{\rm ch}), \tag{C.1}$$

where $F_{\rm ch}$ and $\sigma_{\rm ch}$ are the fluence and its 1σ error at channel ch $=$ L6, L7 and L8, respectively. In method B, the representative fluence $F_{\rm LH}$ and its 1σ error $\sigma_{\rm LH}$ are

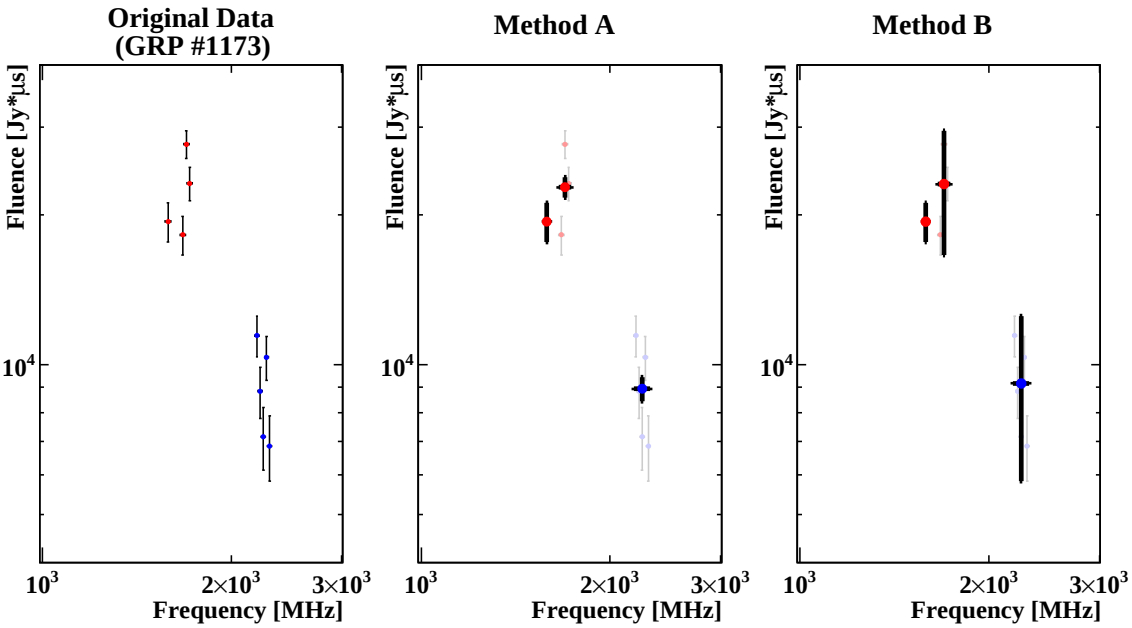

Fig. C.1.— Error estimates for the fluences at LH and S bands. Left: original data points of the four channels in L band (red), and five channels in S band (blue) for GRP #1173. Middle: synthesized data points and errors of LH and S bands with the method A adopted to the analysis in the main text. Right: the same as the middle panel but for the conservative error estimate with method B described in Appendix C.

assumed as

$$F_{\rm LH} \equiv \frac{F_{\rm max,LH} + F_{\rm min,LH}}{2}, \tag{C.2}$$

$$\sigma_{\rm LH} \equiv F_{\rm LH} - F_{\rm min,LH} = F_{\rm max,LH} - F_{\rm LH}. \tag{C.3}$$

As shown in the right panel of Figure C.1, method B leads to larger errors. When there is a channel with a fluence below $3\sigma_{\rm ch}$, we set an upper-limit $F_{\rm max,LH}$ on the fluence at LH band. We also estimate the fluence or its upper-limit at S band in the same way as LH band.

When we use the data generated with method B in the spectral analysis, 95.4% of MPGRPs and 97.0% of IPGRPs are judged to be consistent with SPLs at a significance level of 5% (see Tables C.1 and C.2). In this conservative method, even if a S/N value for a certain channel is above the selection threshold, there are cases that just the upper-limit is set for the synthesized fluence. The numbers of the GRP samples in method B decrease compared to the method A.

Table C.1. The same table as Table 4.4, but with the conservative error estimate, method B.

Detected Band(s)	Group	SPL Assumption Consistent ($\hat{\chi}^2_{\rm min} < 5.99$)	SPL Assumption Inconsistent ($\hat{\chi}^2_{\rm min} > 5.99$)
P & LL & LH & S	I	163	20
P & LL & LH	I	72	3
P & S	I	5	1
P & LL & S	I	9	0
P & LH & S	I	1	0
P & LL	I	88	2
P & LH	I	8	0
LL & LH & S	II	944	59 ($\alpha > 2:1$)
LL & S	II	165	1
LH & S	II	39	2
LL & LH	···	408	25
S	···	146	1 ($\alpha > 2:1$)
LL	···	278	15
LH	···	79	2
P	III	385	3 ($\alpha < -5:3$)
Total		2790	134 ($\alpha > 2:2$, $\alpha < -5:3$)

Table C.2. Same as Table C.1, but for the IPGRPs.

Detected Band(s)	Group	SPL Assumption Consistent ($\hat{\chi}^2_{\rm min} < 5.99$)	SPL Assumption Inconsistent ($\hat{\chi}^2_{\rm min} > 5.99$)
P & LL & LH & S	I	26	2
P & LL & LH	I	14	0
P & S	I	0	0
P & LL & S	I	0	0
P & LH & S	I	0	0
P & LL	I	15	0
P & LH	I	1	0
LL & LH & S	II	60	0
LL & S	II	10	0
LH & S	II	1	0
LL & LH	···	28	2
S	···	4	0
LL	···	23	2
LH	···	2	0
P	III	42	1 ($\alpha < -5:1$)
Total		226	7 ($\alpha > 2:0$, $\alpha < -5:1$)

References

Abdo, A. A., Ackermann, M., Atwood, W. B., et al. 2009, ApJ, 696, 1084

Abdo, A. A., Ackermann, M., Ajello, M., et al. 2010, ApJ, 708, 1254

Aliu, E., Archambault, S., Arlen, T., et al. 2012, ApJ, 760, 136

Amato, E., Salvati, M., Bandiera, R., Pacini, F., & Woltjer, L. 2000, A&A, 359, 1107

Argyle, E., & Gower, J. F. R. 1972, ApJ, 175, L89

Avni, Y., Soltan, A., Tananbaum, H., & Zamorani, G. 1980, ApJ, 238, 800

Baars, J. W. M., Genzel, R., Pauliny-Toth, I. I. K., & Witzel, A. 1977, A&A, 61, 99

Bhat, N. D. R., Tingay, S. J., & Knight, H. S. 2008, ApJ, 676, 1200

Bietenholz, M. F., Yuan, Y., Buehler, R. Lobanov, A. P. & Blandford, R. 2015, MNRAS, 446, 205

Bilous, A. V., Kondratiev, V. I., McLaughlin, M. A. et al. 2011, ApJ, 728, 110

Bilous, A. V., Mclaughlin, M. A., Kondratiev, V. I., & Ransom, S. M. 2012, ApJ, 749, 24

Bilous, A. V., Pennucci, T. T., Demorest, P., & Ransom, S. M. 2015, ApJ, 803, 83

Blackburn, J. K. 1995 in ASP Conf. Ser., 77 "Astronomical Data Analysis Software and Systems IV", ed. R. A. Shaw, H. E. Payne, and J. J. E. Hayes (San Francisco: ASP), 367

Bradt, H. V., Rothschild, R. E., & Swank, J. H. 1993, A&AS, 97, 355

Burke, B. F. & Graham-Smith, F. 2010, An introduction to radio astronomy (Cambridge : Cambridge University Press)

Burke-Spolaor, S., Johnston, S., Bailes, M. et al. 2012, MNRAS, 423, 1351

Campbell, D. B. 2002 in ASP Conf. Ser., 278 "Single-Dish Radio Astronomy: Techniques and Applications", ed. S. Stanimirovic, D. Altschuler, P. Goldsmith, and C. Salter (San Francisco: ASP), 81

Cheng, A. F., & Ruderman, M. A., 1977, ApJ, 212, 800

Cheng, A. F., & Ruderman, M. A., 1980, ApJ, 235, 576

Cheng, K. S., Ho, C., & Ruderman, M. 1986, ApJ, 300, 500

Cheng, K. S., Ho, C., & Ruderman, M. 1986, ApJ, 300, 522

Cognard, I., Shrauner, J. A., Taylor, J. H., & Thorsett, S. E. 1996, ApJ, 457, L81

Collins, S., Shearer, A., Stappers, B., et al. 2012, in IAU Symp. 285, New Horizons in Time-domain Astronomy, ed. E. R. Griffin, R. J. Hanisch, & R. L. Seaman (Cambridge: Cambridge Univ. Press), 296

Cordes, J. M., Bhat, N. D. R., Hankins, T. H., McLaughlin, M. A., & Kern, J. 2004, ApJ, 612, 375

Connor, L., Sievers, J., & Pen, U. 2015, arXiv: 1505.05535

Cordes, J. M., & Wasserman, Ira 2015, arXiv: 1501.00753

Crawford, F., Altemose, D., Li, H., & Lorimer, D. R. 2013, ApJ, 762, 97

Cronyn, W. M., 1970, Science, 168, 1453

Cusumano, G., Hermsen, W., Kramer, M., et al. 2003, A&A, 410, L9

Daugherty, J. K., & Harding, A. K. 1996, ApJ, 458, 278

Eilek, J. A., & Hankins, T. H. 2007, Proceedings of the 363. WE-Heraeus Seminar on Neutron Stars and Pulsars 40 years after the discovery. ed. W. Becker and H. H. Huang. MPE-Report 291. 112

Ellingson, S. W., Clarke, T. E., Craig, J., et al. 2013, ApJ, 768, 136

Ershov, A. A., & Kuzmin, A. D. 2003, Astron. Lett., 29, 91

Ershov, A. A., & Kuzmin, A. D. 2005, A&A, 443, 593

de Pater, I., et al. 2003, Icarus, 163, 434

Dicke, R. H. 1946, RScI, 17, 268

Feroci, M., Stella, L., van den Klis, M., et al. 2012, Exp. Astron., 34, 415

Gajjar, V., Joshi, B. C., & Wright, G. 2014, MNRAS, 439, 221

Gil, J. & Melikidze, G. I. 2005, A&A, 432, L61

Gold, T. 1968, Nature, 218, 731

Goldreich, P. & Julian, W. H. 1969, ApJ, 157, 869

Hankins, T. H., & Rickett, B. J. 1975, in Methods in Computational Physics, Vol. 14: Radio Astronomy (New York: Academic), 55

Hankins, T. H., Kern, J. S., Weatherall, J. C., & Eilek, J. A. 2003, Nature, 422, 141

Hankins, T. H., & Eilek, J. A. 2007, ApJ, 670, 693

Hankins, T. H., Jones, G., & Eilek, J. A. 2015, ApJ, 802, 130

Harrison, F. A., Craig, W. W., Christensen, F. E., et al. 2013, ApJ, 770, 103

Hewish, A., Bell, S. J., Pilkington, J. D. H., Scott, P. F., & Collins, R. A. 1968, Nature, 217, 709

Hobbs, G. B., Edwards, R. T., & Manchester, R. N. 2006, MNRAS, 369, 655

Jessner, A., Popov, M. V., Kondratiev, V. I. et al. 2010, A&A, 524, A60

Johnston, S., van Straten, W., Kramer, M. & Bailes, M. 2001, ApJ, 549, L101

Johnston, S. & Romani, R. W. 2003, ApJ, 590, L95

Karastergiou, A., Chennamangalam, J., Armour, W. et al. 2015, MNRAS, 452, 1254

Kashiyama, K., Ioka, K., & Mészáros, P. 2013, ApJ, 776, L39

Kazantsev, A. N., & Potapov, V. A. 2015, Astronomicheskii Tsirkulyar, 1620, 1

Kazantsev, A. N., & Potapov, V. A. 2015, Astronomicheskii Tsirkulyar, 1628, 1

Karuppusamy, R., Stappers, B. W., & van Straten, W. 2010, A&A, 515, A36

Karuppusamy, R., Stappers, B. W., & Serylak, M. 2011, A&A, 525, A55

Kinkhabwala, A., & Thorsett, S. E. 2000, ApJ, 535, 365

Knight, H. S., Bailes, M., Manchester, R. N., & Ord, S. M. 2005, ApJ, 625, 951

Knight, H. S., Bailes, M., Manchester, R. N., Ord, S. M., & Jacoby, B. A. 2006, ApJ, 640, 941

Knight, H. S., Bailes, M., Manchester, R. N., & Ord, S. M. 2006, ApJ, 653, 580

Knight, H. S. 2006, ChJAA, 6, S2, 41

Knight, H. S. 2007, MNRAS, 378, 723

Kokubun, M., Makishima, K., Takahashi, T. et al. 2007, PASJ, 59, S53

Kondo, T., Koyama, Y., Nakajima, J., Sekido, M., & Osaki, H. 2003, in ASP Conf. Ser., 306 "New Technologies in VLBI", ed. Y. C. Minh (San Francisco: ASP), 205

Kostyuk, S. V., Kondratiev, V. I., Kuzmin, A. D., Popov, M. V., & Soglasnov, V. A. 2003, Astron. Lett., 29, 387

Kramer, M., Karastergiou, A., Gupta, Y., et al. 2003, A&A, 407, 655

Kuiper, L., Hermsen, W., Cusumano, G., et al. 2001, A&A, 378, 918

Kuzmin, A. D., & Losovsky, B. Y. 2002, Astron. Lett., 28, 21

Kuzmin, A. D., & Ershov, A. A. 2004, A&A, 427, 575

Kuzmin, A. D., Ershov, A. A., & Losovsky, B. Y. 2004, Astron. Lett., 30, 247

Kuzmin, A. D., & Ershov, A. A. 2006, Astron. Lett., 32, 583

Lampton, M., Margon, B., & Bowyer, S. 1976, ApJ, 208, 177

Livingstone, M. A., Kaspi, V. M., Gavriil, F. P. et al. 2007, Ap&SS, 308, 317

Lorimer, D. R., & Kramer, M. 2004, Handbook of Pulsar Astronomy (Cambridge: Cambridge Univ. Press)

Lorimer, D. R., Yates, J. A., Lyne, A. G., & Gould, D. M. 1995, MNRAS, 273, 411

Lorimer, D. R., Bailes, M., McLaughlin, M. A., Narkevic, D. J., & Crawford, F. 2007, Science, 318, 777

Lundgren, S. C., Cordes, J. M., Ulmer, M., et al. 1995, ApJ, 453, 433

Luo, Q., & Melrose, D. B. 1992, MNRAS, 258, 616

Lyutikov, M. 2007, MNRAS, 381, 1190

Lyne, A. G., Pritchard, R. S., & Graham-Smith, F. 1993, MNRAS, 265, 1003

Lyne, A., & Graham-Smith, F. 2012, Pulsar Astronomy (Cambridge University Press)

Macquart, J. P., Keane, E., Grainge, K. et al. 2015, in Proc. Advancing Astrophysics with the Square Kilometre Array, PoS(AASKA14)055

Madsen, K. K., Reynolds, S. Harrison, F., et al. 2015, ApJ, 801, 66

Macías-Pérez, J. F., Mayet, F., Aumont, J., & Désert, F.-X. 2010, ApJ, 711, 417

Majid, W. A., Naudet, C. J., Lowe, S. T., & Kuiper, T. B. H. 2011, ApJ, 741, 53

Manchester, R. N., Hobbs, G.B., Teoh, A. & Hobbs, M. 2005, AJ, 129, 1993

Maron, O., Kijak, J., Kramer, M., & Wielebinski, R. 2000, A&A, 147, 195

McLaughlin, M. A., Lyne, A. G., Lorimer, D. R., et al. 2006, Nature, 439, 817

Melrose, D. B. 1995, JApA, 16, 137

Mickaliger, M. B., Mclaughlin, M. A., Lorimer, D. R., et al. 2012, ApJ, 760, 64

Mignani, R. P., Bocchino, F., Bucciantini, N., et al. 2015, arXiv: 1501.02773

Mikami, R., Terasawa, T., Kisaka, S., et al. 2014, JPSCP, 1, 015106

Mikami, R., Terasawa, T., Kisaka, S., et al. 2014, Suzaku-MAXI 2014: Expanding the Frontiers of the X-ray Universe, 180

Misawa, H., Kudo, R., Tsuchiya, F., Morioka, A., and Kondo, T. 2003, Proc. 3rd CRL TDC Symp., 57

Mitsuda, K., Bautz, M., Inoue, H. et al. 2007, PASJ, 59, S1

Moffett, D. A., & Hankins, T. H. 1996, ApJ, 468, 779

Moffett, D. A., & Hankins, T. H. 1999, ApJ, 522, 1046

Mori, H., Kuroda, Y., Miyazawa, T. 2014, Proc. SPIE, 9144, 57

Nyquist, H. 1928, Phys. Rev. Lett., 32, 110

Ohno, M., Kawano, T., Tashiro, M., et al. 2015, arXiv: 1503.01182

Oronsaye, S. I., Ord, S. M., Bhat, N. D. R. et al. 2015, ApJ, 809, 51

Pacini, F. 1968, Nature, 216, 567

Petrova, S. A. 2004, A&AS, 424, 227

Popov, M. V., & Stappers, B. 2003, Astron. Rep., 47, 660

Popov, M. V., Soglasnov, V. I., Kondratiev, A. V., et al. 2008, Astron. Rep., 52, 900

Popov, M., Soglasnov, V., Kondratiev, V., et al. 2009, PASJ, 61, 1197

Press, W. H., Teukolsky, S. A., Vetterling, W. T., & Flannery, B. P. 1992, in Numerical Recipes in C. The Art of Scientific Computing, ed. W. H. Press, S. A. Teukolsky, W. T. Vetterling, & B. P. Flannery (2nd ed.; Cambridge: Cambridge Univ. Press)

Rickett, B. J., & Lyne A. G. 1990, MNRAS, 244, 68

Rosenberg, I. 1970, MNRAS, 147, 215

Ruderman, M. A. & Sutherland, P. G. 1975, ApJ, 196, 51

Sallmen, S., Backer, D. C., Hankins, T. H., et al. 1999, ApJ, 517, 460

Sawicki, M. 2012, PASP, 124, 1208

Shearer, A., Stappers, B., O'connor, P. et al. 2003, Science, 301, 493

Sieber, W. 1973, A&AS, 28, 237

Singal, A. K. & Vats, H. O. 2012, ApJ, 144, 155

Soglasnov, V. A., Popov, M. V., Bartel, N. et al. 2004, ApJ, 616, 439

Stalin, D. H., & Reifenstein, E. C. III 1968, Science, 162, 1481

Strader, M. J., Johnson, M. D., Mazin, B. A. et al. 2013, ApJ, 779, L12

Sturrock, P. A. 1971, ApJ, 164, 529

Takata, J., & Chang, H.-K. 2007, ApJ, 670, 677

Tanaka, S. J., Asano, K., & Terasawa, T. 2015, PTEP, 2015, 073E01

Takahashi, T., Abe, K., Endo, M. et al. 2007, PASJ, 59, S35

Takahashi, T., Mitsuda, K., Kelley, R. et al. 2014, Proc. SPIE, 9144, 25

Taylor, J. H., & Stinebring, D. R. 1986, ARA&A, 24, 285

Terada, Y., Enoto, T., Miyawaki, R. et al. 2008, PASJ, 60, S25

Terasawa, T., & Matsukiyo, S. 2012, Space Sci. Rev., 173, 623

Timokhin, A. N., & Arons, J. 2013, MNRAS, 429, 20

Tingay, S. J., Trott, C. M., Wayth, R. B., et al. 2015, arXiv: 1511.02985

Takefuji, K., Takeuchi, H., Tsutsumi, M., & Koyama, Y. 2010, Sixth International VLBI Service for Geodesy and Astronomy. Proceedings from the 2010 General Meeting, ed. D. Behrend and K.D. Baver. NASA/CP 2010-215864., 378

Thompson, D. J., Bailes, M., Bertsch, D. L. et al., 1999, ApJ, 516, 297

Thornton, D., et al., 2013, Science, 341, 53

Totani, T. 2013, PASJ, 65, L12

Tsai -Wei Jr, Simonetti, J. H., Akukwe, B., et al. 2015, AJ, 149, 65

Tsuchiya, F., Misawa, H., Imai, K., Morioka, A., and Kondo, T. 2010, in 2007, Adv. Geosci., 19, 601

Vinyaikin, E. N., 2014, ARep, 58, 626

Weltevrede, P., Wright, G. A. E., Stappers, B. W., and Rankin, J. M. 2006, A&A, 458, 269

Wilson, T. L., Rohlfs, K., & Hüttmeister, S. 2013, Tools of Radio Astronomy (Berlin: Springer)

Acknowledgement

I would like to extend my gratitude to: Professor Toshio Terasawa for being my supervisor and a great source of inspiration and useful discussions, Assistant Professor Katsuaki Asano, Postdoctral Researcher Shuta Tanaka, Postdoctral Researcher Shota Kisaka, Postdoctral Researcher Yosui Akaike and the active graduate students at the High Energy Astrophysics group in Institute for Cosmic Ray Research, and the University of Tokyo for financial support of my PhD studies, and my family for supporting me throughout my life. This work is also supported by Grants-in-Aid for Scientific Research No.15J09510 from the Ministry of Education, Culture, Sports, Science and Technology (MEXT) of Japan.